The Thesis Committee for Benjamin Joseph Copenhaver
certifies that this is the approved version of the following thesis:

Nonlinear Acoustical Detection of Buried Landmines Using Pulsed Standoff Excitation

APPROVED BY

SUPERVISING COMMITTEE:

Mark F. Hamilton, Supervisor

Thomas G. Muir

Nonlinear Acoustical Detection of Buried Landmines Using Pulsed Standoff Excitation

by

Benjamin Joseph Copenhaver, B.S. Physics

THESIS

Presented to the Faculty of the Graduate School of
The University of Texas at Austin
in Partial Fulfillment
of the Requirements
for the Degree of

MASTER OF SCIENCE IN ENGINEERING

The University of Texas at Austin
May 2014

Dedicated to my parents,
who are even more dedicated to me.

Acknowledgments

The guidance and knowledge of my advisor, Professor Mark Hamilton, were indispensible resources for both the writing of this thesis and my career as an acoustics student at the University of Texas at Austin. His unwavering enthusiasm for the field continues to be a humbling inspiration. It has also been a privilege to work with my other advisor, Dr. Thomas Muir, without whom the work in this thesis could not have been undertaken. His creative, enthusiastic approach to the experimental side of the project was motivating and inspiring, and it was a delight to have had the chance to learn from his vast experience.

Dr. Martin Barlett and Mr. Charlie Slack are due thanks for their technical expertise with the experimental equipment. Special thanks are also due to Justin Gorhum, whose knowledge from previous work on the project and help in the early stages were indispensable. Also, for help with the nuances of LaTeX and MATLAB and many other aspects of life as a graduate student, Dan Tengelsen and Scott Schoen were great office neighbors to have.

This work was supported by the Applied Research Laboratories McKinney Fellowship in Acoustics. Additional support was provided by the Cockrell School of Engineering Thrust 2000 M.E. Class of '66 Endowed Graduate Fellowship in Engineering.

Benjamin Joseph Copenhaver

Nonlinear Acoustical Detection of Buried Landmines Using Pulsed Standoff Excitation

Benjamin Joseph Copenhaver, M.S.E.
The University of Texas at Austin, 2014

Supervisor: Mark F. Hamilton

To help resolve certain practical issues with acoustical methods for landmine detection, experiments were performed using a pulsed, standoff source consisting of sixteen speakers mounted on a circular arc. This source, as well as a pair of 18-inch subwoofers, were used separately for acoustical excitation of the buried mine, and the response of the target site was examined as a function of source frequency, sound pressure level, and excitation signal type, with a particular focus on multitone signals. In addition, modeling was undertaken to investigate the effects of nonlinearity, including bimodular nonlinearity, on frequency generation. A numerical, time-domain solution based on a lumped-element model proposed by Donskoy et al. [J. Acoust. Soc. Am. **117**, 690 (2005)] was developed and used to simulate pulsed excitation and the effects of bimodular nonlinearity, which allowed experimentally observed spectra to be compared with modeled results.

Table of Contents

List of Tables

List of Figures

Chapter 1

Introduction

1.1 Motivation and Background

The ongoing international need for humanitarian de-mining operations is well established, and many remote detection techniques have been proposed and researched.[1,2] One such technique is an acoustical method for landmine detection, which has shown particular promise for a number of reasons. First, these methods do not rely on electromagnetic properties of the buried mine, and thus are not as prone to false positives from buried metallic debris. Additionally, due to the high compliance of the mine, the technique is less affected by solid clutter like rocks and rubble, which pose a problem to imaging techniques such as ground-penetrating radar.

The fundamental principle behind most acoustical techniques for landmine detection is that the high compliance of the mine lid (i.e., the mine arming mechanism in most landmines) makes it unique among the buried objects that are likely to be present in a mined area.[3,4] Resonant behavior of mine lids has been shown to exist in many commonly encountered landmines.[5,6] When the soil around the mine is insonified to induce vibration, the resonance of the mine makes it vibrate differently from the soil around it, as well as differently from buried non-compliant objects such as rocks. This vibrational difference can then be detected through a variety of non-contact means, such as with a Laser Doppler Vibrometer (LDV)[7] or ultrasonic interferometry.[8]

A linear method using the aforementioned approach would involve exciting the soil matrix with continuous tone sweeps over the range of common resonance frequencies for buried mines.[7] The behavior of resonant structures buried in soil has been investigated thoroughly to this end.[9–11] In this application, the optical vibrometer would look for areas of higher amplitude due to the mine's behavior at resonance. These linear methods have some drawbacks, however. For instance, for monofrequency swept insonification, the entire insonified area will be vibrating at the incident frequency, and detecting slight variations in amplitude across the field may prove difficult, especially if the mine is deeply buried.

Nonlinear techniques, on the other hand, offer a convenient way to improve discrimination of buried targets.[9,10,12–14] These methods rely on the detection of frequencies generated due to nonlinear behavior at the interface between the soil and the mine lid, theoretically making target discrimination significantly easier. When a nonlinear system recieves a bifrequency signal as an input, the nonlinearities in that system result in the generation of sum and difference frequencies, as well as other frequencies at different combinations of the original frequencies. One goal of this thesis is to corroborate the work on the nonlinear behavior of buried mines that has been done in the past. The work of Donskoy et al.[9,13] and Korman et al.[10] in particular are considered. Donskoy et al. introduced a lumped-element model of the mine-soil system that includes nonlinearity, and have confirmed its applicability with experimental work. Korman et al. have done extensive experimental work on nonlinear effects in the mine/soil system, including the response of the system to multitone excitation and nonlinear tuning curves of the system resonance.

This thesis introduces three main innovations to the current field of landmine detection. The first is a sixteen-speaker array for standoff insonification of the ground. The aim of the speaker array is to create sound pressure levels on the ground above the mine that are sufficiently high to induce detectable nonlinear behavior without requiring the source to be placed directly above the buried mine. The second is the use of short pulses rather than continuous wave insonification, experimental investigation of which is supplemented by the third innovation, a time-domain adaptation of previous lumped-element models of the mine/soil system. The use of pulses should reduce stress to the speakers and be considerably less obtrusive to operators and bystanders. Additionally, work with large subwoofer speakers located near the buried mine was undertaken in order to further examine the resonance behavior and response to bifrequency excitaiton of the mine/soil system. Portions of the work presented in this thesis have been reported in Refs. 15–17.

1.2 Outline of Thesis

Chapter 2 discusses different models of the mine/soil interaction. Some theoretical background on mechanisms for nonlinearity in the soil and in the interface between the soil and buried mine is introduced, along with a lumped-element model of the mine/soil system, originally introduced and solved in the frequency domain by Donskoy et al.[13] This lumped-element model is adapted for solution by a numerical, time-domain formulation that allows easy investigation of time-domain effects and different types of nonlinearity. Bimodular nonlinearity in particular is explored as a model for the nonlinearity occuring in the soil itself and at the interface between the mine lid and the soil.

Chapter 3 describes the sixteen-speaker array used for standoff insonification. Results from a model of the array as a series of point sources are compared with measurements of the beam pattern of the physical array. In addition, the subwoofers used for higher-amplitude excitation of the target site are described.

Chapter 4 explores a variety of tests and measurements carried out on the lid of a mine simulant. The tests and measurements performed include investigation of the natural frequency of the lid when buried and unburied, as well as the response of the lid to insonification from each source, using different amplitudes, signals, and burial materials. Various signal processing methods for obtaining cleaner frequency spectra are also discussed.

Though the methods of detection and the limitations of practical equipment remain to be considered, these factors are not addressed here. The primary goal of this thesis is to investigate the nonlinear behavior of the insonified mine-soil system, and the capability of our equipment to excite and observe it.

Chapter 2

Models of the Mine/Soil System

Nonlinear behavior in the interaction between the mine and soil is an important factor in improving discrimination between buried mines and other targets in the acoustical method for landmine detection discussed in this thesis. Section 2.1 discusses different mechanisms of nonlinearity in the soil and in the interaction between the soil and the mine lid. Section 2.2 discusses an existing lumped-element model for the mine/soil system, as well as an adaptation of that model to a numerical time-domain solution. The section also discusses applications of nonlinearity to these models, particularly the application of a bimodular stiffness meant to represent the interaction between the soil and the lid of the buried mine.

2.1 Sources of Nonlinearity

The nonlinearity of greatest interest for landmine detection arises at the boundary of the soil and buried mine lid, and occurs because of the lack of bonding at that interface.[13] A specific characteristic of the nonlinearity that arises due to this effect would be extremely beneficial in discriminating between mines and other buried objects. This would most likely take the form of a characteristic harmonic pattern seen in the Fourier transform of the velocity signal of the soil surface in the excited mine/soil system. However, the nonlinearity of the soil itself can be considerable, and must also be taken into account.

2.1.1 Soil Nonlinearity

Extensive information about the nonlinear behavior of soil and other geomaterials can be found in a review paper by Ostrovsky and Johnson.[18] Some relevant highlights from this source follow. Rocks and soil are highly nonlinear media,[†] and their nonlinearity is affected strongly by a number of variables, including water saturation, grain size, and compactness. This nonlinearity is usually quantified by measuring shifts in resonance frequency for a column of the material under investigation. Measurements of harmonic amplitudes via Fourier analysis can also be instructive in investigating the type on nonlinearity found in different geomaterials. For example, partial water saturation of sand columns, especially from dry sand up to 25% saturation, results in a substantial shift in the resonance frequency of the column.[20] In addition, extended high-amplitude excitation of a medium may cause the elastic modulus of the medium to change. It will then take some time (order 10^3 seconds) to return to its original state.[21] This is known as the slow dynamical (relaxation) response. Measurements of harmonic amplitudes via Fourier analysis can also be instructive in investigating the type on nonlinearity found in different geomaterials. For example, the slopes of second and third harmonic strain amplitudes with varying drive strain amplitude in sandstone have been shown to be nearly identical, which indicates nonclassical nonlinearity.[22]

Models of nonlinearity in the soil can take two general forms: classical and phenomenological. The classical form arises from an expansion of the stress-strain relation:

$$\sigma = K\left(\epsilon + \alpha\epsilon^2 + \beta\epsilon^3 + \dots\right), \tag{2.1}$$

where σ and ϵ are stress and strain respectively, K is the elastic modulus, and α and β are nonlinearity coefficients that can, in this case, be expressed as combinations of the elastic moduli.[18] This relation only accounts for some of the nonlinearity

---

[†] Comparative tests between granite and wet sand have shown that unconsolidated materials such as sand and soil have nonlinear behavior very similar to that of rock.[18, 19]

observed in geomaterials, however, so phenomenological models must be applied as well. These might take the form of a function $F[\epsilon, \mathrm{sgn}\,(\dot{\epsilon})]$ added to the stress-strain relation of Eq. (2.1) that describes hysteretic behavior based on the signs of the strain and its first time derivative.[19] Such a function must be adapted to observations of the material in question, as the actual mechanisms of this type of nonlinearity are not yet well understood.[18]

2.1.2 Nonlinearity at the Lid/Soil Interface

The effect of the lack of bonding at the interface between the buried mine lid and the soil above it is thought to be a major contributor to the nonlinearity of the mine/soil system.[9, 10, 12] Because of this lack of bonding, the stress-strain relationship can be very different depending on whether the vibration is in a compressive or tensile phase.[†] During the compressive phase (i.e., negative stress and strain) the soil and lid are always in contact, but during the tensile phase (i.e., positive stress and strain) it may be possible for them to become separated.[13] This can be modeled through a bimodular stiffness, sometimes called a bilinear stiffness or "clapping" nonlinearity. The stress-strain relationship can be viewed as piecewise linear,

$$\sigma(\epsilon) = \begin{cases} \gamma K\epsilon, & \epsilon \geq 0 \\ K\epsilon, & \epsilon < 0, \end{cases} \tag{2.2}$$

where K is an elastic modulus, and γ is the index of bilinearity, a nondimensional parameter between 0 and 1. When $\gamma = 1$ there is no difference between the stiffnesses and the relation $\sigma = K\epsilon$ is recovered (i.e., the relation is fully linear), and when $\gamma = 0$ there is zero stiffness in the modulated part of the curve (i.e., the relation is as nonlinear as possible under this description). The stress-strain diagram for such a relationship is shown in Fig. 2.1. This phenomenon will be present in the soil to some degree due to the granularity of that medium, but the effect should be far more

---

[†] This characteristic is also present to some degree in granular materials such as soil and sand,[23] but the effects of such nonlinearity that arise due to the presence of a buried compliant object such as a mine are thought to overshadow the effects of this type of nonlinearity in the soil itself.[12]

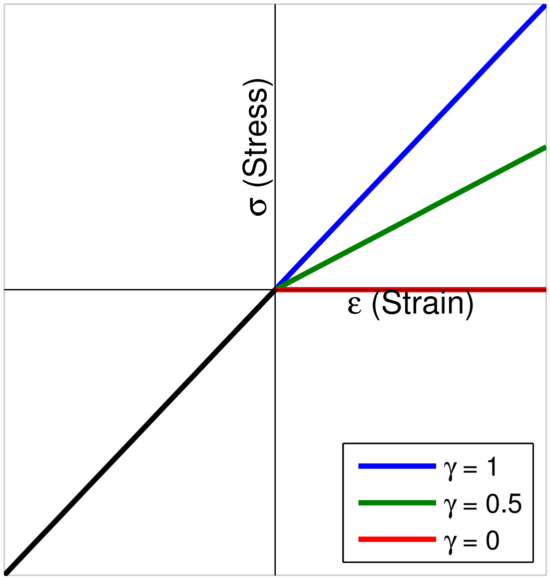

Figure 2.1: Stress-strain diagram for bimodular stiffness with different values of γ.

pronounced in the soil/lid interaction due to the compliance of the lid itself and the possibility for separation across the entire interface.

Note that in the bimodular stiffness model, the amplitude of oscillation has no impact on the effects of nonlinearity. Instead, γ, which corresponds to the "kink angle" between the two stiffnesses in the stress-strain graph, is the sole governor of the nonlinear response.[23] This can be confirmed by examining the Fourier series of the strain response for a sinusoidal stress input. For the input

$$\sigma(t) = \sigma_0 \cos \omega t, \tag{2.3}$$

the strain is[†]

$$\begin{aligned}\epsilon(t) = \frac{\sigma_0}{\pi K}\left(\frac{1}{\gamma} - 1\right) + \frac{\sigma_0}{2K}\left(\frac{1}{\gamma} + 1\right)\cos \omega t \\ + \frac{\sigma_0}{\pi K}\left(\frac{1}{\gamma} - 1\right)\sum_{m=1}^{\infty}(-1)^{m-1}\left(\frac{2}{4m^2-1}\right)\cos 2m\omega t.\end{aligned} \tag{2.4}$$

[†] Appendix A contains the derivation of the Fourier series, as well as a more extended discussion of its characteristics.

The summation contains no powers of the initial amplitude σ_0. Now, consider the ratio between the amplitude of the second harmonic a_2 and the amplitude at the drive frequency a_1:

$$\left|\frac{a_2}{a_1}\right| = \frac{4}{3\pi}\,\frac{1-\gamma}{1+\gamma}, \tag{2.5}$$

which depends only on the ratio $(1-\gamma)/(1+\gamma)$. In contrast, for typical instances of classical nonlinearity [i.e., Eq. (2.1)] the ratio between the amplitudes of the first two harmonics would include some power of the amplitude of the drive signal, indicating higher-order nonlinear effects. The unusual result based on the bimodular stiffness is due to the fact that other than the "kink" at the origin, the system is entirely linear. Another interesting characteristic of the spectrum is that the Fourier series contains only even harmonics after the term for the drive frequency, as well as a DC term because of the increased response whenever the stress is positive.

2.2 Models

A physical model of the system is important for making comparisons with experimental measurements, and to help refine algorithms for detection. Here, we adapt an existing lumped-element model to a numerical, time-domain formulation.

2.2.1 Lumped-element Model

The mine simulant used in this thesis had a diameter of 20 cm with burial depths of up to 15 cm. The frequencies used for excitation did not exceed 500 Hz, which corresponds to a minimum wavelength of 3 m for a typical compressional wave speed in soil of 1500 m/s, or 30 cm for typical shear wave speeds of 150 m/s. In either case, the wavelength is significantly greater than the characteristic geometric size of the system, making a lumped-element approach an appropriate choice.

Donskoy et al.[9,13] have introduced an equivalent lumped-element model for the vibration of a land mine/soil system. Figure 2.2(a) depicts the physical version of this model with its attendant inertial, compliant, and lossy characteristics. Figures 2.2(b)

mine	k_m	2.5×10^7	Pa/m
	r_m	1.7×10^3	kg/(m^{2}s)
	m_m	12	kg/m^2
soil	k_{s1}	2.4×10^7	Pa/m
	r_{s1}	3.9×10^3	kg/(m^{2}s)
	k_{s2}	10^8	Pa/m
	r_{s2}	4×10^3	kg/(m^{2}s)
	m_s	40	kg/m^2
nonlinearity	α	1	μm^{-1}
	β	1	μm^{-1}

Table 2.1: Parameters used for the lumped-element model, after Donskoy et al.[13]

and (c) show adaptations of this model to mechanical and circuit models, respectively. In the mechanical model, inertias, compliances, and losses map respectively to masses, springs and dampers, while the circuit model maps these to inductors, capacitors, and resistors. Mass, stiffness, and internal losses of the mine are given by m_m, k_m, and r_m. The mass of the soil is given by m_s, and the compression and shear components of stiffnesses and losses by k_{s1}, r_{s1}, and k_{s2}, r_{s2}, respectively. The values for these parameters given in Table 2.1 are the values used by Donskoy et al.,[13] which were intended to represent an Italian VS-1.6 antitank mine buried under 1 inch of gravel. The system is excited by an arbitrary force (per unit area, or pressure) $P(t)$. For bifrequency excitation with frequencies f_1 and f_2 where $f_1 < f_2$, we take $P(t)$ to have the form

$$P(t) = P_1 \sin 2\pi f_1 t + P_2 \sin 2\pi f_2 t, \tag{2.6}$$

which can be adapted for single frequency excitation by setting $P_2 = 0$. The amplitude of excitation is typically set at $P_1 = P_2 = 0.3$ Pa, as in Donskoy et al.[13]

Nonlinearity is introduced in these models by way of a classically nonlinear compliance meant to represent the interaction at the mine-soil interface. (Soil nonlinearity

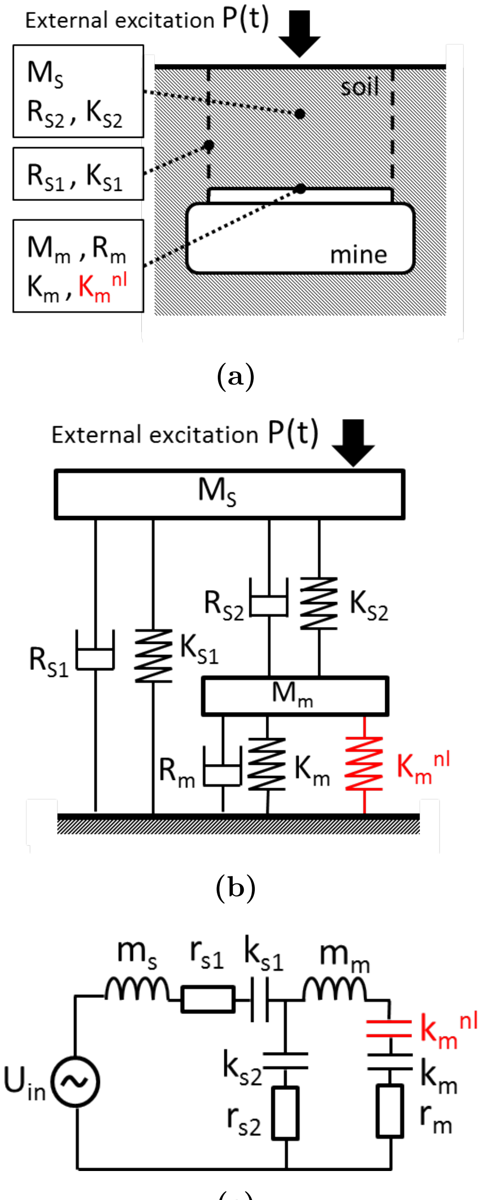

(a)

(b)

(c)

Figure 2.2: Physical, mechanical, and circuit versions of Donskoy et al.'s lumped-element model of the mine-soil system.[13] The nonlinear component is highlighted in red in each case.

is not explicitly considered here.) Quadratic and cubic[†] nonlinearity are both included in the model by way of a nonlinear stiffness given by

$$k_m^{\mathrm{nl}} = k_m \left[\alpha x_m + (\beta x_m)^2\right], \tag{2.7}$$

where k_m is the linear stiffness coefficient, x_m is the displacement of the mine lid, and α and β are the quadratic and cubic parameters of nonlinearity. As indicated in Table 2.1, α and β are both given values of 1 μm^{-1}.[‡]

This model was further adapted by Attenborough et al.[14] to include the presence of a geophone atop the soil column. A fraction of the geophone mass is added as extra loading on the mine/soil system, and a nonlinear stiffness $k_{\mathrm{gp}}^{\mathrm{nl}}$ is added to the nonlinear stiffness of the mine, giving the nonlinear spring a value of $k^{\mathrm{nl}} = k_m^{\mathrm{nl}} + k_{\mathrm{gp}}^{\mathrm{nl}}$. These additions do not significantly alter the structure of the model, so they are not explored further in the present treatment.

In keeping with the chief experimental approach described in Chapter 4, we seek the response of the system to biharmonic excitation. Specifically, we will examine the linear response at the input frequencies f_1 and f_2 and the response at the sum frequency

$$f_\Sigma = f_1 + f_2, \tag{2.8}$$

which is due to quadratic effects. Though a difference frequency is also generated through quadratic effects, in experimental measurements it is typically lost in low-frequency noise, so it will not be considered here. Donskoy et al.[13] also consider the response at the first and second intermodulation frequencies

$$f_{\mathrm{IM1}} = 2f_1 - f_2, \tag{2.9}$$

$$f_{\mathrm{IM2}} = 2f_2 - f_1, \tag{2.10}$$

[†] Though cubic nonlinearity is often negligible in acoustical and vibrational applications, it may result in responses at the intermodulation frequencies that are observable when the system is driven near resonance. Experimental observations of effects of cubic nonlinearity are reported in Chapter 4.

[‡] Note that 1 μm^{-1} is equal to 10^6 m^{-1} rather than 10^{-6} m^{-1}.

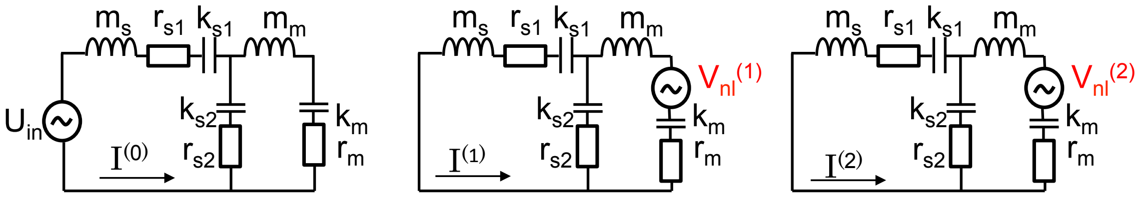

Figure 2.3: Equivalent circuits after Donskoy et al.[13] for (0), (1), and (2) iterations of perturbation method (method of successive approximations) for circuit from Fig. 2.2(c). Total current given by $I^{(0)}(t)+I^{(1)}(t)+I^{(2)}(t)$.

which arise due to a combination of quadratic and cubic effects. Analytical expressions for the response of the system at each of these frequencies[†] may be obtained using a perturbation method, sometimes known as the method of successive approximations, to solve the circuit by iteration. This method is illustrated in Fig. 2.3. In the first iteration the nonlinearity is ignored. Then in subsequent iterations, the nonlinear element is considered to be a voltage source determined by its response to the current determined in its absence in the first iteration, and so on. The total current (which corresponds to the soil surface velocity) is then the sum of the currents in these different iterations.

Results from the perturbation method are shown in Fig. 2.4. Figure 2.4(a) shows the response for single-frequency excitation, while Fig. 2.4(b) shows the response for biharmonic excitation with a difference between primaries given by $\Delta f = f_2 - f_1 = 5$ Hz. In the single-frequency case plotted in Fig. 2.4(a), the response at the primary frequency f_1 and at the second harmonic $2f_1$ are plotted as a function of the primary frequency f_1. As the presence of masses and compliances in the model implies, resonant behavior can be observed in the system. The primary frequency response shows a clear resonance at 150 Hz, and there is also a smaller local maximum beyond the domain of the plot at 580 Hz. However, the presence of a compliant buried object is only part of the reason for this resonant behavior. Though consideration of a fixed object such as a rock or a steel disk would eliminate k_m and m_m from the

---

[†] See Ref. 13 for these expressions and their derivation.

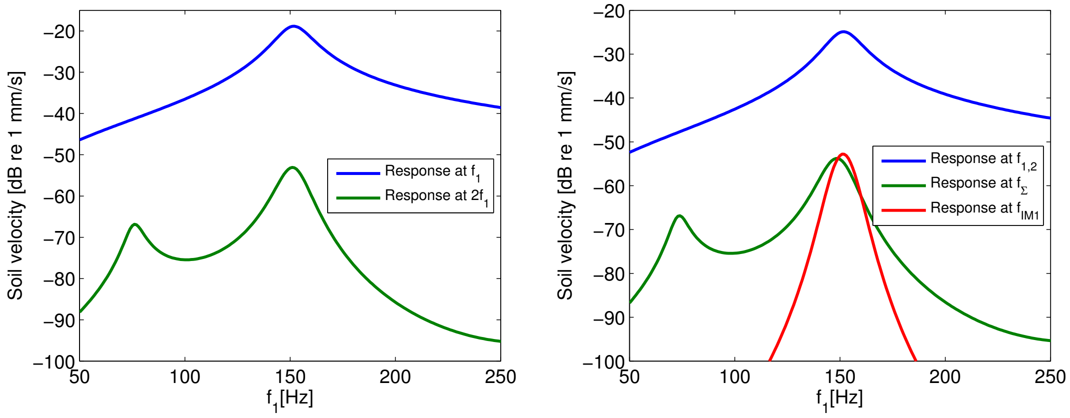

(a) **(b)**

Figure 2.4: Results from perturbation solution of the circuit model of the mine/soil system with resonance frequency of 150 Hz. Responses at different frequencies of interest are shown as a function of the primary frequency f_1. (a) Response at the primary frequency and second harmonic for single-frequency excitation. (b) Response at the primary, sum, and first intermodulation frequencies for bifrequency excitation with primary frequencies f_1 and $f_2 = f_1 + \Delta f$, $\Delta f = 5$ Hz.

model, resonant behavior would still arise due to the mass and compliance of the soil in the column above the buried object.[9] This is one potential drawback of a linear detection scheme.

The quality factor Q can also be determined from the linear response of the system. Equal to the ratio of the natural frequency of the system to the width of the spectral peak at 3 dB down, this parameter describes the amount of damping in a system, with a lower value of Q indicating greater damping. In the system described by the parameters of Table 2.1, the resonance peak is 24 Hz wide, so the quality factor is ~ 9. The smaller peak at 580 Hz has a width of 135 Hz, so its quality factor is ~ 4.

In the frequency response curve for the second harmonic in Fig. 2.4(a), there are two local maxima. The lower occurs when the second harmonic is near the system resonance, i.e., when the primary is at half of the resonance frequency. The higher, larger maximum occurs when the primary frequency is at resonance. Even though the second harmonic is well off resonance, the increased amplitude of the system overall results in a greater response at the second harmonic.

The results for the case of bifrequency excitation are similar to those of the single frequency case. Here, the quadratic response is determined at the sum frequency $f_\Sigma = f_1 + f_2$.[†] Two peaks are again present: the lower occurs when the sum frequency is near the system resonance, i.e., when the primaries are near half the resonance frequency, and the higher, larger maximum occurs when the system is driven by the primaries near resonance, causing the overall response of the system to be greater. Increasing the difference Δf between the primary frequencies causes the higher peak to broaden and eventually resolve into two peaks when Δf is greater than the peak width. These peaks would occur when each primary is at the system resonance. The response at the first intermodulation frequency $f_{\mathrm{IM1}} = 2f_1 - f_2$ is also plotted. Responses at this frequency are often negligible; however, the presence of the resonance in this system causes the response at this frequency to nearly equal the amplitude of the response at the sum frequency when the system is near resonance. According to this simulation, the system must be driven near resonance for this response to be appreciable.

2.2.2 Numerical Time-domain Solution

Whereas Donskoy et al.[13] solved the lumped element model in the frequency domain using a perturbation method as described in the previous section, we aim to find a numerical time-domain solution to the same model. One major advantage of a time-domain treatment of this system is the ability to easily include different types of nonlinearity, including the clapping nonlinearity described previously in this chapter. Furthermore, the nonlinearity need not be a small perturbation in the overall system response. The time-domain model also naturally includes transient behavior at the onset of excitation, and makes it simple to model the response of the system to pulsed

---

[†] Again, though the difference frequency is also due to quadratic effects, it is typically very low in frequency due to the frequency pairs used here, and often lost in low-frequency noise in experimental measurements.

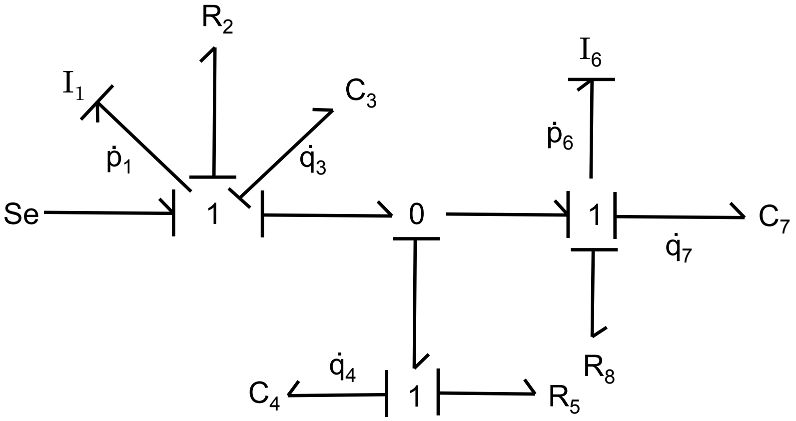

Figure 2.5: Bond graph representation of the lumped-element models in Fig. 2.2.

excitation. Additionally, the complete spectrum of the response at a given frequency or set of frequencies may be obtained by taking a Fourier transform of the time-series solution.

To obtain the differential equations that describe the mine/soil system, a bond graph approach was used.[†] Under this approach, the models in Fig. 2.2 can be represented as shown in Fig. 2.5. The graph has five independent state variables (corresponding to the inertia and compliance elements, I and C, respectively), and thus can be represented by five coupled first-order differential equations.

The state equations corresponding to Donskoy et al.'s model are as follows:

$$\begin{bmatrix} \dot{p}_1 \\ \dot{q}_3 \\ \dot{q}_4 \\ \dot{p}_6 \\ \dot{q}_7 \end{bmatrix} = \begin{bmatrix} -\frac{r_{s1}+r_{s2}}{m_s} & -k_{s1} & -k_{s2} & \frac{r_{s2}}{m_m} & 0 \\ \frac{1}{m_s} & 0 & 0 & 0 & 0 \\ \frac{1}{m_s} & 0 & 0 & -\frac{1}{m_m} & 0 \\ \frac{r_{s2}}{m_s} & 0 & k_{s2} & -\frac{r_{s2}+r_m}{m_m} & -[k_m + k_m^{\text{nl}}(q_7)] \\ 0 & 0 & 0 & \frac{1}{m_m} & 0 \end{bmatrix} \begin{bmatrix} p_1 \\ q_3 \\ q_4 \\ p_6 \\ q_7 \end{bmatrix} + \begin{bmatrix} F(t) \\ 0 \\ 0 \\ 0 \\ 0 \end{bmatrix} \tag{2.11}$$

[†] See Ref. 24 for an in-depth discussion of representing systems with bond graphs.

The parameters in the matrix are the same as those in the lumped element model, and their values may be found in Table 2.1. The remaining parameters in this set of state equations can be transformed to Donskoy et al.'s notation using the following relations:

$$p_1 = m_s v_s, \tag{2.12}$$

$$p_6 = m_m v_m, \tag{2.13}$$

$$k_m^{\mathrm{nl}} = k_m[\alpha q_7 + (\beta q_7)^2], \tag{2.14}$$

where v_m and v_s are the respective velocities of soil and mine, and α and β are again the quadratic and cubic parameters of nonlinearity. The system of equations may now be easily solved in the time domain using the Runge-Kutta method. This method results in time-series waveforms for the velocites of the soil and mine lid. In order to obtain the responses at different frequencies, an FFT (fast Fourier transform) is taken of the soil surface velocity waveform, then the amplitude at the desired frequencies is found from the resulting plot. Care must be taken to window the time series to contain both an integer number of beats and an integer number of cycles of each primary frequency. For comparison with the results from the frequency-domain perturbation solution, the transient response of the system should also be windowed out in order to take the transform of steady-state behavior only.

An example of the time series and corresponding spectra may be found in Fig. 2.6. The time series for the soil surface velocity (v_s) response to bifrequency excitation with $f_1 = 100$ Hz and $f_2 = 105$ Hz is shown in Fig. 2.6(a). Because the excitation is off-resonance and begins at a maximum in the envelope, some irregular effects can be observed at the onset of excitation. If the system were being driven by a single frequency near resonance, the signal would build up to a steady state in a number of cycles roughly equal to the quality factor. However, an irregular response at the onset with energy within the resonance band of the system occurs when the system is driven off resonance. This is visible in Fig. 2.6(b), which is the FFT of the signal in Fig. 2.6(a)—a wide peak centered at the resonance frequency of the system is noticeable despite the primary excitation being well off resonance. However, when these irregularities at the onset are windowed out as in Fig. 2.6(c), only the incident frequencies, sum frequency, and second harmonics are visible as narrow peaks in the spectrum.

As in the perturbation solution, when the system is excited at two primary frequencies f_1 and f_2, the presence of quadratic nonlinearity in the system should lead to increased responses at the sum frequency [Eq. (2.8)], and the presence of cubic nonlinearity should lead to increased response at the first and second intermodulation frequencies [Eqs. (2.9) and (2.10)], among others. The sum frequency response is clearly visible in the spectrum of Fig. 2.6(c), but the intermodulation frequencies cannot be discerned. However, when the system is driven near its resonance frequency as in Fig. 2.6(d), the intermodulation frequencies may be seen as small peaks on the edge of the primary peaks. Additionally, the difference frequency is visible in Fig. 2.6(d), though it is nearly 65 dB down from the amplitude of the primary frequencies. Results at a range of excitation frequencies for single-frequency excitation and bifrequency excitation are shown in Fig. 2.7

The results from the numerical time-domain solution as shown in Fig. 2.7 may now be compared with the results from the perturbation solution as shown in Fig. 2.4. For single-frequency excitation [Figs. 2.4(a) and 2.7(a)], the results agree completely at both the primary frequency and the second harmonic. For the bifrequency case with $\Delta f = 5$ Hz [Figs. 2.4(b) and 2.7(b)], the results are slightly more divergent. The response at the primary frequencies again matches perfectly, but the response at the second harmonic is 6 dB lower in the numerical results than in the perturbation results. The source of this discrepancy is uncertain, though it likely stems from issues with the spectral analysis. Additionally, the result for the response at the intermodulation frequency is very different from that found by the perturbation method. Though significantly lower when the system is being driven near resonance, it does not drop off with increasing frequency as it does in the perturbation solution. The increased amplitude of the intermodulation frequency response seen at higher

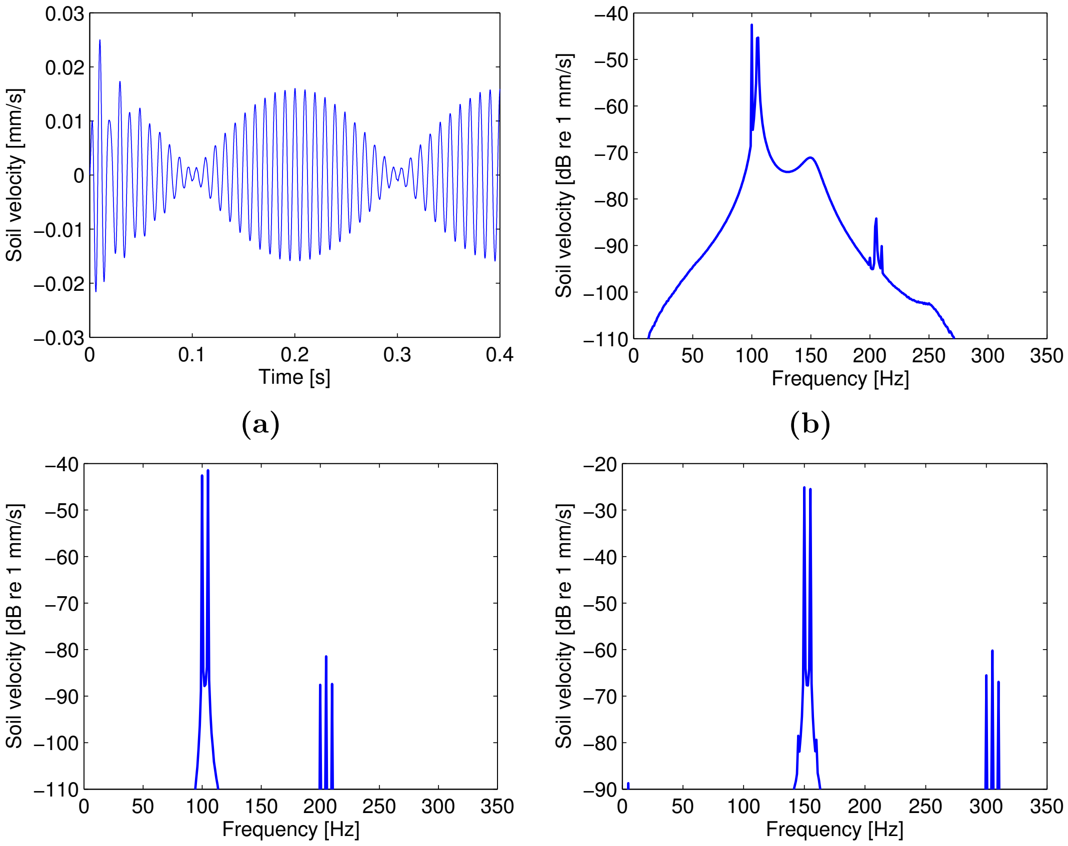

(a) **(b)**

(c) **(d)**

Figure 2.6: Example of results from numerical time-domain solution for bifrequency excitation with $\Delta f = 5$ Hz. (a) Soil surface velocity as a function of time. (b) Spectrum of the signal in (a). (c) Spectrum of the signal in (a) after windowing to exclude the transient at the onset of excitation. (d) Spectrum when the primary frequencies are near the system's natural frequency.

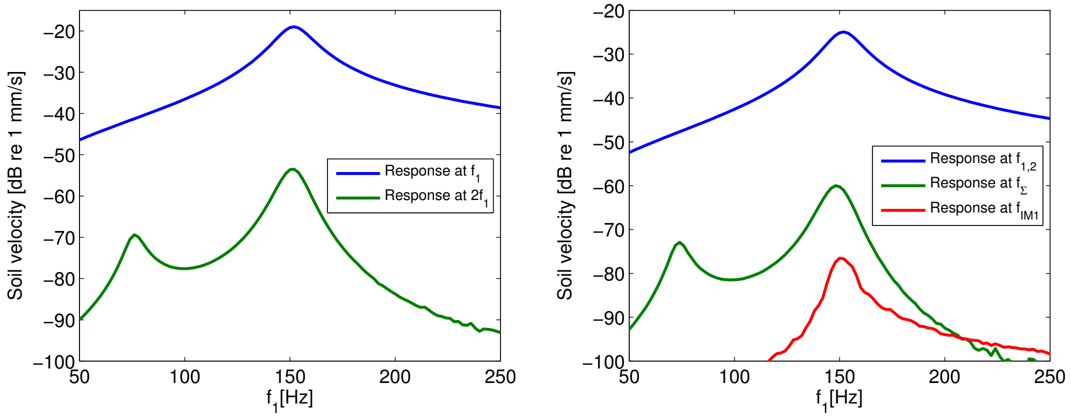

(a) **(b)**

Figure 2.7: Results from the numerical time-domain solution to the lumped element model. Responses at different frequencies are shown as a function of the primary frequency f_1. (a) Response at the primary frequency and at the second harmonic for single-frequency excitation. (b) Response at the primary, sum, and first intermodulation frequencies for bifrequency excitation with primary frequencies f_1 and $f_2 = f_1 + \Delta f$, where $\Delta f = 5$ Hz.

frequencies is probably due to the limitations of the numerical method—accurate results require the Fourier-transformed signal to contain an integer number of cycles of the frequency in question, and it is difficult to achieve this for all frequencies in question.

2.2.3 Application of Bimodular Nonlinearity

As mentioned previously, one major advantage of the numerical time-domain formulation is the ability to easily include other forms of nonlinearity. Here, we consider the bimodular nonlinearity described in Sec. 2.1.2 and apply it to the nonlinear stiffness in the lumped-element model.[†] In terms of the parameters in Eq. (2.11), the

---

[†] For an application of bimodular nonlinearity to wave propagation in a continuous medium, see Ref. 25.

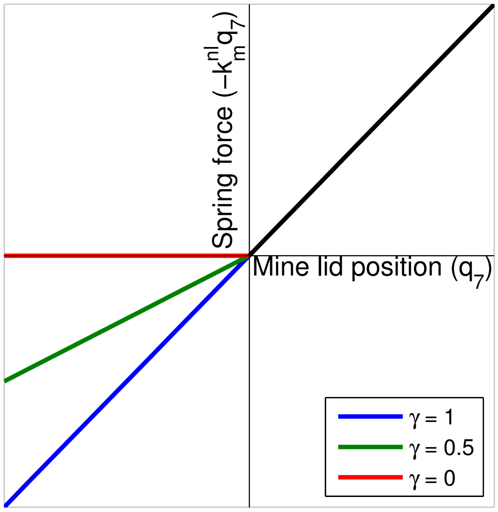

Figure 2.8: Bimodular stiffness as it is applied to our numerical, time-domain model. Softening occurs when the position of the lid is negative.

nonlinear stiffness is given by

$$k_m^{\text{nl}}(q_7) = \begin{cases} \gamma k_m, & q_7 < 0 \\ k_m, & q_7 \geq 0, \end{cases} \tag{2.15}$$

Here, q_7 corresponds to the position of the mine lid. A graphical representation of this type of bimodular nonlinearity as it is applied in the model is shown in Fig. 2.8. It would be trivial to include a stiffness that is dependent on soil velocity or on the difference between motion in the mine and soil, but here we consider only the position (strain) dependent case.

Examples of spectra for a case of bifrequency excitation with $f_1 = 100$ Hz and $f_2 = 105$ Hz and bimodular nonlinearity with different values of γ are shown in Fig. 2.9. Even with the somewhat weak nonlinearity ($\gamma = 0.9$) as shown in Fig. 2.9(a), many more interaction frequencies are visible than in the classically nonlinear case of Fig. 2.6(d). In addition, the sum frequency and second harmonics have greater amplitudes relative to the primaries in the clapping case. When γ is increased to 0.5 in Fig. 2.9(b), the amplitude of the harmonics increases still further, along with

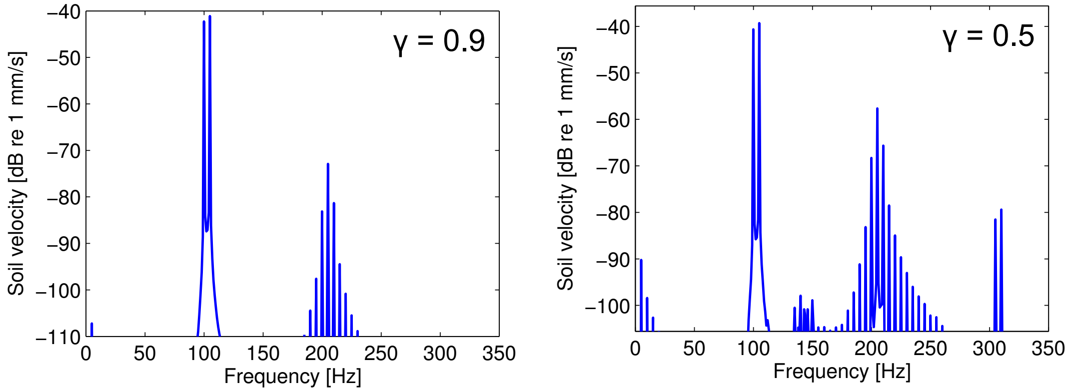

(a) **(b)**

Figure 2.9: Examples of soil surface velocity spectra under bimodular nonlinearity condition, with $f_1 = 100$ Hz and $f_2 = 105$ Hz. (a) $\gamma = 0.9$. (b) $\gamma = 0.5$. As γ decreases, interaction frequencies increase in number and in amplitude.

even more interaction frequencies becoming visible. The difference frequency is also visible, though in each case it is far lower in amplitude than the sum frequency.

Changes in γ affect more than just the spectrum. As illustrated in Fig. 2.10, decreasing γ causes the natural frequency of the entire system to decrease due to the overall decreasing stiffness of the system. Though the resonance frequency when $\gamma = 0.9$ is nearly the same as in the linear case, when $\gamma = 0$ the resonance shifts from 150 Hz to 126 Hz. In addition, very low values of γ can allow the amplitude of second-order effects like the second harmonic in the single-frequency case or the sum frequency in the bifrequency case to overtake the amplitude of the primary frequency. This occurs when the system is driven at about half the natural frequency, which places these frequencies near the overall system resonance. It is interesting to note that even though the resonance of the system changes with γ, the width of the resonance peak remains constant at $\sim$17 Hz. This results in a slight shift downward in the quality factor as γ decreases, from $\sim$8.4 when $\gamma = 1$ to $\sim$7.9 when $\gamma = 0$.

As discussed in Sec. 2.1.2 and Appendix A, the spectrum of the response of a bimodular stiffness subjected to a sinusoidal input has some unique characteristics. These include the presence of only even harmonics beyond the fundamental, and the

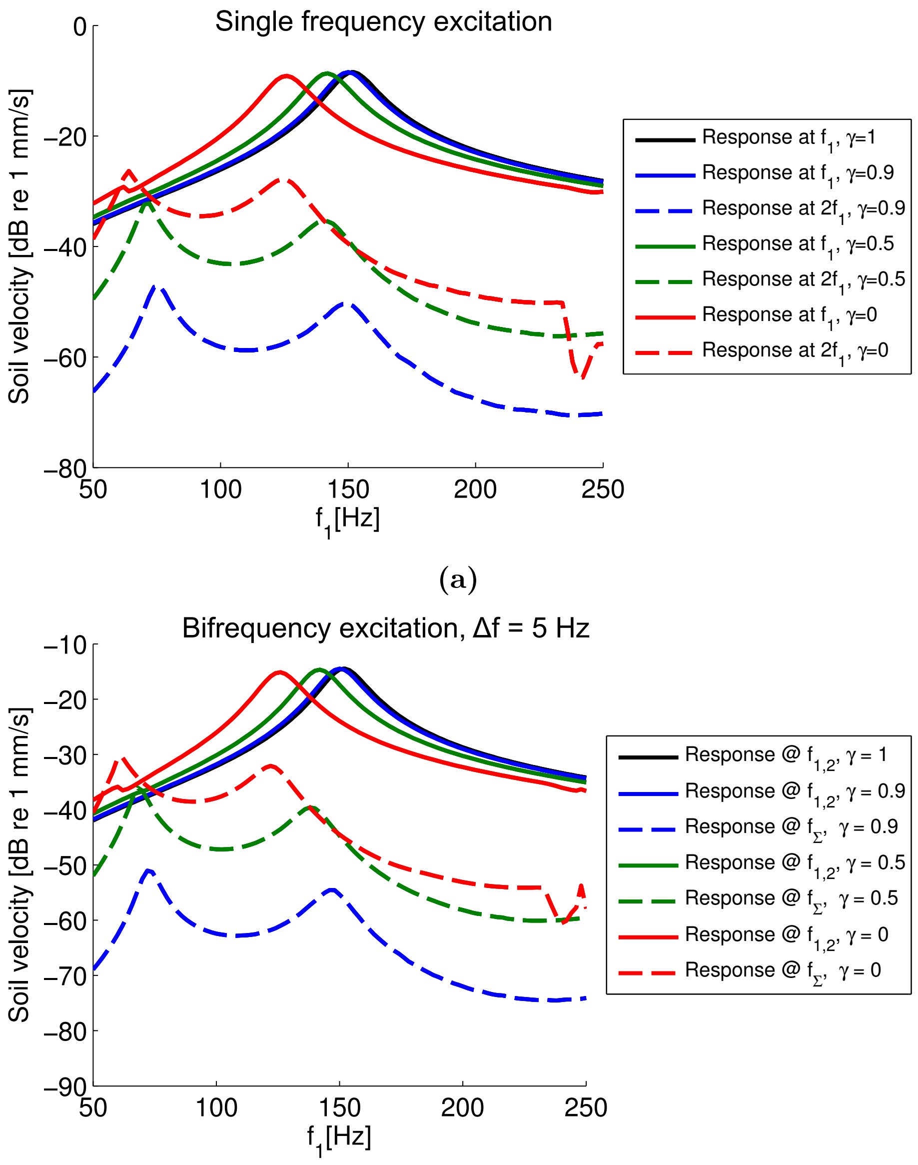

(a)

(b)

Figure 2.10: Results from the numerical time-domain solution for the mine/soil model with bimodular nonlinearity included. Responses at different frequencies are shown as a function of the primary frequency f_1, and with different values of γ. (a) Linear response at the primary frequncy and quadratic response at the second harmonic for single-frequency excitation. (b) Response at the primary and sum frequencies for bifrequency excitation with $\Delta f = 5$ Hz. Note the shifting of the primary resonance downward in frequency with decreasing γ.

linear relationship of the higher harmonics to the amplitude of the fundamental. Using the numerical time-domain simulation, we can examine the behavior of such a stiffness when included in the model with masses and other stiffnesses. Under single-frequency excitation at 150 Hz and $\gamma = 0.5$, the amplitude of the second harmonic is 26 dB lower than the primary no matter the overall amplitude of excitation. However, in the case of classical nonlinearity, the second harmonic is 34 dB down from the primary under the usual excitation amplitude of 0.3 Pa, whereas the difference decreases to 22 dB lower than the primary when the excitation amplitude is doubled. This phenomenon is illustrated in Fig. 2.11, which shows different amplitudes of single-frequency excitation of the mine/soil system with both a classically nonlinear stiffness and the bimodular stiffness.

Despite the indication of Eq. (2.4) that only even harmonics are present when a bimodular stiffness is excited by a sinusoid, odd harmonics can be clearly seen in Fig. 2.11(b) and (d), albeit at a reduced amplitude from the even harmonics. This can be explained by viewing the even harmonics as secondary sources. For example, when the system is excited by multiple frequencies, interaction frequencies such as the sum frequency will arise. If the system is excited by a primary frequency f_1 and another frequency $f_2 = 2f_1$ (simulating the effect of the second harmonic), then the sum frequency $f_\Sigma = f_1 + 2f_1 = 3f_1$ will be at the frequency of the third harmonic.

2.2.4 Combining Nonlinear Effects

Of course, the nonlinearity present in the physical mine/soil system will likely be neither exclusively classical nor entirely bimodular. These effects could be combined to more closely approximate observed mine/soil system behavior. This combination could take the form of a stress-strain relationship that is both nonlinear and has a "kink" at the origin, combining the relations of Eq. (2.1) and Eq. (2.2):

$$\sigma(\epsilon) = \begin{cases} \gamma K_0 \left(\epsilon + \alpha\epsilon^2 + \beta\epsilon^3 + \ldots\right), & \epsilon \geq 0 \\ K_0 \left(\epsilon + \alpha\epsilon^2 + \beta\epsilon^3 + \ldots\right), & \epsilon < 0, \end{cases} \tag{2.16}$$

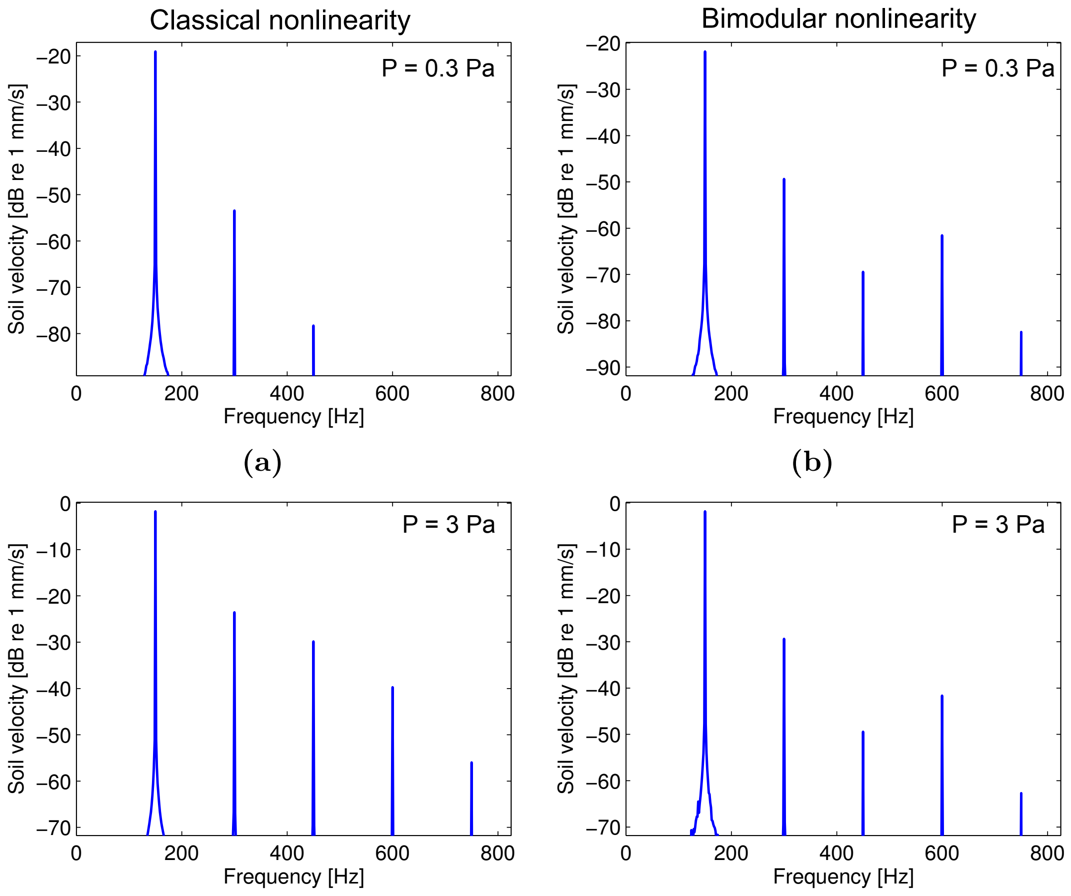

(a) (b) (c) (d)

Figure 2.11: Comparison of soil/mine system response to single-frequency excitation ($f_1 = f_0 = 150$ Hz) with different amplitudes. Both classical nonlinearity and bimodular nonlinearity ($\gamma = 0.5$) are considered. (a) Classical nonlinearity, amplitude 0.3 Pa. (b) Bimodular nonlinearity, amplitude 0.3 Pa. (c) Classical nonlinearity, amplitude 3 Pa. (d) Bimodular nonlinearity, amplitude 3 Pa. With classical nonlinearity, when the amplitude of excitation increases from 0.3 Pa (a) to 3 Pa (c), the relative amplitude of the harmonics increases dramatically. Under bimodular nonlinearity however, when the amplitude of excitation increases from 0.3 Pa (b) to 3 Pa (d), the relative amplitude of the harmonics remains the same.

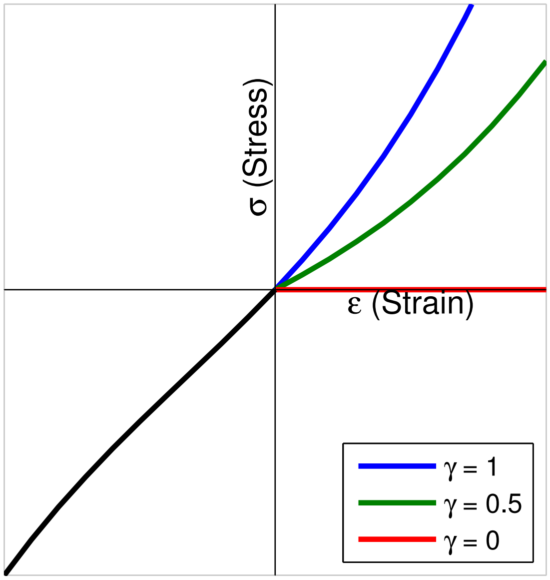

Figure 2.12: Stress-strain diagram for stiffness that combines bimodular stiffness with classical nonlinearity, as given in Eq. (2.16).

Stress-strain curves for this relationship are shown in Fig. 2.12. A complete exploration of the effects of different ways of combining nonlinearity is left for future investigations.

2.3 Conclusion

The models described in this chapter by no means claims to comprehensively describe the complicated system under examination. However, they do help in obtaining a qualitative evaluation of the dynamic behavior of the system, especially with the results obtained using the numerical solution. In addition to allowing examination of the motion of the system in the time domain and the associated spectra, it has opened up many types of nonlinearity to easy application to the model. Experimental results will inform future iterations of this model, especially as to the type(s) of nonlinearity that should be included. The application of bimodular nonlinearity to the model of the mine/soil system has many interesting effects, but experimental work will be needed to determine the degree to which this type of nonlinearity applies to the problem. If its effect is significant, as the limited effect of overall amplitude on the harmonics generated due to the presence of a buried compliant object could be useful a defining characteristic of the nonlinear response, though again, significant expermental investigation is necessary to confirm its applicability.

Chapter 3

Standoff Array Characterization

The sixteen-speaker array used for standoff insonification of the ground is described in this chapter. This array was conceived, designed, and developed by T.G. Muir while at the National Center for Physical Acoustics (NCPA) at the University of Mississippi, assisted by Dr. Wayne Plager on the element design. The array was made available to the Applied Research Laboratories at the University of Texas at Austin (ARL:UT) for testing and experimentation. The present effort is a continuation of work originally carried out and reported by Barlett et al.[26] at ARL:UT, though it has been deconstructed and reassembled with minor modifications since that work was presented. Section 3.1 describes the physical components and construction of the array. Models and measurements of the sound field from the array are described in Sec. 3.2. A pair of subwoofers was also used for investigation of increased excitation levels at the target site, and is described in Sec. 3.3.

3.1 Array Construction

The standoff array, pictured in Fig. 3.1, consists of sixteen speakers arranged on a circular arc of radius 6 feet (1.83 m), with the speakers placed every 8 inches (20.3 cm) horizontally. The array is thus more densely packed at the top of the arc than on the sides in terms of angular spacing, as Fig. 3.1 shows. This provides for some "amplitude shading" of the array, reducing minor lobes with some minor broadening of the beam. In this circular arc configuration the speakers are in phase along the center axis of the circle at any distance from the array, due to the equal distance of any on-axis point to all speakers. The speakers are 6 inch bass midrange

Figure 3.1: Sixteen-speaker array used for ground insonification. The radius of the array is 6 feet, and each speaker is separated horizontally from its neighbors by 8 inches.

speakers from Renaissance Audio® (model MSW-1166).[†] Each speaker is mounted in a cylindrical PVC enclosure with a volume of 1.25 cubic feet (35,400 cc), which is packed with wool to increase internal absorption and reduce reverberation in the back volume. The array framework was constructed from 80/20 brand aluminum components, and it is mounted on an aluminum cart with pneumatic tires for easy maneuverability.

As shown in Fig. 3.2, the speakers are wired as two interwoven "modules" of eight speakers each, with pairs connected in series. The nominal impedance of each speaker is 8 ohms, so this reduces the input impedance of each module to 4 ohms, as well as allowing the odd and even speakers to be driven independently — when two frequencies are being used, sending each frequency through a different amplifier and module reduces the possibility of nonlinear interactions occuring in the speakers and amplifiers. Crown® CE4000 audio amplifiers are used to drive the array. For

---

[†] See Appendix B for the manufaturer's specifications for the speakers and other equipment.

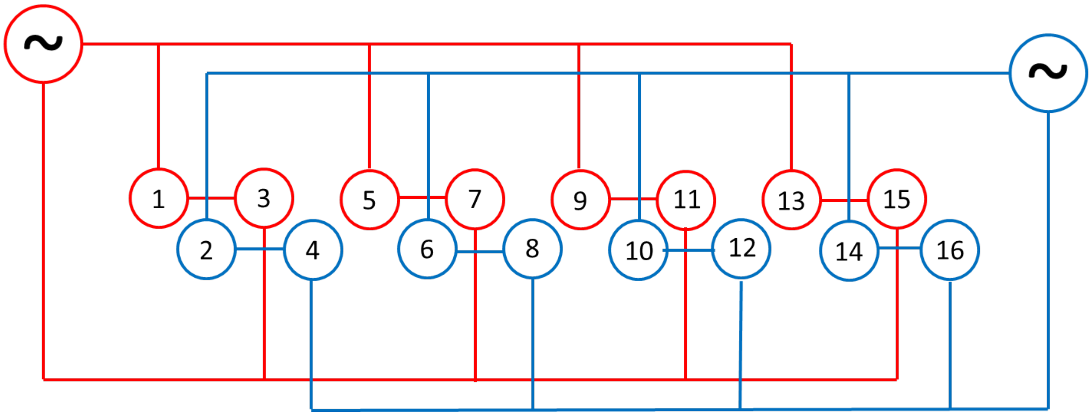

Figure 3.2: Circuit diagram of interwoven speaker "modules" for standoff array. Even and odd speakers are driven independently by amplifiers operating in bridge mode.

bifrequency insonification, the amplifiers are operated in bridge mode,[†] for which each amplifier has a nominal maximum output of 2800 W into the 4 ohm impedance of a single module. For single-frequency measurements, a single amplifier operating in stereo mode drives both modules for a maximum output of 1200 W per module. Input signals are generated by one or two Wavetek model 278 digital function generators. For pulsed, bifrequency signals, these can be triggered simultaneously by a pulse from a third function generator. The maximum amplitude that can be generated by the function generators without causing clipping in the amplifiers is 1.4 V.

3.2 Field Characterization

3.2.1 Models

The array was modeled in MATLAB by treating each speaker as a point source radiating a sinusoidal signal. The pressure at a point $\mathbf{r}$ can be found by summing the spherical pressure waves radiated in phase from each source:

$$p(\mathbf{r}) = \sum_{n=1}^{16} \frac{1}{R_n} e^{-jkR_n} \tag{3.1}$$

[†] See Appendix B for details of amplifier operation.

Here, k is the wavenumber ω/c [where $\omega = 2\pi f$ and c is the sound velocity in air (343 m/s)], and R_n is the distance from speaker n to the point $\mathbf{r}$. The frequencies under investigation range from 125–500 Hz, which corresponds to wavelengths in air of 0.7–2.7 m. The speakers are 0.15 m in diameter (roughly five times smaller than the shortest possible wavelength), so the point source model is reasonable for these frequencies. The field on the ground in front of the array as predicted by this model is shown at two different frequencies in Fig. 3.3. Black dotted lines indicate the width of a typical roadway, showing sufficiently wide coverage at lower frequencies. Additionally, the on-axis amplitude as far as 20 m away from the array is only 20 dB down from the maximum amplitude in the plane of the array.

Our array was practical to build, and its characteristics may be better understood by comparing with theoretical models. The present array's characteristic of every point on axis being equidistant from the radiating surface(s) is shared with the ring piston as described in Ref. 27[†]. Recall that sources mounted in the array lie along the perimeter of a circular arc in the vertical plane with the center in the plane of the ground. If the ground is modeled as a nominally hard (rigid) surface, then the sources combined with their images used to satisfy the rigid ground condition lie along the perimeter of a complete circle. To this extent our array resembles a ring source, because in the limit of a continuous distribution of point sources along the semi-circle above the ground, one may expect to recover the directivity function of a ring source in free space. The directivity for such a ring source is given by

$$D(\theta) = J_0(ka \sin\theta), \tag{3.2}$$

where a is the radius of the ring and θ is the angle off axis. A comparison between Eq. (3.2) and the directivity of the array modeled as point sources is presented in Fig. 3.4. The directivity of the ring source is narrower because sound is radiated from every point on the source, whereas the loudspeaker array radiates at sixteen points on the arc. As noted in Sec. 3.1, the constant horizontal spacing of the speakers

---

[†] Pages 442–445.

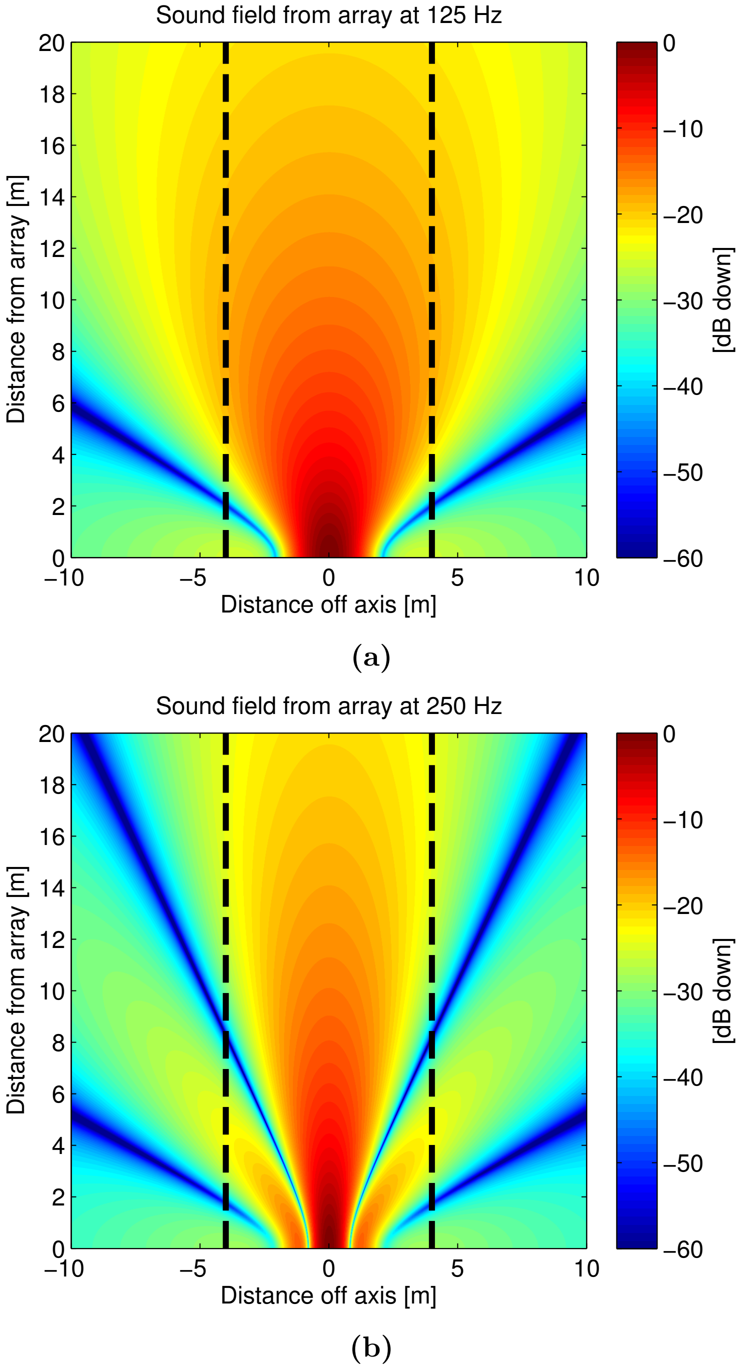

Figure 3.3: Sound field in front of array, modeled in MATLAB as an array of point sources radiating at (a) 125 Hz and (b) 250 Hz. The width of a typical roadway is indicated by the black dotted lines.

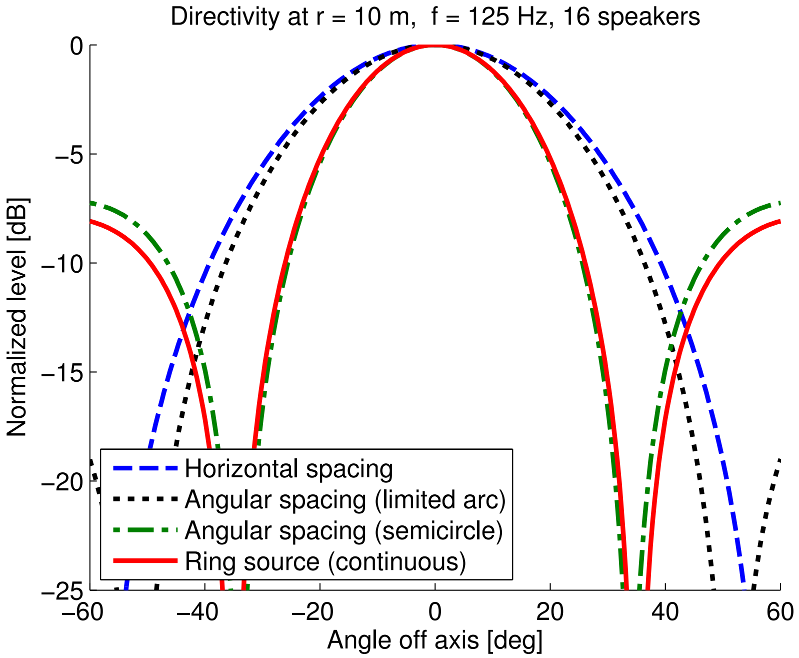

Figure 3.4: Comparison of the directivity pattern at 125 Hz for the array modeled as sixteen point sources in three different configurations and as a ring piston. The directivity patterns shown are for constant horizontal spacing of elements, constant angular spacing of elements over the arc occupied by the horizontally spaced speakers, constant angular spacing of elements over a full semicircle, and the continuous ring source.

in the array causes a slight decrease in the angular spacing between speakers at the top of the array. When the speakers are evenly spaced in arc angle instead of in the horizontal coordinate, the directivity approaches that of the ring source. A near-exact directivity to that of the ring source is obtained when the sources are evenly angularly spaced across the entire semicircle. When the sources are close together and evenly spaced in angle within the arc occupied by the horizontally-spaced speakers (i.e., from $-56°$ to $+56°$ from vertical), the directivity resembles that of the horizontally spaced speakers, but is slightly narrower, as it is a closer approximation to the ring source. The horizontal spacing of the present array results in a slightly wider directivity, though this may come at some cost to the absolute amplitude.

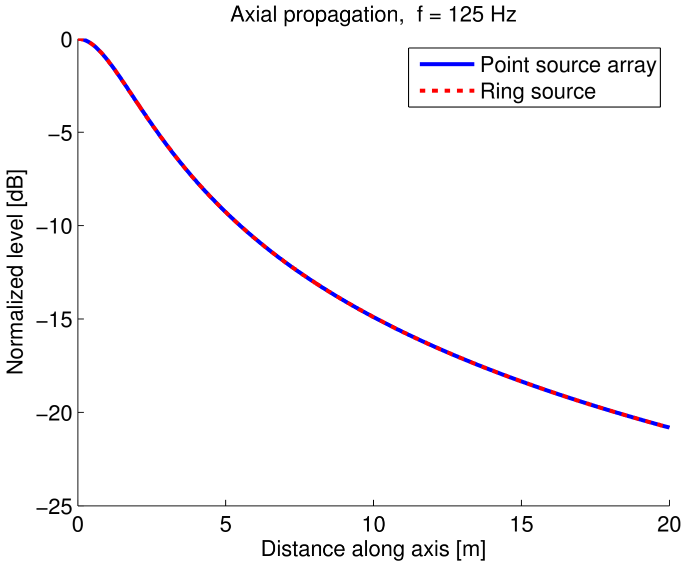

Figure 3.5: Comparison of the axial propagation at 125 Hz for the array modeled as point sources and as a ring piston.

Though the ring source model and the point source model for the present array differ somewhat in terms of directivity patterns, the models compare much more favorably when the on-axis amplitude is examined. The on-axis decay factor for the ring piston source is simply

$$\frac{1}{\sqrt{1+r^2/a^2}}, \tag{3.3}$$

where r is the distance along the axis. This decay is unique in that it is frequency-independent, which is due to the radiation from every point along the source arriving in phase at any given point along the axis. The loss of amplitude with distance is therefore due only to spherical spreading from the elements in the array as projected along the array axis, rather than the much stronger effect of phase incoherence associated with signals from different elements of the array arriving on axis at different times (e.g., as occurs for a linear array or a circular piston source). Figure 3.5 shows a comparison of this model for on-axis amplitude with the point source model, and shows the two models to agree exactly on this point.

3.2.2 Measurements

3.2.2.1 Instrumentation

To measure the sound output of the array, a G.R.A.S. type 40BF 1/4-inch free-field microphone was used together with a G.R.A.S. type 26AC preamplifier.[†] The microphone was mounted on a stand such that its height above the ground for each measurement was approximately 3 inches. For these measurements, data was collected using a Tektronix TPS2024 digital storage oscilloscope. See Appendix B for manufacturer's specifications.

To investigate the beam pattern of the speaker array, measurements of the sound pressure level (SPL) were made as a function of angle and separately as a function of on-axis distance in front of the array. These field characterization measurements were made with only one frequency at a time, so both array modules were driven by a single two-channel amplifier operating in stereo mode. Tone bursts of four cycles were used as the signal to be measured. Despite the short duration of these signals, the amplitude was constant throughout the length of the signal, allowing a reasonable measurement of SPL to be made. To reduce human error, the built-in oscilloscope math functions were used to read the peak-to-peak amplitude of the voltage signal from the microphone. From this value, the RMS pressure and thus the SPL can be calculated. For a sinusoidal signal, the RMS amplitude is given by the amplitude (which is half of the peak-to-peak amplitude) divided by $\sqrt{2}$, so

$$V_{\mathrm{rms}} = \frac{V_{\mathrm{PP}}}{2\sqrt{2}}. \tag{3.4}$$

To convert from voltage to pressure, we use the sensitivity S in V/Pa of the microphone along with the gain G in dB of the microphone preamplifier[‡], giving

$$p_{\mathrm{rms}} = \frac{V_{\mathrm{rms}}}{SG}. \tag{3.5}$$

[†] Manufacturer's specifications for these can be found in Appendix B.

[‡] The microphone we used has a sensitivity of 3.49 mV/Pa, and the gain was typically set to 20 dB.

When substituted into the equation for SPL with reference pressure $p_{\text{ref}} = 20\,\mu\text{Pa}$,

$$\text{SPL} = 20\log_{10}\left(\frac{p_{\text{rms}}}{p_{\text{ref}}}\right), \tag{3.6}$$

we obtain a relation for SPL in terms of the peak-to-peak voltage output of the microphone:

$$\text{SPL} = 20\log_{10}\left(\frac{V_{\text{PP}}}{2\sqrt{2}\,p_{\text{ref}}S10^{G/20}}\right). \tag{3.7}$$

3.2.2.2 Directivity Measurements

To investigate the directivity of the standoff array, measurements were made at a distance of 10 m from the center of the array, at angles from 60° left to 50° right of the center axis. The sound field measurements were made at 125 Hz, 250 Hz, and 500 Hz. The results are shown in Fig. 3.6 along with the predicted directivity at the corresponding distance and frequencies. This predicted curve is based on the point-source model of Sec. 3.2.1. Each red circle indicates the average of three measurements made at a given position. To compare off-axis falloff, both measured values and predicted values were normalized such that the on-axis level was 0 dB.[†] Good agreement can be seen between the predicted and measured values.

3.2.2.3 Propagation Measurements

Additional measurements were made to verify the on-axis levels at increasing distance from the array. These measurements were undertaken only at 250 Hz. For reference, the maximum level observed on-axis at a distance of 2 m was approximately 123 dB (re 20 μPa). The results in Fig. 3.7 show good agreement close to the array, but the measured results are lower in amplitude than predicted as distance from the array increases. This discrepancy cannot be accounted for by attenuation—the attenuation in air at these frequencies would be less than 1 dB at 20 meters. One

---

[†] Here, the on-axis SPL values (re 20 μPa) were 106 dB, 106 dB, and 103 dB for the 125 Hz, 250 Hz, and 500 Hz trials, respectively.

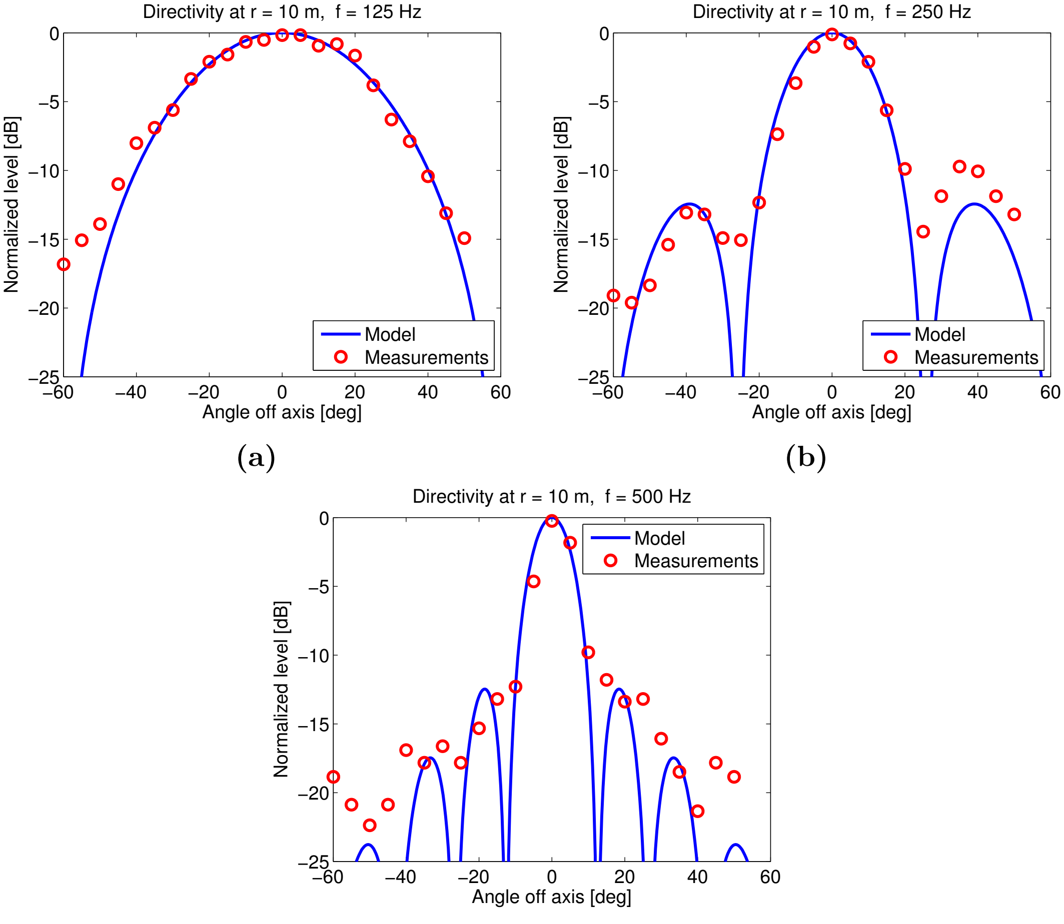

(a) **(b)**

(c)

Figure 3.6: Comparison of measured and predicted standoff array directivity at a 10 m radius measured from the center of the array, made at (a) 125 Hz, (b) 250 Hz, and (c) 500 Hz.

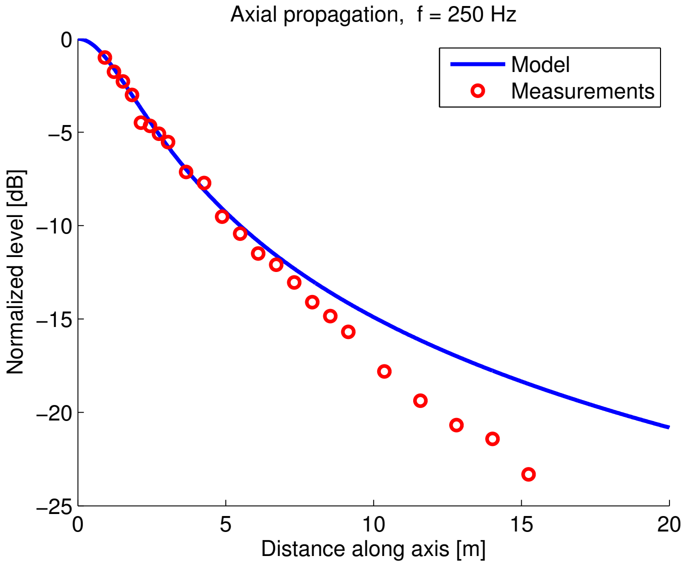

Figure 3.7: Comparison of measured and predicted axial propagation at 250 Hz. Predicted curve comes from the point source model of the array.

possibility is that reflections from the grass-covered ground surface could be phase shifted due to the finite impedance of the ground, resulting in destructive interference. This is especially likely as the angle of incidence approaches grazing,and indeed the attenuation appears to increase as distance from the array increases. At 7 m, where the measured amplitude begins to diverge from the predicted values, the angle from vertical is 75.3° for the ray from the highest speakers on the array, and 81.6° for the lowest speakers—both approaching grazing (90°). Additional measurements to further examine this unusual outcome would be an interesting point of investigation in a future study.

3.3 Subwoofers

In order to investigate the effects of higher amplitudes of excitation, we employed a pair of Peavey® Lo Max® 18-inch subwoofers. These were mounted in subwoofer cabinets that put the speakers at a 45-degree angle to vertical, and were positioned directly above the buried mine as pictured in Fig. 3.8. Each subwoofer was driven by

Figure 3.8: Photograph of subwoofers used for high-intensity insonification. Unburied mine is shown for reference.

a single function generator and Crown amplifier, similarly to the way the two modules of the standoff array were separated. Each speaker has an impedance of 8 ohms, so the maximum output of each amplifier is 2400 W for a maximum SPL above the mine of 145 dB, roughly 20 dB greater than that produced by the sixteen-speaker array at 2 m. These are not intended for any sort of standoff excitation, rather being useful primarily for in-depth experimental investigation of nonlinear effects arising in the mine/soil system when high excitation amplitudes are employed.

3.4 Conclusion

The sixteen-speaker standoff array was shown to have a beam pattern suitable for the insonification of a wide area at a safe standoff distance. At the frequencies of greatest interest to the methods of mine detection discussed in this thesis (i.e. less than 250 Hz), it is quite capable of insonifying the width of a typical thoroughfare.

Though measurements indicated a faster falloff along the axis than predicted, the array still appears capable of delivering high amplitudes (i.e. no more than 20 dB lower than the source strength) at distances of up to 10 m. Subwoofers positioned directly over the mine can be used for experimental investigation of the nonlinear effects of higher levels of insonification, though this setup sacrifices the standoff capabilites of the sixteen-speaker array, and thus is not as suited to a practical field implementation.

Chapter 4

Experimental Measurements on the Mine/Soil System

In this chapter, the behavior of the mine/soil system is investigated experimentally. The mine simulant itself as well as instrumentation for observing the velocity of the soil surface and the compliant, resonant lid is described in Sec. 4.1. Section 4.2 describes investigations of the resonant behavior of the buried and unburied lid. Basic tests for the observation of nonlinear response to bifrequency insonification are described in Sec. 4.3, including a digression on pulsed excitation. An exploration of the effect of excitation amplitude on nonlinear responses in the mine/soil system is presented in Sec. 4.4, and comparison with the results obtained with the lumped-element model of Chapter 2 is made in Sec. 4.5.

4.1 Equipment

This section describes the equipment and instrumentation used to insonify the mine/soil system and measure the velocity of the mine lid and the soil above the mine. Manufacturers' specification sheets for the sensing equipment, amplifiers, and speakers can be found in Appendix B.

4.1.1 Mine Simulant

The mine simulant used in these experiments was an inert replica of an Italian VS-1.6 anti-tank mine from Inert Products, LLC. This replica was originally a solid heavyweight plastic structure. In order to give the simulant compliant behavior similar to an actual landmine, the lid area of the replica was sliced of with machine tools

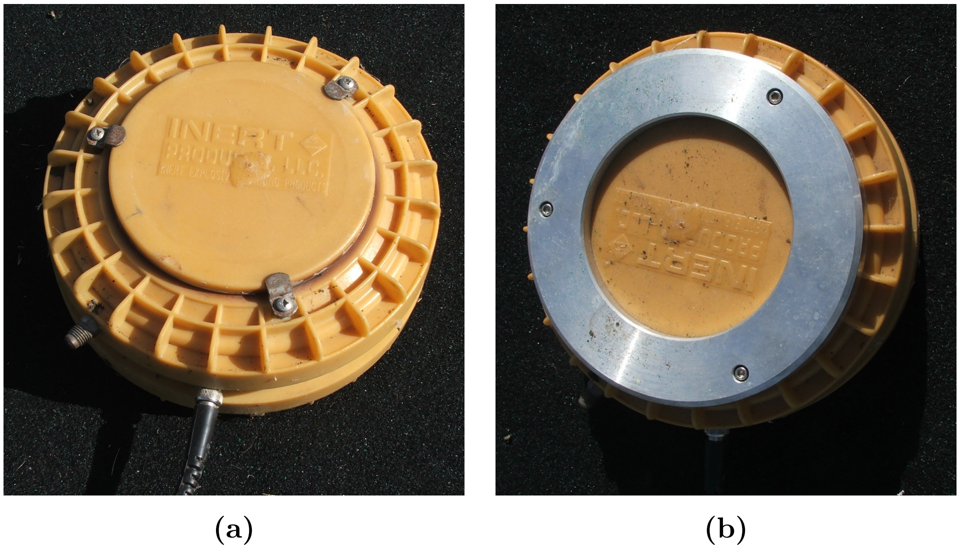
(a) (b)

Figure 4.1: Photographs showing different mechanisms for securing the mine lid to the casing. (a) “Tab” method, which secures the lid at three points using aluminum tabs. (b) “Ring” method, which secures the lid using a steel ring to give a more uniform boundary condition along the edge of the lid.

and made ready to be reaffixed as a compliant lid, while the area underneath was hollowed out to a depth of 4.5 cm, leaving a small cylindrical air-filled volume when the lid was reaffixed. The circular lid has a diameter of 14.2 cm and is 0.8 cm thick, and the total volume of the internal cavity is 680 cc. The lid can be held on to the main body of the mine simulant either by an aluminum ring around its perimeter, or by three small steel tabs. Both of these were secured by screws inserted into three holes drilled into the solid part of the mine casing, and anchored by metal nuts within the casing. These different methods for securing the lid to the casing are shown in Fig. 4.1. A rubber gasket between the lid and the mine casing ensured that the inner cavity was well sealed.

In order to measure the velocity of the mine lid, a Sensor Nederland SM-11 geophone was securely glued to the underside of the lid, as pictured in Fig. 4.2. A BNC connector mounted on a hole drilled from the side of the casing into the interior cavity allows the signal from this geophone to be obtained without interfering with

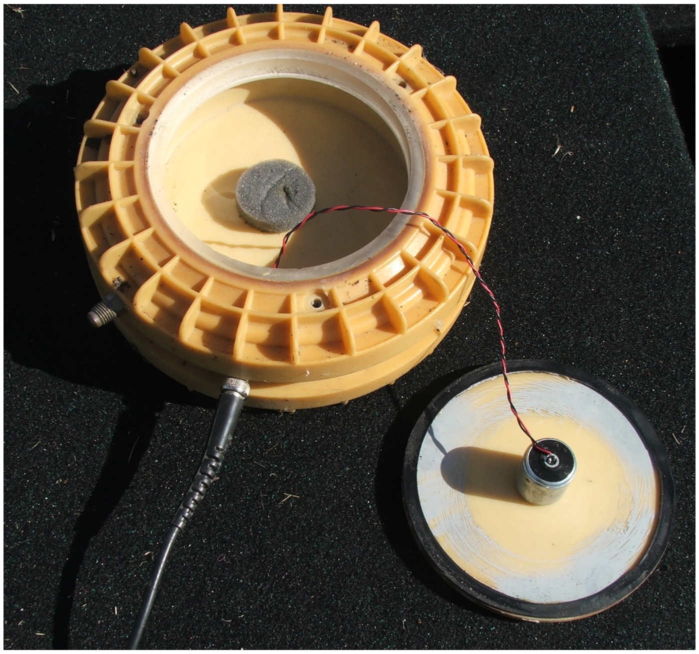

Figure 4.2: Photograph of mine simulant with lid removed to show geophone used to measure lid velocity.

the structure of the lid. This geophone has a resonance frequency of 30 Hz with a spurious frequency of greater than 500 Hz, so it should be appropriate for the excitation frequencies investigated in this thesis.

4.1.2 Ground Geophone

Another Sensor Nederland SM-11 geophone was used to measure the surface velocity of the insonified soil. The geophone was buried with its top just below the surface of the soil to minimize the effect of the direct sound while still measuring the velocity close to the soil surface. The use of a geophone to measure soil surface velocity is less than ideal — its presence in the soil column above the mine adds mass to the system, and it is susceptible to boundary effects similar to those that arise at the mine/soil interface.[†] Additionally, it cannot measure the velocity at the soil surface without being exposed to the acoustic excitation, and thus ends up measuring

---

[†] These issues are described at length by Attenborough et al.[14]

approximately the average ground motion in the upper layer of the ground equal to the geophonone's length of 3 cm. Even so, the use of a geophone is significantly simpler and less expensive than non-contact methods such as Laser Doppler Vibrometry. Throughout this chapter, the sand or soil surface velocity will refer to the velocity measured by the buried geophone.

4.1.3 Insonification

As described in Chapter 3, two different sets of speakers were used to insonify the soil above the mine. The first configuration employed the sixteen-speaker standoff array described in Sec. 3.1. In this configuration, the mine was buried 2 m in front of the array on the center axis, where the maximum SPL on the ground from the array was approximately 123 dB (re 20 μPa). The second setup was used to investigate the effects of higher amplitudes of excitation, and employed a pair of subwoofers as described in Sec. 3.3. These were positioned directly above the buried mine as pictured in Fig. 3.8, and gave a maximum SPL above the mine of 145 dB.

4.1.4 Data Acquisition

In general, three time series were measured in each experimental trial: the velocity of the mine lid, which was measured with the geophone inside the lid; the velocity of the soil surface, which was measured with the buried geophone; and the sound pressure near the soil surface, which was measured with the microphone described in Sec. 3.2.2.1. A typical experimental setup with buried mine, ground geophone and microphone is shown from two perspectives in Fig. 4.3. Signals from the microphone, ground geophone and lid geophone were fed into a WaveBook® data acquisition device, which was run using the DASYLab interface. For pulsed excitation, data acquisition could be triggered by a pulse from a function generator that also triggered the function generators to produce simultaneous signals to output to the speakers. Data files from each trial were then analyzed in MATLAB programs written by the author.

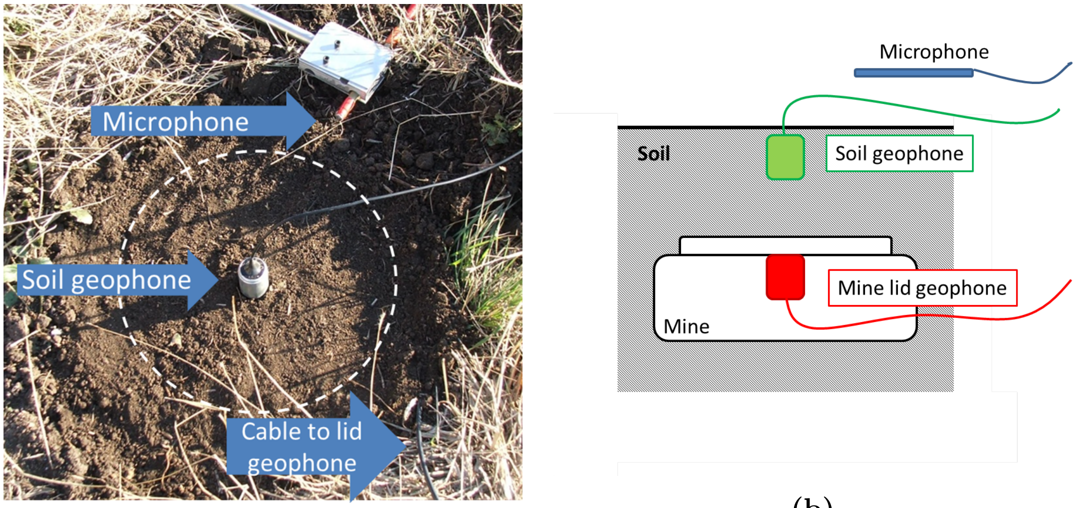

(a)

(b)

Figure 4.3: Illustrations of typical experimental setup. (a) Overhead photograph with the geophone unburied to show its position. The white dotted circle shows where the mine is buried. (b) Cutaway diagram of the setup.

4.2 Investigation of Mine Resonance

Two methods were used to investigate the natural frequency and resonant behavior of the mine lid: measurements of impulse responses, and measurements of impedance as a function of frequency.

4.2.1 Tap Tests

Impulse responses are a simple way to measure the natural frequency of a system. The response of a system to an impulse gives its response across a wide range of frequencies, with a shorter impulse resulting in a wider frequency range.[28] For testing the unburied mine, an impulse was created with a sharp rap off the center of the mine lid using a hard implement such as a pen, and the resulting motion captured by the lid geophone was examined. The FFT of this signal was taken, from which the resonance frequency and resonance peak width could be determined. From these, the quality factor Q could be determined, which is the ratio of natural frequency to the bandwidth:

$$Q = \frac{f_0}{\mathrm{BW}}, \tag{4.1}$$

where bandwidth BW is defined by the "half-power" points, which are 3 dB below the peak spectral response. The quality factor indicates the amount of damping in the system — a higher value of Q indicates less damping. An example of the time-domain signal and frequency spectrum for one of these trials can be seen in Fig. 4.4(a). The mechanism by which the lid was attached to the casing had some effect — when the ring was used instead of the three tabs, the natural frequency was higher and the bandwidth was wider. Though the torque on the bolts used in the different clamping methods was not checked, the higher resonance frequency in the ring case was likely due to the ring holding the lid with a tighter, more uniform constriction.

The resonant behavior of the buried mine lid was also investigated. In this case, the mine was buried in 5 cm (2 in.) of sand or soil, a common depth for buried mines in the field.[29] To obtain the impulse response in this case, the area immediately above the buried mine was sharply slapped by hand, and the resulting motion was analyzed as described previously. Examples of the time series and frequency spectrum obtained from these trials can be seen in Fig. 4.4(b). The natural frequency of the buried lid/soil system was significantly lower than the natural frequency of the unburied lid, and the bandwidth of the buried mine's response was somewhat wider as well, resulting in quality factors near 1 for each buried case. The results summarized in Table 4.1 reveal strong damping due to loading by the overlying soil, with quality factors ranging from about 1 for the buried mine in both sand and soil to 4 for the unburied mine.

One potential issue with these results is that a constant impulse is not realized with the manual excitation method used. The amplitude of the impulse should not matter in a linear system, but nonlinear tuning curves reported by Korman et al.[10] show that the natural frequency of the buried mine can change with excitation amplitude. Specifically, higher amplitudes corresponded to a downward shift in natural

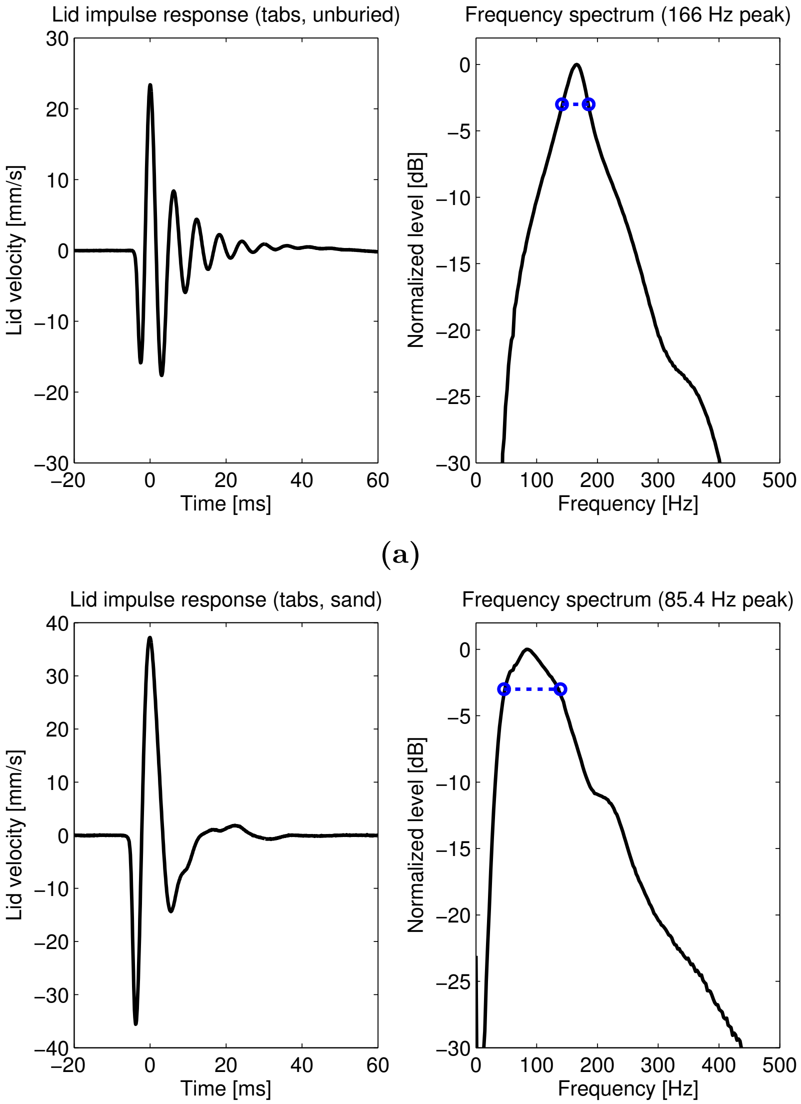

(a)

(b)

Figure 4.4: Examples of time-domain response and corresponding frequency spectra for "tap tests" carried out on the mine lid. (a) Results for the tab-affixed lid with no soil covering. (b) Results for the tab-affixed lid under 5 cm of sand. The blue dotted line in the frequency-domain plots indicates the width of the peak at 3 dB down.

	Natural Frequency [Hz]	Bandwidth [Hz]	Q factor
Unburied, Tabs	168 ± 3	46 ± 5	3.7 ± 0.4
Unburied, Ring	218 ± 11	69 ± 17	3.2 ± 0.8
Sand, Tabs	83 ± 11	84 ± 7	1.0 ± 0.2
Sand, Ring	84 ± 7	107 ± 18	0.8 ± 0.1
Soil, Tabs	96 ± 9	95 ± 8	1.0 ± 0.1
Soil, Ring	79 ± 15	83 ± 19	1.0 ± 0.3

Table 4.1: Mine lid natural frequency and spectral response bandwidth at 3 dB down under different burial conditions and methods for affixing lid to casing. Each entry is the result of at least three trials.

frequency. However, these shifts are only 5–10 Hz over a five-fold increase in amplitude. Our results obtained through the tap tests thus should not differ widely as a result of different amplitudes. Other sources report the natural frequency of an unburied VS-1.6 antitank mine to be 220 Hz,[9] which matches our results most closely for the ring affixment method.

4.2.2 Admittance Test

Another method of determining the resonance of the system experimentally is to measure the admittance of the mine/soil system as a function of incident excitation frequency. Acoustic admittance Y is the inverse of acoustic impedance Z, which makes the admittance the ratio of velocity v to acoustic pressure p (in the frequency domain):

$$Y = \frac{1}{Z} = \frac{v}{p} \tag{4.2}$$

A peak in the admittance indicates a resonance — maximum motion is being obtained for the least magnitude of incident pressure.

The admittance of the mine/soil system can be easily measured by using the microphone to measure the acoustic pressure at the soil surface and the buried geophone to measure the soil surface velocity. The admittance of the mine lid can also be measured by observing its velocity with the lid geophone. We recorded the amplitude of

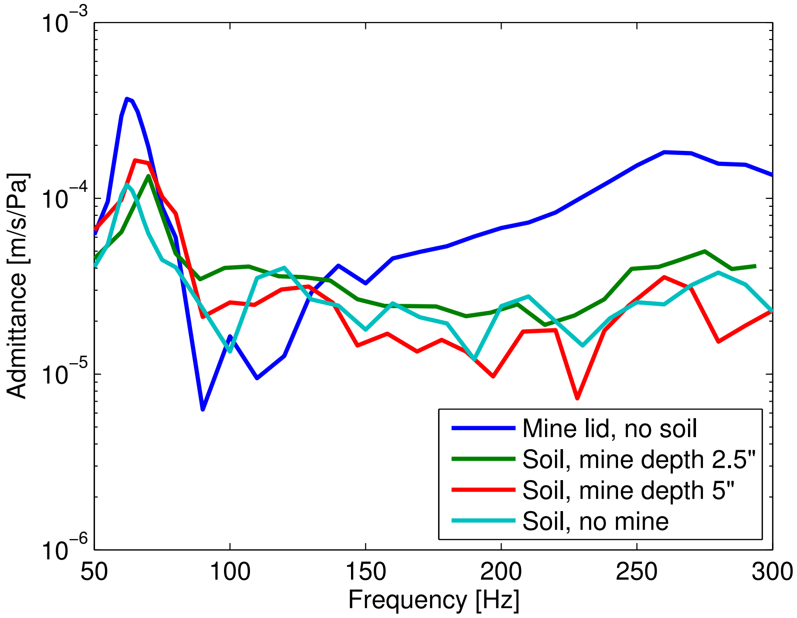

Figure 4.5: Admittance of the mine/soil system as a function of frequency for different burial conditions. The mine lid is attached to the casing using the ring method.

oscillation at increments of the excitation frequency of 5–10 Hz, decreased to 2 Hz in the 60–80 Hz range near the most noticeable peak. Figure 4.5 shows the admittance of the mine/soil system for different depths of mine burial, graphed as a function of excitation frequency. For these results, the mine lid is affixed to the casing via the ring method. Admittance at the soil surface is included when the mine is buried at depths of 2.5 inches and 5 inches, as well as when there is no mine buried. The admittance measured for the unburied mine lid is also included.

Some unusual effects are found in these results. Most noticeable is the presence of a peak near 70 Hz in every case, with a quality factor of ~ 7 in each case except for the 5-inch burial, where $Q \simeq 5$. This would appear to indicate a resonance in the geophone, as the geophone is the only constant in every case. However, the manufacturer's information for the geophone[†] indicates that the geophone's natural frequency is 30 Hz, which should imply a flat response above that frequency. The

---

[†] See Appendix B for the manufacturer's specification sheet.

70 Hz resonance observed for a mine buried in 2.5 inches of soil is within one standard deviation of the 79 Hz resonance of the mine buried in 5 cm (2 in.) of soil as reported in Table 4.1. However, the quality factor in this case is ~ 7, significantly different from the quality factor of ~ 1 found by impulse response. The curve for the unburied mine also indicates a peak around 265 Hz with a quality factor of ~ 4. Another possible cause of the 70 Hz resonance could reflections in the soil cavity between the lid and soil surface, or within the hard (relative to the disturbed filling soil) walls of the cavity, though this would change somewhat between trials, and would not have an effect on the unburied lid. Note also that these tests measured the admittance of the system at the soil surface, whereas the tap tests of Sec. 4.2.1 measured the admittance of the system from the lid.

4.3 Basic Nonlinear Tests

Initial tests with bifrequency excitation were carried out to investigate whether nonlinear effects could be generated and observed in the mine/soil system with our equipment. These tests involved insonifying the system with two frequencies and observing the velocities of the ground and the mine lid with geophones. The presence of sum frequencies and other frequencies that arise due to nonlinear interactions could then be observed by taking the Fast Fourier transform (FFT) of the velocity signals and examining the resulting spectra. The primary frequencies (f_1 and f_2, with $f_1 < f_2$) can then be identified by the most prominent peaks in the frequency spectrum, as well as harmonics ($2f_1$ and $2f_2$) and other frequencies that are simple combinations of the primaries, such as the sum frequency

$$f_\Sigma = f_1 + f_2 \tag{4.3}$$

and intermodulation frequencies (using Donskoy et al.'s notation[13])

$$f_{\mathrm{IM1}} = 2f_1 - f_2 \tag{4.4}$$

$$f_{\mathrm{IM2}} = 2f_2 - f_1, \tag{4.5}$$

as well as other possible intermodulation frequencies at linear combinations of the two primary frequencies (e.g. $3f_1 - f_2$, $2f_1 + 2f_2$, etc.). Two pairs of drive frequencies were used in the trials in this section: 200 and 220 Hz, which fall near the resonance of the unburied mine, and 150 and 175 Hz, which fall near an initial assessment of the buried mine resonance.

The amplitude of excitation for each trial in terms of sound pressure level above the mine is determined in one of two ways. The first is to use the RMS pressure amplitude according to the relationship

$$\mathrm{SPL} = 20 \log_{10} \left(\frac{p_{\mathrm{rms}}}{20\,\mu\mathrm{Pa}} \right) . \tag{4.6}$$

However, the presence of two frequencies means that the combined signal is amplitude-modulated, so the simple relation for the RMS value of sinusoidal signals using the peak-to-peak pressure given in Eq. (3.4) can no longer be used. Instead we use the definition of RMS

$$p_{\mathrm{rms}} = \sqrt{\frac{1}{T_b - T_a} \int_{T_a}^{T_b} \left[p(t)\right]^2 dt}\ , \tag{4.7}$$

with the time span of a single beat $[T_{\mathrm{beat}} = T_b - T_a = 1/(f_2 - f_1)]$ determining the limits of integration. The SPL obtained when this value for the RMS pressure is used in Eq. 4.6 is referred to as the overall SPL from here forward.

The other method of obtaining the level of excitation is to find the levels of the individual primaries directly from the spectra, though this method is more susceptible to errors due to inconsistent windowing. In the numerical simulations of Chap. 2, it was possible to perfectly apply a rectangular window to the time series, encompassing an integer number of cycles and beats. However, it proved difficult to do this consistently for the experimental results due to fluctuations in the frequencies generated by the function generators. Because minor changes in the window could greatly affect the spectra, we generally chose to use a Hann window. Although this method gives somewhat less accurate results for the amplitudes of different components, it has the advantage of smoothing out inconsistencies at the beginning and end of the series, making for more consistent results between trials. The Hann window at the nth sample is defined by

$$w(n) = 0.5\left[1 - \cos\left(\frac{2\pi n}{N-1}\right)\right], \tag{4.8}$$

where N is the total number of samples in the series.[30] Figure 4.6 shows an example of the substantially different results obtained when different types of windows are used. The spectrum from an unwindowed signal shown in Fig. 4.6(a) is not significantly improved by the addtion of a rectangular window in Fig. 4.6(b). However, note the significant rise in the noise floor when the rectangular window is misaligned, as in Fig. 4.6(c). The application of a Hann window, shown in Fig. 4.6(d) reduces this floor greatly, allowing individual spectral lines to be easily seen. Spectra throughout this section were obtained by applying a Hann window across the ∼1.25 s duration of the signal, then taking the FFT, resulting in a ∼1 Hz bandwidth in the spectra.

4.3.1 Experimental Results Using Sixteen-speaker Array

In the first set of basic tests, the sixteen-speaker standoff array was used for insonification. For these tests, the mine simulant with the lid attached using the tab affixment method was located on the array axis, 2 m in front of the array. We began by insonifying the bare mine simulant, i.e., without any soil covering it. Figure 4.7 shows results for bifrequency excitation of the unburied mine at 150 and 175 Hz using the standoff array.[†] The overall SPL at the soil surface is 116 dB. The frequency spectrum for the lid velocity of the unburied mine is shown in Fig. 4.7(a). Though strong second harmonics can be seen in the spectrum, no sum frequency is evident. However, the intermodulation frequencies f_{IM1}, f_{IM2} are visible. The first intermodulation frequency is located at 120 Hz, where we would expect the second harmonic of the 60 Hz noise, but the other is located at 205 Hz. Its presence and similar level to that of the signal at 120 Hz suggests that the lid alone has some cubic nonlinearity.

[†] In the figures of this chapter, series and spectra from the pressure signals, lid velocity, and soil surface velocity are represented by blue, red, and green lines, respectively.

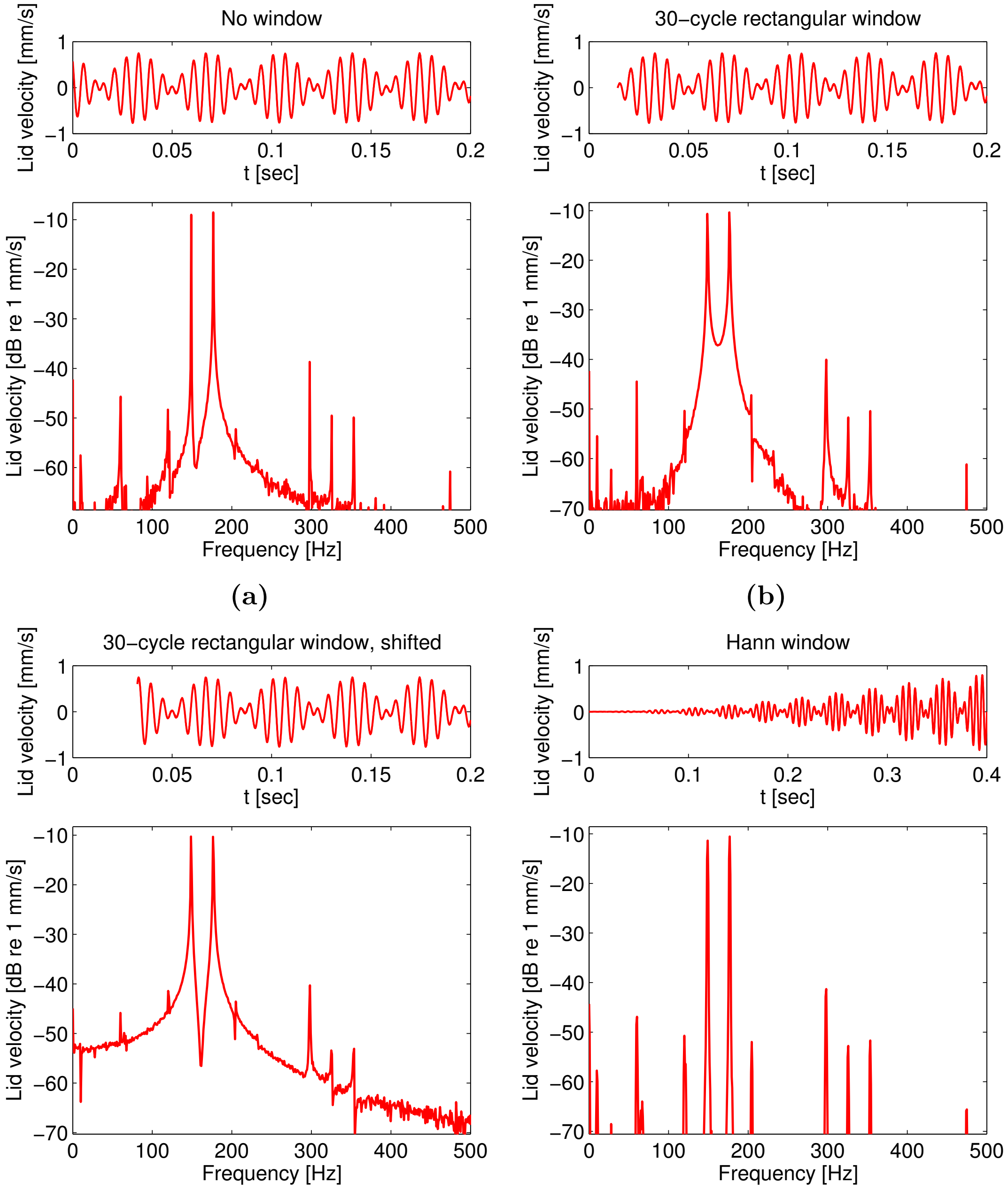

(a) (b) (c) (d)

Figure 4.6: Comparisons of buried mine response with and without windowing. The beginning of the windowed time series of a representative lid velocity signal and corresponding spectra are shown for four different window conditions. (a) Results when no window is applied. (b) Results for a rectangular window with length 30 beats. (c) Results for a rectangular window time-shifted by half the beat length. (d) Results for a Hann window across the entire signal. Note that the time scale in (d) is extended to show the window's shading.

Unfortunately, problems with the ground geophone placement in this series of tests mean that results for the soil surface velocity cannot be shown for comparison.

Figure 4.7(b) shows the spectrum for the acoustic pressure signal, which also displays strong second harmonics. The presence of second harmonics in both the lid velocity spectrum and the acoustic pressure spectrum seems to indicate that the second harmonics are being generated due to nonlinearity in the speakers or amplifiers.[†] This illustrates a primary reason that searching for nonlinear effects with single-frequency excitation is not an ideal method — with single-frequency excitation, harmonics may be generated by nonlinearity at any point in the entire system, including in the signal generator, amplifier, and speakers, as well as in the insonified system. However, with bifrequency excitation, keeping the signals separated until they exit the speakers ensures that the observed interaction frequencies can only have been generated due to nonlinearity in the insonified system itself (including the air).

When the mine was buried under a shallow (2 cm) covering of mortar sand and insonified using the same frequencies and amplitude as in the unburied case just described, a sum frequency component becomes visible between the two second harmonics in the lid velocity spectrum, as can be seen in Fig. 4.8(a). The responses at the intermodulation frequencies f_{IM1}, f_{IM2} are also more prominent than they were in the unburied case. The frequency spectrum for the pressure signal, shown in Fig. 4.8(b), continues to show no sum frequency, so we can be reasonably certain that the sum frequency is being generated in the insonified mine/sand system.

Tests like these were repeated for a variety of burial conditions and insonification frequencies. Both sand and soil were used as fill material, at burial depths of 2 cm and 8 cm measured from the surface of the soil to the top of the mine lid. In addition, the effects of the state of the fill material was investigated by taking measurements

---

[†] Though it may be possible that the second harmonics are being generated in the microphone and geophone, the similarity in the spectra despite the significant difference in the nonlinear behavior of the microphone and geophone appears to indicate generation due to nonlinearity in the insonification system.

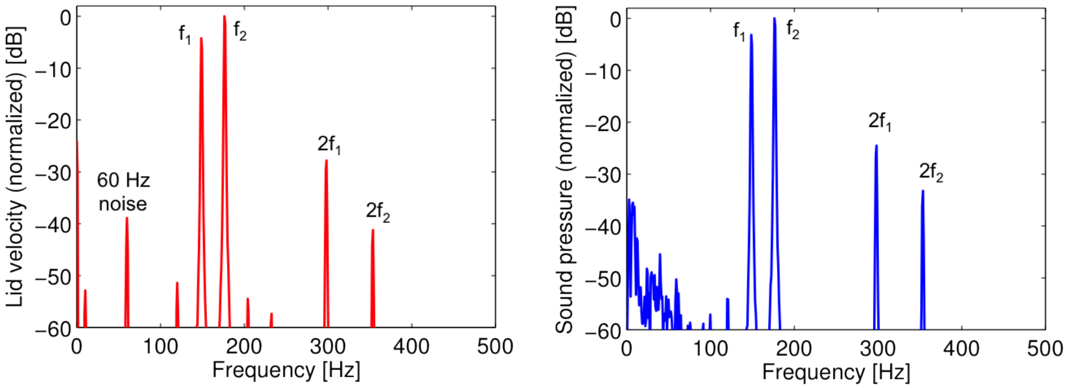

(a) **(b)**

Figure 4.7: Frequency spectra for the unburied mine simulant insonified by the standoff array with primary frequencies 150 and 175 Hz and total SPL at the mine of 116 dB. The scales on the y-axes of the spectra plots are in dB down from the primary frequency component with the highest level. (a) Lid velocity spectrum. (b) Acoustic pressure spectrum in air above the simulant mine case. Though second harmonics are clear in each case, no sum frequency is visible in either spectrum.

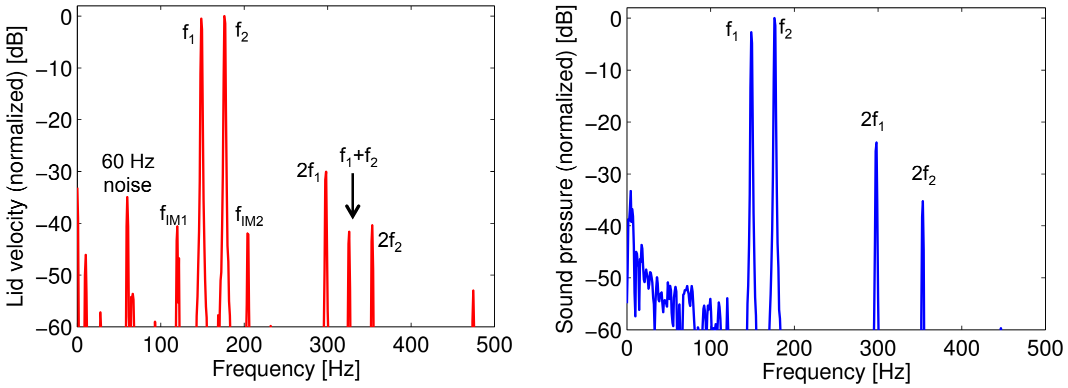

(a) **(b)**

Figure 4.8: Frequency spectra for the mine lid under 2 cm of sand insonified by the standoff array. (a) Lid velocity spectrum. (b) Acoustic pressure spectrum above the buried mine. The presence of a covering of sand causes a sum frequency component to become visible between the two second harmonics in the lid velocity spectrum (compare to Fig. 4.7).

when the covering sand or soil was freshly laid, and again after the mine had lain buried overnight, giving the covering a chance to settle. The effects of the state of the soil were further investigated by taking some measurements with a dehydrated covering of soil. In each case, the frequency spectrum was taken, and the level of the peak at the sum frequency was measured in dB down from the level of the higher of the two sum frequency peaks.

Table 4.2 summarizes the results from these tests. The total SPL above the mine in each of these cases was 111–114 dB. A few general trends can be seen in these results. The relative level of the sum frequency component is less in deep sand than in shallow sand, though depth does not seem to have a great effect for fresh (i.e., moist and unconsolidated) soil. In addition, burial under sand tends to show stronger responses at the sum frequencies, while fresh soil tends to show the weakest responses at the sum frequencies. Of the two pairs of frequencies used (200 Hz and 220 Hz; 150 Hz and 175 Hz), neither consistently results in a stronger response at the sum frequency signal relative to that at the primary frequencies — out of seven burial conditions, four showed a stronger sum-frequency signal for the lower frequency pair, two showed a stronger sum-frequency signal for the higher pair, and one showed sum frequency components that were equal in amplitude. In each case, the response at the sum frequency was lower in amplitude than one or both of the second harmonics. The spectra for each of these trials can be found in Appendix C.

4.3.2 Experimental Results Using Subwoofers

To investigate the effect of higher sound pressure levels on the ground above the mine, the subwoofers described in Sec. 3.3 were employed. The subwoofers were located on the ground directly above the buried mine, and the mine lid was again secured using the tab method. The increased amplitude generated by the subwoofers exposed the nonlinearity in the lid alone, as can be seen in the lid velocity spectrum for the unburied mine insonified by the subwoofers at an overall incident SPL of 130 dB, shown in Fig. 4.9(a). Compare the unburied lid velocity spectrum in Fig. 4.7(a), where

Covering Type	**Depth**	**Primary Frequencies**	**Lid Velocity Sum Freq. Level**
Unburied	0 cm	200 Hz, 220 Hz	Not observed
		150 Hz, 175 Hz	Not observed
Soil (fresh)	2 cm	200 Hz, 225 Hz	−59 dB
		150 Hz, 185 Hz	−61 dB
	8 cm	200 Hz, 220 Hz	−59 dB
		150 Hz, 175 Hz	−61 dB
Soil (dehydrated)	2 cm	200 Hz, 220 Hz	−56 dB
		150 Hz, 175 Hz	−56 dB
Soil (settled)	2 cm	200 Hz, 220 Hz	−47 dB
		150 Hz, 175 Hz	−44 dB
Sand (fresh)	2 cm	200 Hz, 220 Hz	−48 dB
		150 Hz, 175 Hz	−42 dB
	8 cm	200 Hz, 220 Hz	−46 dB
		150 Hz, 175 Hz	−55 dB
Sand (settled)	2 cm	200 Hz, 220 Hz	−46 dB
		150 Hz, 175 Hz	−48 dB

Table 4.2: Results of bifrequency tests using the standoff array to insonify the mine buried under different conditions. “Sum Frequency” column gives the level of the peak at the sum frequency in the lid velocity spectrum in dB down from the primary frequency peaks. Overall excitation levels were 111–114 dB.

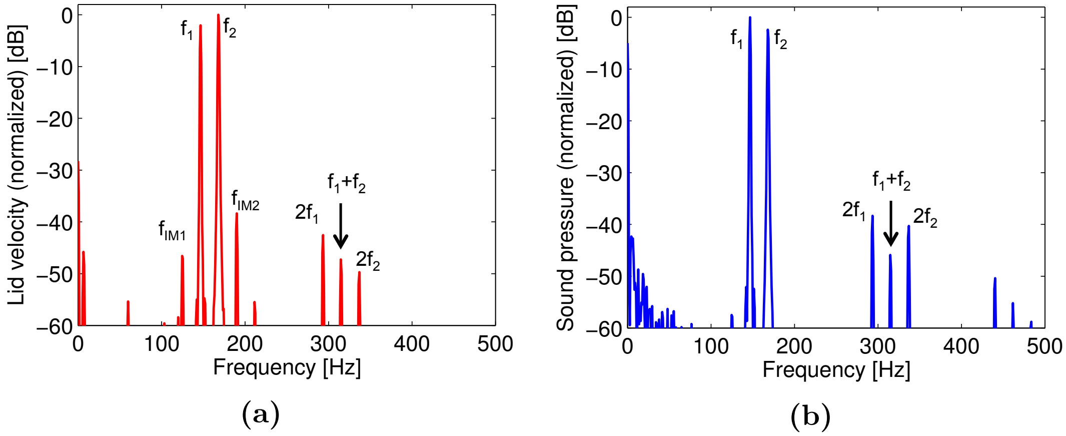

Figure 4.9: Frequency spectra for the unburied mine simulant insonified by the subwoofers with primary frequencies 145 and 170 Hz and overall incident SPL of 130 dB. (a) Lid velocity spectrum. (b) Pressure spectrum. A small sum frequency response in both the pressure and velocity spectra is noticeable due to the increased amplitude causing nonlinear effects in the microphone and geophone themselves.

the overall incident SPL is 116 dB and no sum frequency is visible. The increased amplitude also caused a sum frequency to be generated in the pressure spectrum due to nonlinearity in the microphone itself, shown in Fig. 4.9(b).

When the subwoofers are used to insonify the buried mine, the sum frequency becomes much more prominent, and an increased response at other intermodulation frequencies can be seen. This is evident in the spectra in Fig. 4.10, which show the lid velocity and acoustic pressure spectra for the mine buried under 5 cm of soil and insonified at 150 and 170 Hz with an overall incident SPL of 130 dB. These other intermodulation frequencies occur at linear combinations of the primary frequencies, and are indicative of higher-order nonlinear effects. Additionally, the higher amplitude of the sum frequency, harmonics, and intermodulation frequencies in the buried case vs. the unburied case again points to the primary source of nonlinearity to be the presence of soil above the buried mine. It is interesting to note that the second harmonics and sum frequency in the microphone are slightly higher in the buried vs. unburied case, which could indicate the microphone detecting acoustic pressure

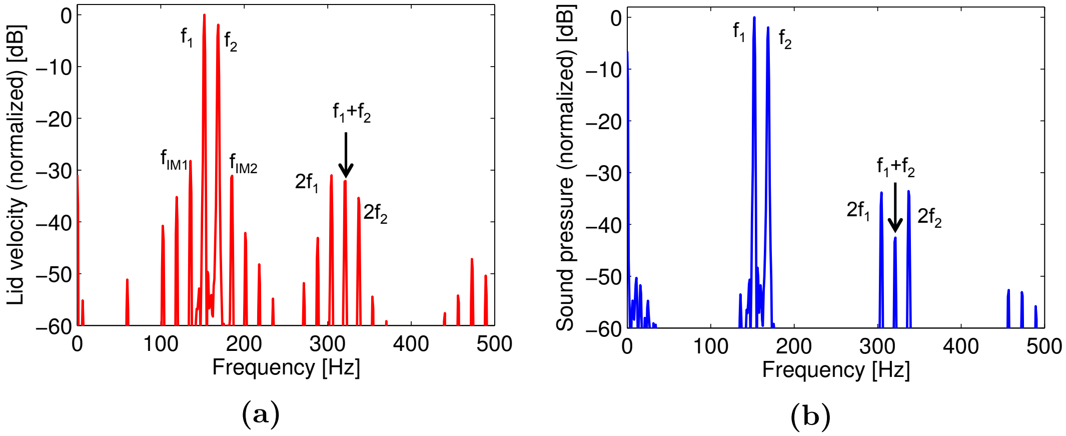

Figure 4.10: Frequency spectra for the mine simulant buried under 5 cm of soil and insonified by the subwoofers with primary frequencies 150 and 170 Hz and overall incident SPL of 130 dB. (a) Lid velocity spectrum. (b) Pressure spectrum. The sum frequency in the lid velocity spectrum is much stronger than in the unburied case of Fig. 4.9, and many other interaction frequencies now have an increased response as well.

variations due to the vibration of the buried mine, though this requires extensive further testing to confirm or deny.

Results from these tests are given in Tab. 4.3. These were not as exhaustive as the results from the sixteen-speaker array shown in Tab. 4.2, as they were intended primarily to set the stage for the amplitude response tests described in Sec. 4.4. Some interesting trends can be noticed, however. The highest frequency pair (200 and 220 Hz) seems to be significantly less effective at exciting high-level sum frequency responses, probably because it is farther from the mine's resonance. No significant difference between fresh and settled soil can be seen here. The levels of the sum frequency response are significantly greater than those reported for the results of lower-amplitude excitation, however. The spectra for each of these trials can be found in Appendix C.

Overall, the results of these basic tests compare well qualitatively with the nonlinear effects observed in similar tests by Korman et al.[10] Their results are reproduced in Fig. 4.11. That particular test excited a buried Italian VS-2.2 landmine at an overall

Covering Type	Depth	Primary Frequencies	Lid Velocity Sum Freq. Level
Unburied	0 cm	150 Hz, 170 Hz	−47 dB
		200 Hz, 220 Hz	−61 dB
Soil (fresh)	5 cm	150 Hz, 170 Hz	−30 dB
		75 Hz, 85 Hz	−34 dB
		195 Hz, 215 Hz	−40 dB
Soil (settled)	5 cm	150 Hz, 170 Hz	−32 dB
		100 Hz, 250 Hz	−34 dB

Table 4.3: Results of bifrequency tests using the subwoofers to insonify the mine buried under different conditions. "Sum Frequency" column gives the level of the peak at the sum frequency in the lid velocity spectrum in dB down from the primary frequency peaks. Overall excitation levels were 126–130 dB.

SPL of 105 dB and primary frequencies $f_1 = 165$ Hz and $f_2 = 175$. (Our landmine is an Italian VS-1.6, which is slightly larger.) The soil surface velocity spectra show a strong sum frequency and second harmonics directly above the buried mine, but only the primaries and weak intermodulation frequencies remain when the soil velocity is measured off the mine, that is, on undisturbed soil. Their tests also indicate sideband lines in the primary excitation for their buried mine measurement. This effect was observed in our measurements for the lid velocity spectrum, but not in the acoustic pressure spectrum for the microphone above ground.

4.3.3 Tone Burst Insonification

The limited duration of a tone burst allows us to use higher sound pressure levels for insonification without fear of damaging the loudspeakers, in addition to being less obtrusive to operators and bystanders than continuous waves. However, the use of bursts requires careful attention to signal processing in order to obtain meaningful spectra, as the short duration of bursts means that the resolution in the frequency domain is less. As discussed in Sec. 2.2.2, an ideal rectangular window contains a perfectly repeating waveform. In multifrequency cases like ours, the frequencies

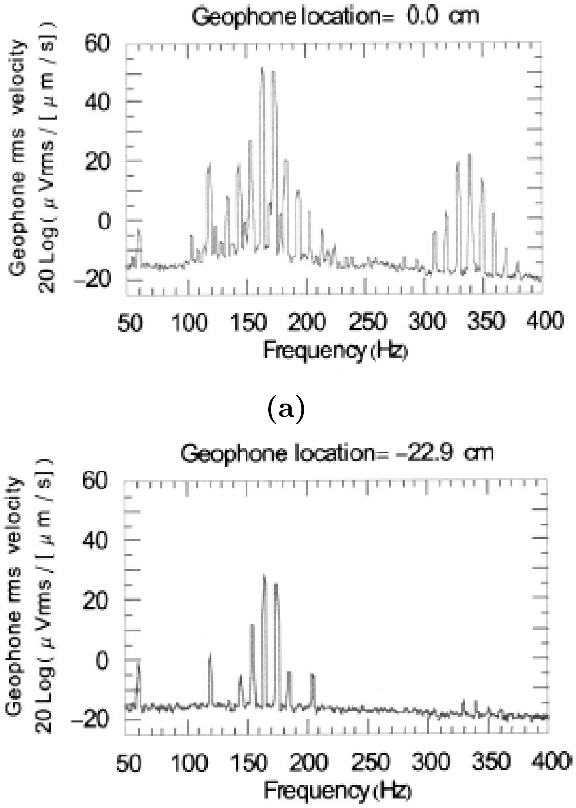

(a)

(b)

Figure 4.11: Nonlinear results of Korman et al.[10] Soil velocity spectra for bifrequency excitation of $f_1 = 165$ Hz and $f_2 = 175$ Hz and overall SPL of 105 dB. (a) Soil velocity spectrum above buried mine. (b) Soil velocity spectrum far from mine (i.e., on undisturbed soil).

involved must be carefully chosen integer multiples of each other in order for the waveform to repeat within a reasonable amount of time. This was difficult to achieve in practive due to the imprecision of our function generators — the frequency output of each generator did not match exactly the displayed frequency, and the degree of discrepancy would vary from day to day. Because each function generator was capable of producing only a single-frequency tone burst with an integer number of cycles, the overall time length of the pulses from each generator could be slightly different, resulting in a short single-frequency "overhang" at the end of each pulse. An extreme example of this issue is shown in Fig. 4.12, though the overhang could be easily minimized to less than one cycle by adjusting pulse counts. One way this could be overcome would be to somehow gate the function generators, effectively multiplying each output by a rectangular wave of the desired pulse duration, though this would result in part at least one component being cut off mid-cycle. In any case, the application of a window such as a Hann window can help to smooth out these inconsistencies. Figure 4.13 shows some examples of windowing for bursts of different length. The type of window cannot make much of a difference for very short bursts, as in Figs. 4.13(a) and 4.13(b). However, when applied to a longer window as in Figs. 4.13(c) and 4.13(d), the Hann window allows better distinction between peaks. In practice, we found a bifrequency pulse with five "beats" to be ideal — this is the minimum duration at which decent resolution is obtained. Bursts of this duration with a Hann window applied were used to conduct the experiments in the following section. However, dual frequency tone bursts of durations that are longer yet would have reduced the significance of the pulse overhang problem and given sharper spectral lines in the frequency spectra, and should be considered in future work.

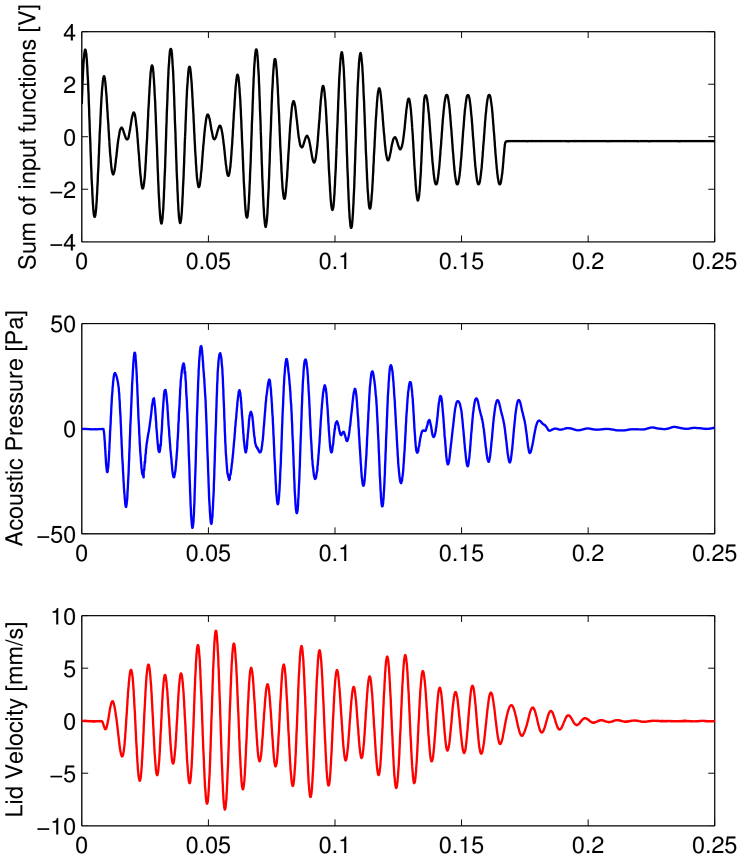

Figure 4.12: Example of a misaligned bifrequency tone burst, including the sum of the input signals and time-domain responses from the microphone and unburied mine lid. Primary frequencies are 120 Hz and 145 Hz. Note the single-frequency overhang at the end of the burst.

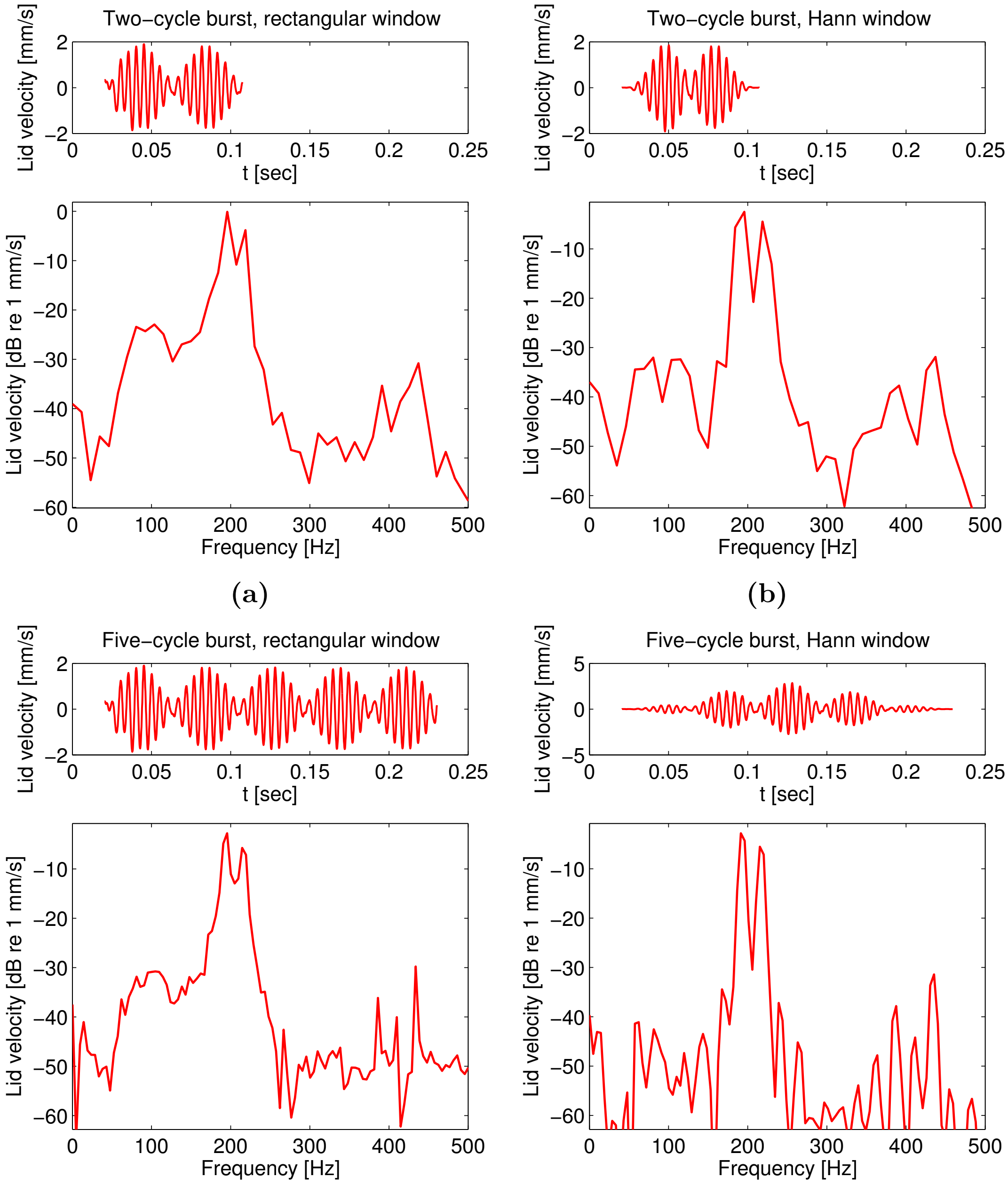

(a) **(b)**

(c) **(d)**

Figure 4.13: The effects of different types of windows on long and short bursts with primary frequencies 190 Hz and 215 Hz. Two-beat bursts are shown in (a) and (b), while five-beat bursts are shown in (c) and (d). The rectangular window applied in (a) and (c) gives somewhat jagged spectra, and the Hann window applied in (b) and (d) results in much more distinct spectral lines, especially close to the primaries.

4.4 Amplitude Response

The increased amplitudes obtainable with the subwoofers raised important questions about the minimum amplitude necessary to observe nonlinear effects. In a practical mine detection application, it would be advisable to minimize amplitude in order to use less energy, as well as to avoid interfering with the detection mechanism. To investigate the effects of excitation amplitude, we insonified the mine/soil system with bursts of five envelope cycles at a fixed frequency pair using the subwoofers, and recorded how the amplitudes of the primary frequency components and the sum frequency component changed as the overall amplitude of insonification varied. Preliminary tests were performed at a few representative frequency pairs, but the pair of 90 Hz and 110 Hz gave the highest amplitude responses for any given excitation amplitude (implying that it is closest to the resonance of the buried mine), so it was chosen for in-depth investigation. These tests investigated the ground surface velocity and lid velocity when the mine was buried, as well as ground surface velocity when no mine is present and lid velocity when the mine is unburied. The pressure spectra during each of these trials were also measured. To minimize transient effects from wind and other noise, three measurements were made for each amplitude setting. The levels at the sum frequency peaks could then be obtained from the FFT of the average of the time series from these trials. The averaged spectra from which the following figures were derived can be found in Appendix C.

Figures 4.14 and 4.15 show the levels of the primary components and sum frequency components in each signal as a function of the overall incident SPL (as described in Sec. 4.3) for burial in soil and sand, respectively. Primary and sum frequency components are shown for the pressure, the lid velocity, and the ground surface velocity. Each point represents the average of three trials. In the pressure (microphone) plots, the primary frequency component level and sum frequency component level increase linearly with excitation level, with the sum frequency component level increasing at roughly twice the rate of the primary frequency component level. This is expected for a system with primarily quadratic nonlinearity. In addition, the results for the microphone signal remain essentially the same no matter the ground material or mine presence, indicating that any acoustic pressure variation caused by the vibration of the ground is negligible, at least given our current setup and analysis. The curves for the unburied lid velocity are very similar in each case, as expected, with the exception that the slope of the sum frequency levels is slightly higher in the soil case. This is probably due to inconsistent placement of the unburied mine relative to the speakers.

Some unusual results are found in the measurements in sand. When the mine is buried in sand, the level of the primaries for both the mine velocity and the ground surface velocity increases more rapidly above an incident SPL of 130 dB. Previous investigations have revealed an effect of excitation amplitude on the resonance frequency of the buried mine,[10] so it is possible that higher excitation levels bring the resonance frequency closer to the frequency of excitation. However, such a sudden shift would not be expected if this were the case. In addition, the sum frequencies in the sand surface velocity spectrum level off above 130 dB when no mine is present. Another unexpected observation is that in both the sand and soil cases, the primary frequency component in the ground surface velocity measurements when no mine is present increases with a slope in the range of only 0.72 to 0.75. This indicates absorption or some other loss of energy, though it is odd that this does not occur when a mine is present. A general trend is that only the cases where sand or soil is included show kinks in the curves. In the results from the pressure signals as well as from the velocity of the unburied mine lid, the curves are fairly straight. This highlights the highly nonlinear nature of soils.

With the set of experiments just described, we are able to compare the ground surface velocity above a buried mine to the ground surface velocity over an area without a buried mine. This comparison is shown in Fig. 4.16. Some unexpected phenomena result. In soil, the sum frequency amplitude is greater when there is no mine buried than when a buried mine is present. This probably has to do with the soil itself — as mentioned in Sec. 2.1, the nonlinearity of geomaterials such as soil

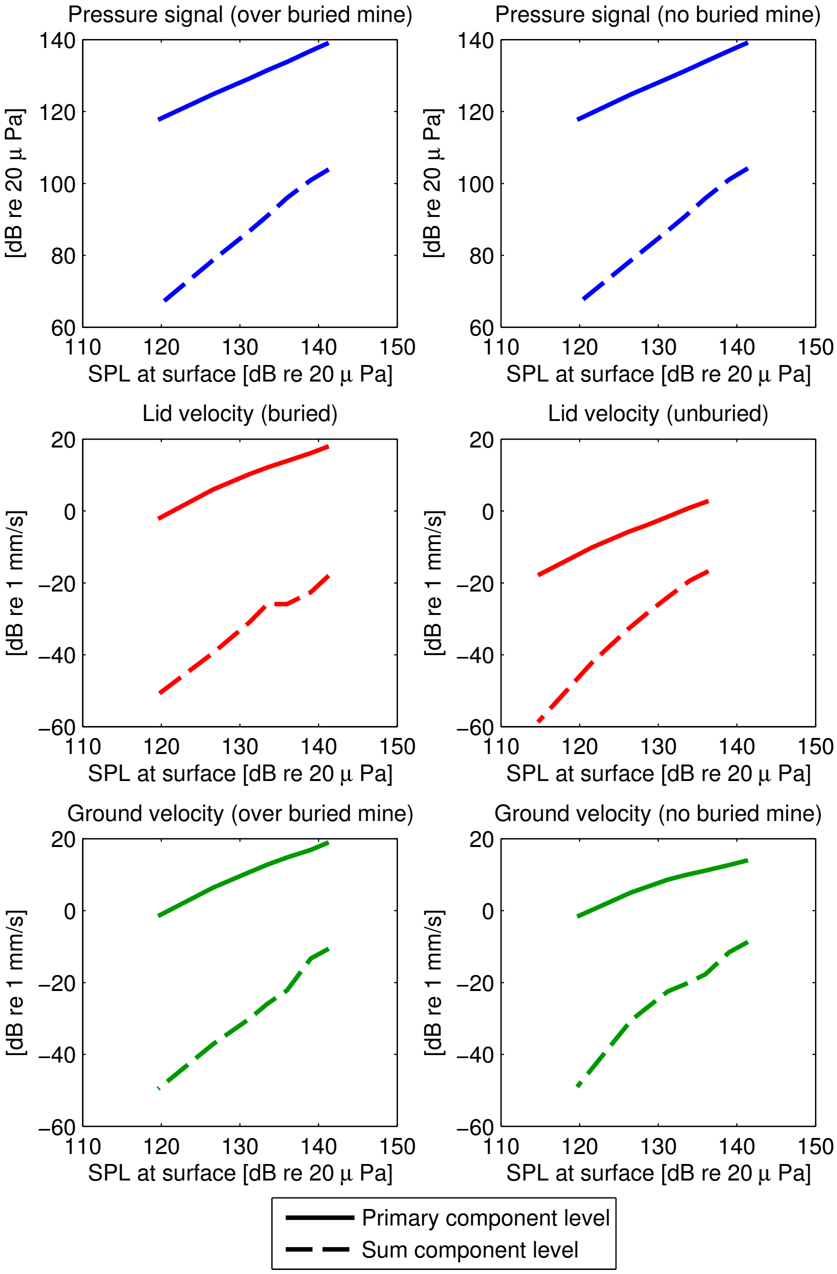

Figure 4.14: Levels, as a function of incident SPL, of primary frequency and sum frequency components of pressure signal, lid velocity, and ground surface velocity for burial under 5 cm soil. Primary frequencies are 90 Hz and 110 Hz.

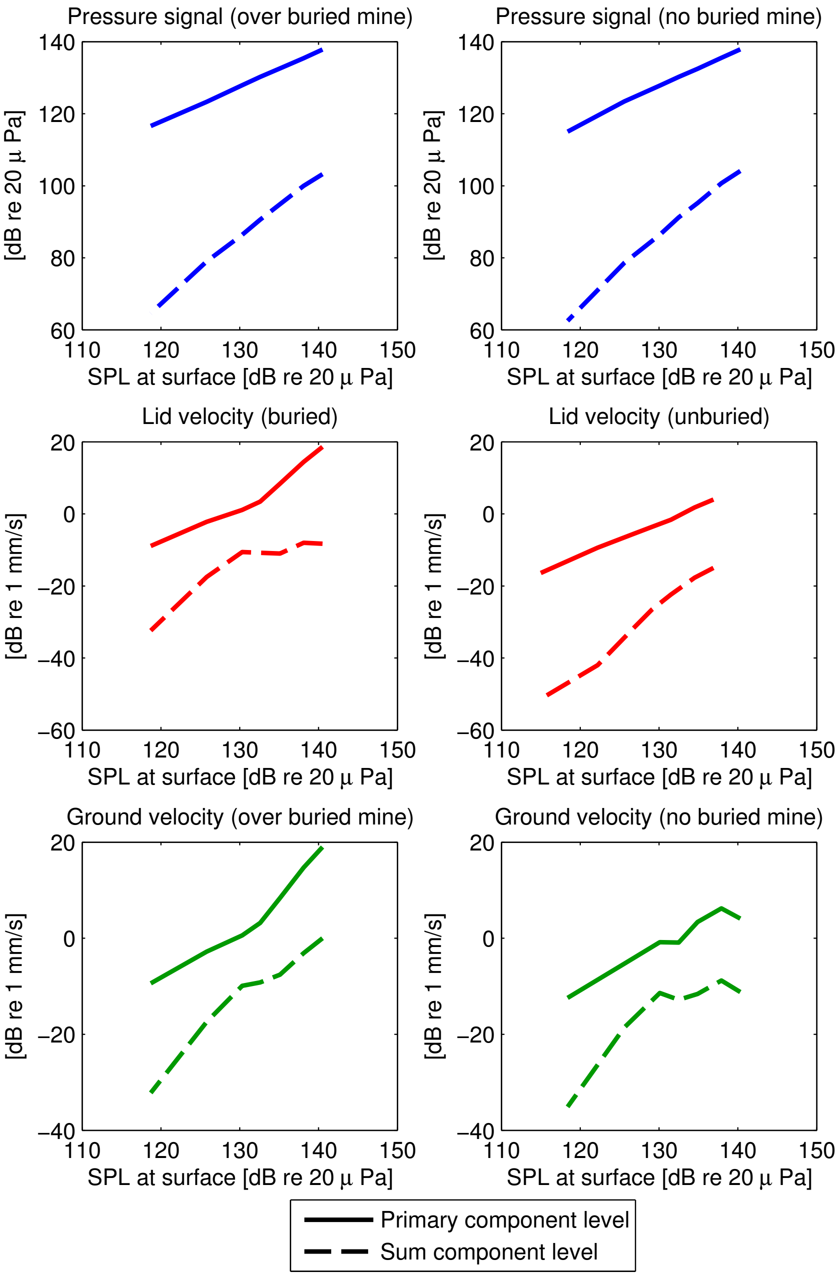

Figure 4.15: Levels, as a function of incident SPL, of primary frequency and sum frequency components of pressure signal, lid velocity, and ground surface velocity for burial under 5 cm sand. Primary frequencies are 90 Hz and 110 Hz.

may be affected greatly by a number of variables including moisture and compactness. Though care was taken when unburying the mine and replacing the soil to use the same soil and compact it by the same amount, the mere act of disturbing the soil unavoidably changed its nonlinearity. The results for the trials in sand are somewhat more expected — the sum frequency level is nearly the same in the mine and mineless cases, but above 130 dB becomes greater in the presence of a mine, while it levels off when no mine is present. This implies some sort of saturation of the nonlinear effects in the sand itself, though further experiments would be necessary to confirm this. When the level of the sum frequency component is compared to the level of the primary, some further unusual results occur. In sand, the highest level of the sum frequency component relative to the primary occurs at an overall incident SPL of 130 dB, decreasing at higher incident SPLs. This is the case for the ground surface velocity both in and without the presence of a buried mine. It is possible that the resonance of the sand column is shifting with amplitude, and an incident SPL of 130 dB marks the point where the changing resonance frequency matches the frequencies of insonification or the sum frequency. Again, further investigation is required before any definitive statements are made.

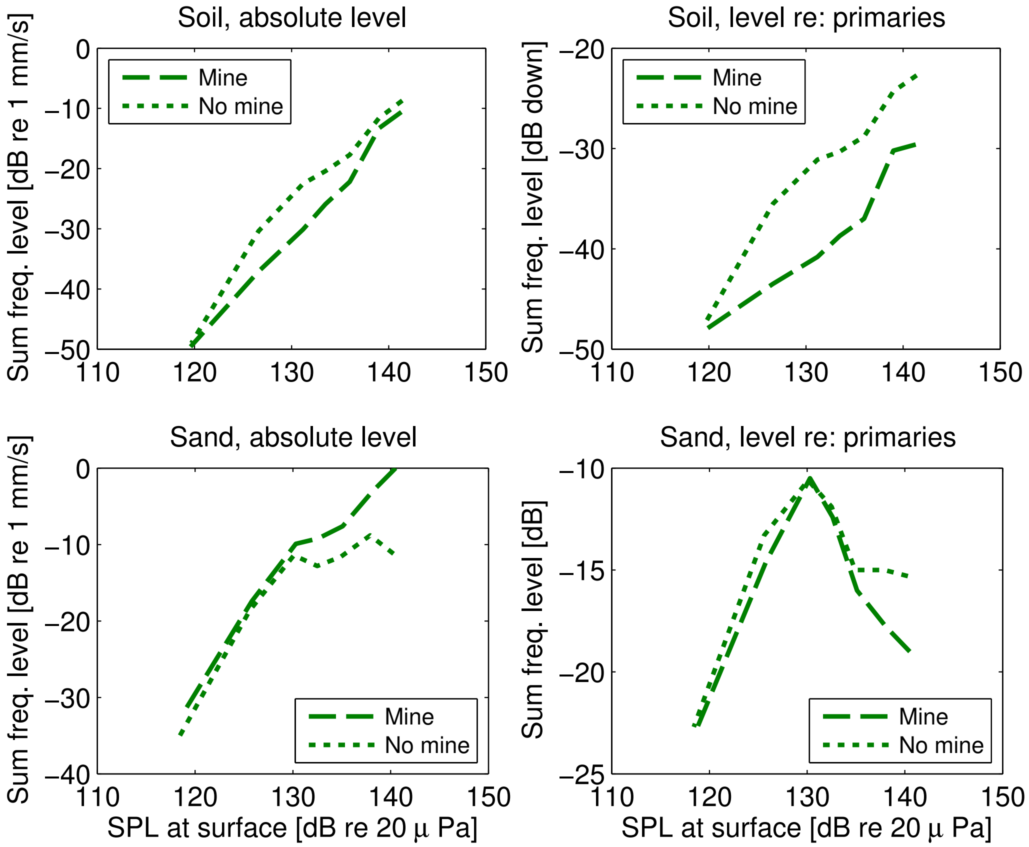

Figure 4.16: Amplitudes of sum frequency components in the ground surface velocity spectrum as a function of the overall SPL at the surface. The left column shows the actual amplitudes of the sum frequencies, while the right column shows the sum frequency amplitudes in dB down from the primary frequency amplitudes. Primary frequencies are 90 Hz and 110 Hz.

4.5 Comparison with Models

Chapter 2 introduced a lumped-element model of the mine/soil system. Though a quantitative assessment of the accuracy of this model is infeasible given our lack of information about the parameters of our physical system,[†] qualitative comparisons can be made between the spectra obtained via numerical solution and via experimental measurement. Figure 4.17(a) shows the experimentally obtained ground surface velocity spectrum for excitation at 90 Hz and 110 Hz with an incident pressure amplitude of 100 Pa (130 dB), with the mine buried under 5 cm of sand. Representative spectra from the numerical time-domain solution to the model are shown in Fig. 4.17(b)–(d). As shown in Fig. 4.17(b), the bimodular nonlinearity in Eq. (2.2) with a strong kink ($\gamma = 0.1$) is a fairly good qualitiative match for the measurement. Spectra from the model using classical nonlinearity are shown in Figs. 4.17(c) and 4.17(d). The parameters are unchanged from those listed in Table 2.1, though the excitation amplitude is increased significantly to 100 Pa in Fig. 4.17(c) to match the measurement. This increased amplitude causes distortion even greater than that seen in the measurement, though reducing the amplitude to 10 Pa as shown in Fig. 4.17(d) yields a spectrum that matches the measurement more closely. An exact match is not expected as the parameters used are not tailored to our measurement conditions; however, this comparison indicates either weaker classical nonlinearity in our system than was found by Donskoy et al.,[13] or the presence of fairly strong bimodular nonlinearity. In any case, further directed investigation is needed to judge the type of nonlinearity that best represents that present in the physical system.

[†] The model uses shear and compressive compliances and resistances for the soil, as well as the compliance and resistance of the mine lid, as well as masses for both lid and soil. The soil mass may be determined by measuring its density, and the compliances and resistances may be determined by measuring compressive and shear wave speeds and finding the associated moduli.

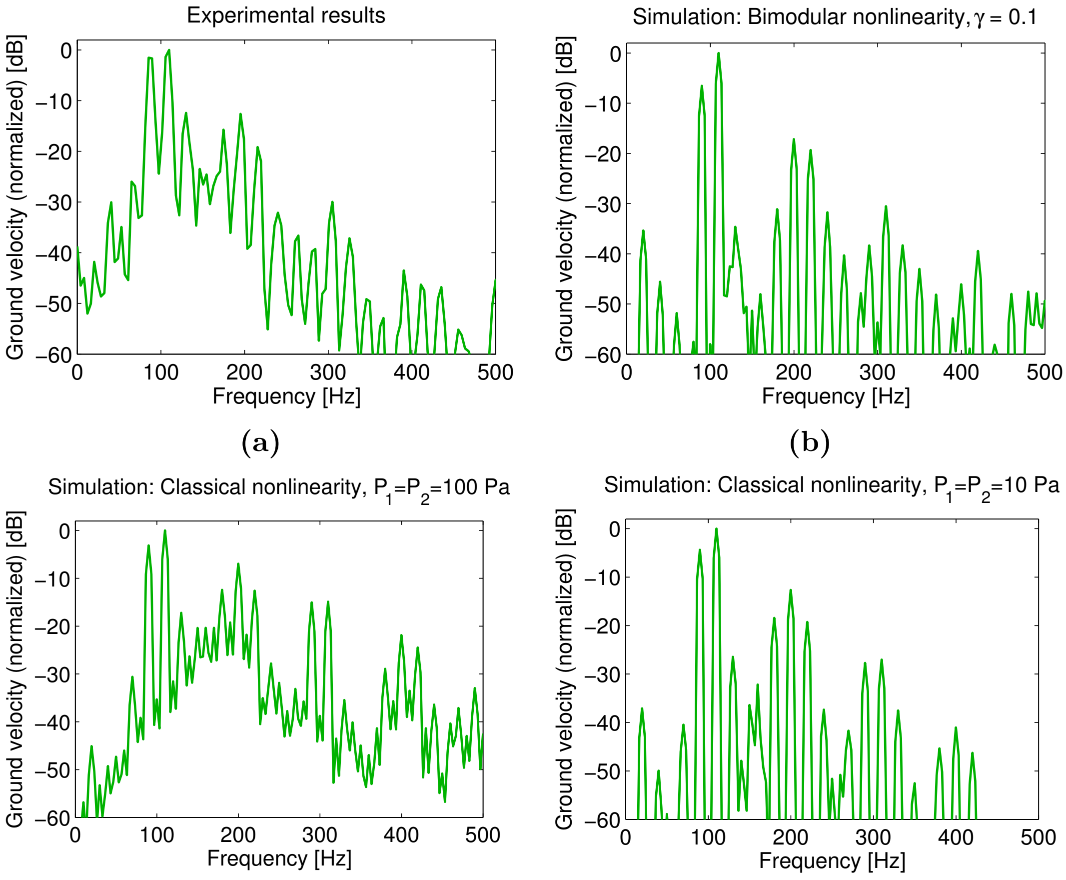

(a) (b) (c) (d)

Figure 4.17: Comparison of experimental and simulated spectra. (a) Experimental results: normalized ground surface velocity spectrum for excitation at 90 Hz and 110 Hz, 100 Pa (130 dB), and the mine buried under 5 cm of sand. (b)–(d) Simulated results: (b) Bimodular nonlinearity, $\gamma = 0.1$. (c) Classical nonlinearity, amplitude 100 Pa. (d) Classical nonlinearity, amplitude 10 Pa. Recall that the shape of the frequency spectrum resulting from bimodular nonlinearity is independent of amplitude, and therefore amplitude need not be reported for the simultation in (b).

4.6 Conclusion

The experiments and measurements described in this chapter have reexamined and expanded on previous work in part, as well as exposing areas for potential future investigations. Our standoff array was shown to be capable of exciting and observing nonlinear effects in the mine/soil system, and the subwoofers were used to focus in on nonlinear effects and details at higher amplitudes. These nonlinear effects were clearly observed to increase when the mine was buried, though the present experiments did not show whether this increase was due primarily to the interaction between the soil and lid, as theorized by some,[10, 13] or to the nonlinearity of the soil itself. While other researchers[10] have found clear indications of increased nonlinearity in the presence of a buried mine, our measurements have highlighted the obfuscating effects of the soil nonlinearity. The amplitude tests of Sec. 4.4 are particularly promising for revealing the nature of the nonlinearity in the mine/soil system, and would benefit from further investigation. These future measurements would ideally take careful account of the properties of the fill material, as variations in the soil and sand appeared to be a significant factor affecting our measurements.

Chapter 5

Conclusion

In this thesis, methods of exciting and observing nonlinearity in a land mine/soil system have been explored, as well as models of this system that include nonlinearity. This work has advanced the theoretical understanding of the acoustical detection of landmines, and has provided some interesting though somewhat inconclusive experiments which may bring us closer to understanding what may be required for humanitarian demining.

The lumped-element model of Donskoy et al.[13] described in Chapter 2 provides one way to examine the behavior of the mine/soil system. Though it does not completely describe the complicated system, it provides insights to the behavior of nonlinear components in a resonant framework. The present numerical time-domain solution to the problem adds still more depth to the analysis by allowing easy implementation of different types of nonlinearity. This includes the application of bimodular nonlinearity, a type of nonlinearity that is common in soils and other geomaterials, but whose effects are difficult to appraise analytically.[18] In addition, the ability to examine spectra of the soil velocity and lid velocity allows easy comparison with experimental results. Extensive comparison with experiments involving detailed soil characterization will be needed to determine the appropriate values for the parameters in the model, particularly in terms of the type of nonlinearity present in the system and its associated parameters, as well as how this nonlinearity is affected by the presence or absence of a buried mine. If these can be determined, it would help greatly with developing different algorithms and methods for detection.

The sixteen-speaker standoff array introduced in Chapter 3 has significant potential in a practial land mine detection application due to the ability of the array to insonify a wide area at safe distances. In the frequency range considered for landmine detection in this thesis (90–250 Hz), the models and measurements performed on this array have demonstrated its ability to insonify the width of a typical roadway with amplitudes of no less than 20 dB down from the source strength at distances of up to 10 meters. Though the experiments described in Chapter 4 showed that the amplitudes generated by the standoff array in its present setup were on the low end of those capable of exciting observable nonlinearity, increased amplitude should be easily obtainable with more powerful equipment. Additionally, though this thesis did not address signal preprocessing enhancements to signal detection which would improve observable nonlinearity, it is known that many options exist and could be used to advantage, such as band-pass filtering or coherent correlation, etc.

A common theme in the experiments and measurements in Chapter 4 was the obfuscating effect of the burial material on the behavior of the buried mine. Though these experiments showed that nonlinear effects in the mine/soil system were capable of being excited and observed using our apparatus, the nonlinear effects of the soil itself were often difficult to distinguish from the nonlinear effects due to the presence of the buried mine. The use of a geophone to measure the soil velocity could be a factor, as it is subject to nonlinear interface effects similar to those at the mine/soil interface.[14] The less than ideal deployment conditions of the geophone could also have exacerbated this problem. Nonetheless, the use of the geophone affixed to the interior side of the mine case lid allowed us to observe a clear increase in nonlinear behavior in the mine itself when it was buried. Future investigations into the nature of nonlinear soil responses under different conditions using similar or different methods for excitation and observation would be very useful in refining mine detection techniques.

Further investigations are necessary before a field implementation of a nonlinear acoustical method for landmine detection is ready for deployment. For example, the entire subject of standoff methods for detection of nonlinearly vibrating landmines needs to be addressed, although significant progress has been made with the optical detection schemes cited. However, the findings reported in this thesis have corroborated and expanded upon previous work, and hopefully represent a step forward in bringing this beneficial acoustical technology to the field of humanitarian demining.

Appendices

Appendix A

Spectral Characteristics of Bimodular Nonlinearity

Here, we discuss the spectral characteristics of a signal subject to a bilinear modulus.

A.1 Single-frequency Excitation

We assume a sinusoidal stress input,

$$\sigma(t) = \sigma_0 \cos \omega t, \tag{A.1}$$

with cosine chosen to make the resulting strain an even function of time. The strain ϵ as a function of stress is given by

$$\epsilon(\sigma) = \begin{cases} \frac{1}{K}\sigma, & \sigma < 0 \\ \frac{1}{\gamma K}\sigma, & \sigma \geq 0, \end{cases} \tag{A.2}$$

which is an inversion of Eq. (2.2). Figure A.1(a) shows the stress input and the strain output for the type of bimodular nonlinearity considered here, while Fig. A.1(b) shows the stress response for a sinusoidal strain input.

The Fourier expansion of the strain is given by

$$\epsilon(t) = \frac{1}{2}a_0 + \sum_{n=1}^{\infty} a_n \cos n\omega t, \tag{A.3}$$

where (using the nondimensional time $\tau = \omega t$ to simplify)

$$a_n = \frac{2}{\pi} \int_0^{\pi} f(\tau) \cos n\tau \, d\tau. \tag{A.4}$$

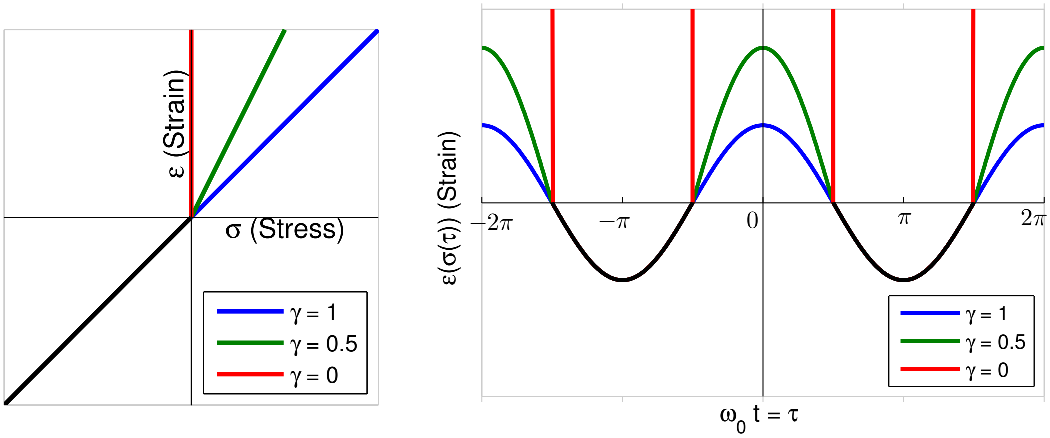

(a)

(b)

Figure A.1: (a) Bimodular stress-strain relationship and (b) strain responses under varying values of γ to a cosine stress input.

Now we can solve for each coefficient. For a_0, Eq. (A.4) becomes [recall Fig. A.1(b)]

$$a_0 = \frac{2}{\pi}\left[\int_0^{\pi/2} \frac{\sigma_0}{\gamma K}\cos\tau\, d\tau + \int_{\pi/2}^{\pi} \frac{\sigma_0}{K}\cos\tau\, d\tau\right], \tag{A.5}$$

which, when evaluated, gives

$$a_0 = \frac{2\sigma_0}{\pi K}\left(\frac{1}{\gamma} - 1\right). \tag{A.6}$$

Next, after applying the identity $\cos\alpha\cos\beta = \frac{1}{2}\left[\cos(\alpha-\beta) + \cos(\alpha+\beta)\right]$ to Eq. (A.4), the expression for a_n is given by

$$a_n = \frac{2}{\pi}\left[\int_0^{\pi/2} \frac{\sigma_0}{\gamma K}\cos\tau\cos n\tau\, d\tau + \int_{\pi/2}^{\pi} \frac{\sigma_0}{K}\cos\tau\cos n\tau\, d\tau\right] \tag{A.7}$$

$$= \frac{\sigma_0}{\pi K}\left\{\frac{1}{\gamma}\int_0^{\pi/2}\left[\cos(n-1)\tau + \cos(n+1)\tau\right]\, d\tau\right.$$

$$\left. + \int_{\pi/2}^{\pi}\left[\cos(n-1)\tau + \cos(n+1)\tau\right]\, d\tau\right\}. \tag{A.8}$$

The integrations yield

$$a_{n>0} = \frac{\sigma_0}{\pi K} \left\{ \frac{1}{\gamma} \left[\frac{\sin(n-1)\tau}{n-1} + \frac{\sin(n+1)\tau}{n+1} \right] \Bigg|_0^{\pi/2} + \left[\frac{\sin(n-1)\tau}{n-1} + \frac{\sin(n+1)\tau}{n+1} \right] \Bigg|_{\pi/2}^{\pi} \right\}. \tag{A.9}$$

Because of the $n-1$ term, $n=1$ is a special case, resulting in

$$a_1 = \frac{\sigma_0}{\pi K} \left[\frac{1}{\gamma} \left(\tau + \frac{1}{2} \sin 2\tau \right) \Bigg|_0^{\pi/2} + \left(\tau + \frac{1}{2} \sin 2\tau \right) \Bigg|_{\pi/2}^{\pi} \right] \tag{A.10}$$

$$= \frac{\sigma_0}{2K} \left(\frac{1}{\gamma} + 1 \right). \tag{A.11}$$

For n even (other than $n=0$),

$$a_{n \text{ even}} = \frac{\sigma_0}{\pi K} \left(\frac{1}{\gamma} - 1 \right) (-1)^{\frac{n}{2}-1} \left(\frac{2}{n^2-1} \right), \quad n \neq 0, \tag{A.12}$$

while for n odd (other than $n=1$)

$$a_{n \text{ odd}} = 0, \quad n \neq 1. \tag{A.13}$$

Using these results in Eq. (A.3) gives

$$\epsilon(t) = \frac{\sigma_0}{\pi K} \left(\frac{1}{\gamma} - 1 \right) + \frac{\sigma_0}{2K} \left(\frac{1}{\gamma} + 1 \right) \cos \omega t + \frac{\sigma_0}{\pi K} \left(\frac{1}{\gamma} - 1 \right) \sum_{m=1}^{\infty} (-1)^{m-1} \left(\frac{2}{4m^2-1} \right) \cos 2m\omega t \tag{A.14}$$

$$= \frac{\sigma_0}{\pi \gamma K} \left[(1-\gamma) + \frac{\pi}{2}(1+\gamma) \cos \omega t + 2(1-\gamma) \left(\frac{1}{3} \cos 2\omega t - \frac{1}{15} \cos 4\omega t + \ldots \right) \right]. \tag{A.15}$$

When $\gamma = 1$, corresponding to a fully linear Hooke's law relation between stress and strain, Eq. (A.15) reduces to $\epsilon(t) = \frac{\sigma_0}{K} \cos \omega t$ and there are no harmonics and no dc offset, as expected. Figure A.2 shows a sample spectrum with $f = \omega/2\pi = 100$ Hz and $\gamma = 0.5$.

The Fourier series can also be derived starting from a sine input. The derivation becomes slightly more involved because the resulting function is neither even nor odd,

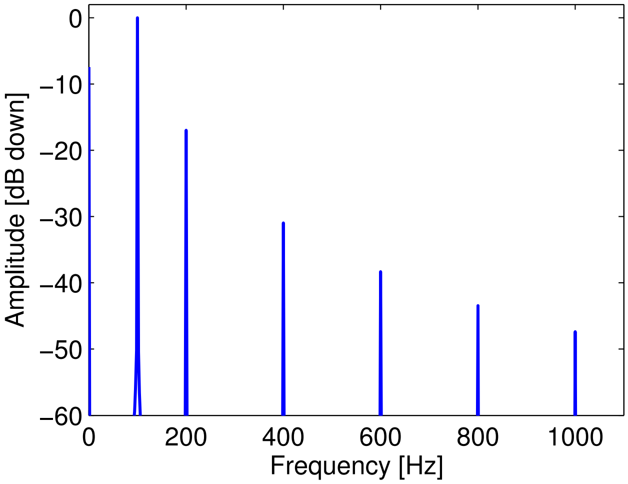

Figure A.2: Spectrum for response of a bimodular stiffness ($\gamma = 0.5$) to a sinusoidal input ($f = 100$ Hz).

but the results are very similar: the drive frequency term becomes a sine function, and the series for the even cosine harmonics is all positive. Otherwise the series is unchanged.

A few interesting aspects of these results are worth noting. First, there are no odd harmonics besides the fundamental frequency. Second, the amplitude of the harmonics is linearly related to amplitude of the input signal, as opposed to the quadratic or cubic relation frequently found in cases of nonlinearity. To demonstrate this, we examine the ratios of the first two nonlinearly generated harmonics to the fundamental, which show that these depend only on γ:

$$\left|\frac{a_2}{a_1}\right| = \frac{4}{3\pi}\,\frac{1-\gamma}{1+\gamma} \tag{A.16}$$

$$\left|\frac{a_4}{a_1}\right| = \frac{4}{15\pi}\,\frac{1-\gamma}{1+\gamma} \tag{A.17}$$

When $\gamma = 1$, the harmonics disappear, but when $\gamma = 0$, corresponding to a total lack of bonding when $\sigma > 0$, the amplitude of the harmonics is highest. Also, a DC term is included, which reflects the positive skewing seen in the shape of the functions in Fig. A.1(b).

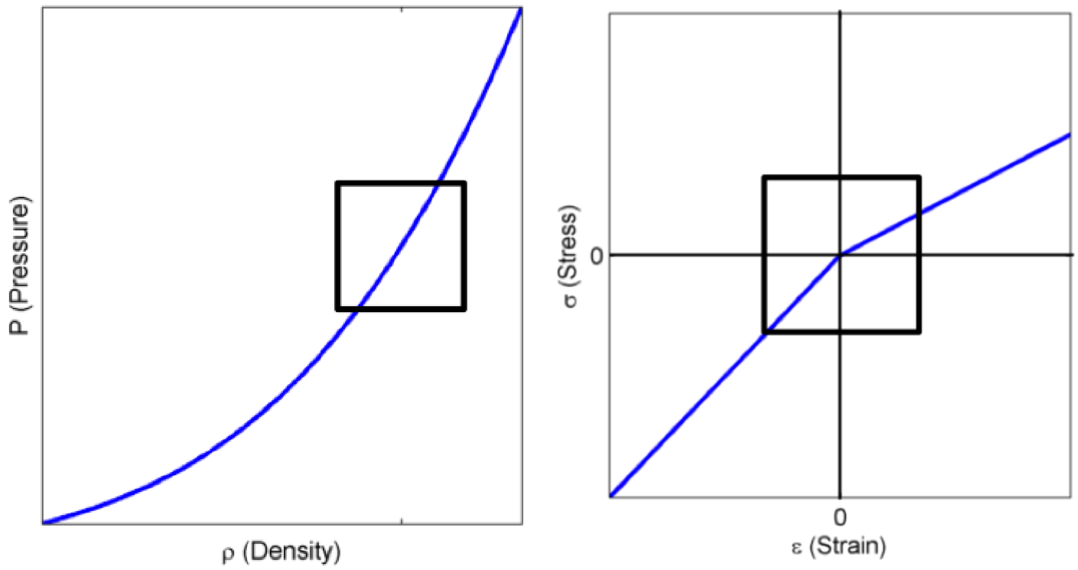

(a) **(b)**

Figure A.3: (a) In instances of classical nonlinearity such as the adiabatic gas law, $P \propto \rho^{1.4}$, small-amplitude oscillations (i.e., those that stay within the box in the figure) can be well-approximated by a linear relationship, but larger oscillations must take the curvature of the relationship into account. (b) On the other hand, for a bimodular stress-strain curve, the relation will have the same overall shape no matter the amplitude of oscillation (equivalently, size of the box).

This lack of amplitude dependence is unique compared to effects of classical nonlinearity. The reason for this is illustrated in Fig. A.3. When an element containing bimodular nonlinearity is excited, the only truly nonlinear area is the origin. Thus as long as the oscillations take the system through the origin, the overall shape of the nonlinearity remains the same. However, in cases of classical nonlinearity such as the adiabatic gas law, small oscillations around equilibrium can be well described by a linear relationship, but quadratic or higher-order relationships must be considered when the amplitude of oscillation becomes large.

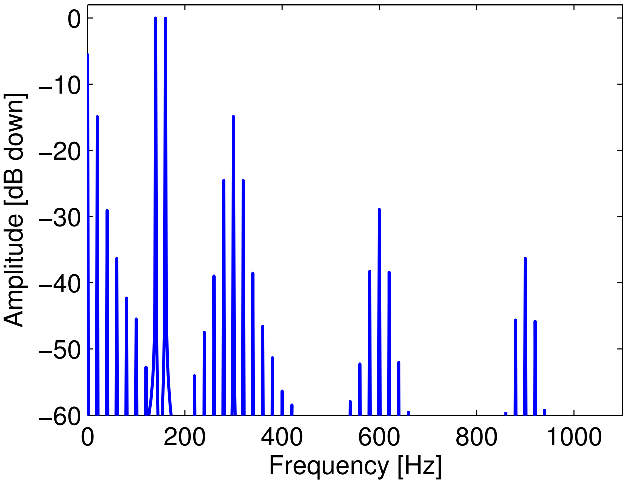

Figure A.4: Spectrum for response of a bimodular stiffness ($\gamma = 0.5$) to a bifrequency sinusoidal input with $f_1 = 140$ Hz and $f_2 = 160$ Hz. Note interaction frequencies clustered around even multiples of the sum frequency ($f_\Sigma = 300$ Hz).

A.2 Multiple-frequency Excitation

In general, the output $y(t)$ for an arbitrary input $x(t)$ could be represented as follows:

$$
\begin{aligned}
y(t) &= F[x(t)] && \text{(A.18)}\\
&= x(t)H[-x(t)] + \frac{1}{\gamma}x(t)H[x(t)], && \text{(A.19)}
\end{aligned}
$$

where H is the unit Heaviside step function. The Fourier transform of this would be difficult to evaluate analytically, but it is relatively straightforward to carry out numerically. Results for an input that consists of the sum of two cosines of different frequencies and equal amplitudes is shown in Fig. A.4. Though many interaction frequencies are evident in the spectrum, the largest responses other than those of the primaries are located at even multiples of the sum frequency, mirroring the absence of odd harmonics seen in the single-frequency case.

Appendix B

Manufacturers' Specification Sheets

This appendix contains specification sheets for the sensors and sources used in the experimental portion of the thesis. Section B.1 contains the specification sheet for the G.R.A.S. type 40BF 1/4-inch free-field microphone. Section B.2 contains the specification sheet for the G.R.A.S. type 26AC preamplifier used to amplify the microphone signal. Section B.3 contains the specification sheet for the geophones used to sense the lid and soil velocity. These are Sensor Nederland SM-11 geophones made in the Netherlands, and distributed in the U.S. by the Input-Output corporation. Section B.4 contains the specification sheet for the Crown® CE4000 audio amplifiers employed to drive the array and subwoofers. Section B.5 contains the specification sheet for the Renaissance Audio® MSW-1166 speakers employed in the standoff array. Section B.6 contains the specification sheet for the Peavey® Lo Max® 18-inch subwoofers employed for high-amplitude excitation of the buried mine. These were operated in 4-ohm dual (stereo) mode for the array directivity tests in Chapter 3, and in 4-ohm bridge (mono) mode otherwise.

B.1 Manufacturer's Specifications for Microphone

G.R.A.S. 40BF 1/4" Ext. Polarized Free-field Microphone

Freq range: 4 Hz to 100 kHz
Dyn range: 30 dB(A) to 171 dB
Sensitivity: 4 mV/Pa

The 40BF is an IEC 61094 WS3F ¼" externally polarized free-field microphone with rear-venting. The prepolarized equivalent is G.R.A.S. 40BE.

Specifications

Frequency range (±1 dB)	Hz	10 to 40 k
Frequency range (±2 dB)	Hz	4 to 100 k
Dynamic range lower limit (microphone thermal noise)	dB(A)	30
Dynamic range lower limit with G.R.A.S. preamplifier	dB(A)	35
Dynamic range upper limit	dB	171
Dynamic range upper limit with G.R.A.S. preamplifier @ +28 V / ±14 V power supply	dB	161
Dynamic range upper limit with G.R.A.S. preamplifier @ +120 V / ±60 V power supply	dB	173
Open-circuit sensitivity @ 250 Hz (±3 dB)	mV/Pa	4

G.R.A.S.
SOUND & VIBRATION

Headquarters Skovlytoften 33 • DK-2840 Holte • Denmark • Tel: +45 45 66 40 46 • Fax: +45 45 66 40 47 • E-mail: gras@gras.dk • www.gras.dk

Open-circuit sensitivity @ 250 Hz (±3 dB)	dB re 1V/Pa	-48
Resonance frequency	kHz	100
Microphone cartridge capacitance, typical	pF	7
Microphone venting		Rear
IEC 61094 designation		WS3F
Temperature range, operation	°C / °F	-40 to 150 / -40 to 302
Temperature range, storage	°C / °F	-40 to 85 / -40 to 185
Temperature coefficient @250 Hz	dB/°C / dB/°F	-0.01 / -0.006
Static pressure coefficient @250 Hz	dB/kPa	-0.02
Humidity range non condensing	% RH	0 to 100
Humidity coefficient @250 Hz	dB/% RH	-0.0013
Influence of axial vibration @1 m/s²	dB re 20 µPa	60
CE/RoHS compliant/WEEE registered		Yes / Yes, Yes
Weight	g / oz	1.75 / 0.062

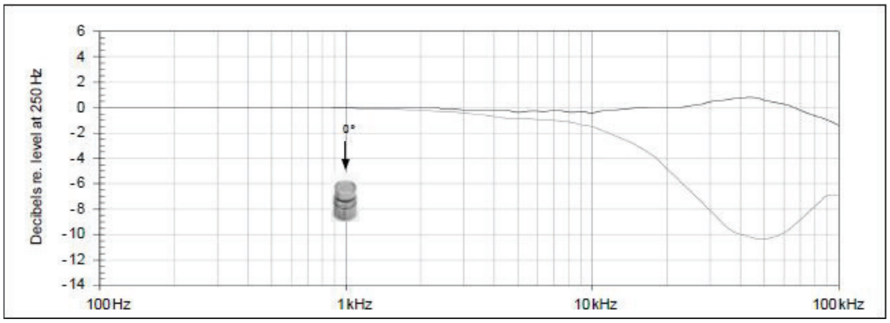

Typical frequency response (without protection grid). Upper curve shows free-field response for 0°, lower curve shows pressure response.

B.2 Manufacturer's Specifications for Microphone Preamplifier

¼″ Preamplifier Type 26AC, General-purpose

Specifications

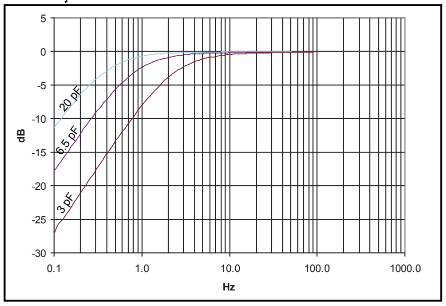

Fig. 3 Typical low-frequency response of Type 26AC for ½″ (20 pF), ¼″ (6.5 pF) and ⅛″ (3 pF) microphones

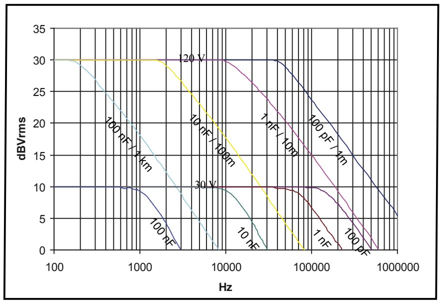

Fig. 4 Typical max. rms output signal with 120 V and 30 V supply

Technical Data

Frequency response (18pF/small signal):
2.5 Hz - 200 kHz . . . . ±0.2 dB

Slew rate:
20 V/µs

Input impedance:
20 GΩ, 0.5 pF

Output impedance (Cs = 20 pF, f = 1000Hz):
Typical . . . . 75 Ω

Noise (measured with 20 pF ½″ dummy mic.):
A-weighted:. . . . . ≤2.5 µV rms
(typically 1.8 µV rms)
Linear (20 Hz - 20 kHz): . . . . ≤6 µV rms
(typically 3.5 µV rms)

Gain*:
Typical:. . . . . -0.27 dB

Power supply:
Single:. . . . . 28 V (0.7 mA) to 120 V (2.5 mA)
Dual:. . . . . ±14 V (0.7 mA) to ±60 V (2.5 mA)

Maximum signal-output voltage (peak):
from ±10 V to ±50 V

Temperature:
Operation:. -30 °C to +70 °C
Storage: . . . . -40 °C to +85 °C

Relative humidity:
Operation:. . . . . 0 to 95 %
Storage: . . . . 0 to 95 %

Dimensions and Weight:
Diameter: . . . . 6.35 mm (¼″)
Length: . . . . 43 mm (1.7″)
Weight (without cable):. . . . . 6 g (0.2 oz)
Weight (with cable + LEMO conn.): 50 g (1.8 oz)

Accessories

Included

GR0010:	¼″ to ½″ adapter for use with G.R.A.S. ½″ microphones

Optional

RA0001:	Right-angled (90°) Adapter for ½″ microphone and ¼″ preamplifier
RA0003:	Adapter for ½″ microphone and ¼″ preamplifier
RA0006:	Angled (90°) Adapter ¼″ to ¼″.
AA0008:	Extension cable, 3 metres
AA0009:	Extension cable, 10 metres
AA0012:	Extension cable, 30 metres
AA0014:	Extension cable, 100 metres
AA0020_XX:	Extension cable, XX metres (customer-specified length)
AA0013:	Tripod adapter for ¼″ preamplifier
RA0096:	Tripod adapter for ¼″ preamplifier with angular adjustment

* Measured with 20 pF ½″ dummy microphone

G.R.A.S. Sound & Vibration reserves the right to change specifications and accessories without notice.

G.R.A.S.
SOUND & VIBRATION

Skovlytoften 33,
2840 Holte, Denmark
www.gras.dk gras@gras.dk

B.3 Manufacturer’s Specifications for Geophones

Specifications

INPUT/OUTPUT, INC.

	SM-11/U-FT
Frequency	
Natural frequency (f_n)	30 Hz
Tolerance	±5%
Maximum tilt angle for specified f_n	180°
Typical spurious frequency	>500 Hz
Distortion	
Distortion with 0.7 in/s p.p. coil-to-case velocity	<0.2%
Distortion measurement frequency	30 Hz
Maximum tilt angle for distortion specification	180°
Damping	
Open-circuit damping	0.55
Open-circuit damping tolerance	±5%
Resistance	
Standard coil resistances	360 Ω
Tolerance	±5%
Sensitivity	
Open-circuit sensitivity	30 V/m/s (0.75 V/in/s)
Tolerance	±5%
$R_tB_cf_n$	7,785 ΩHz
Moving mass	9.2 g (0.32 oz)
Maximum coil excursion p.p.	>1 mm (>0.04 in)
Physical Characteristics	
Diameter	26.6 mm (1.02 in)
Height	32 mm (1.26 in)
Weight	89 g (3.13 oz)
Operating temperature range	–40°C to +100°C (–40°F to +212°F)
Limited Warranty Period*	2 years

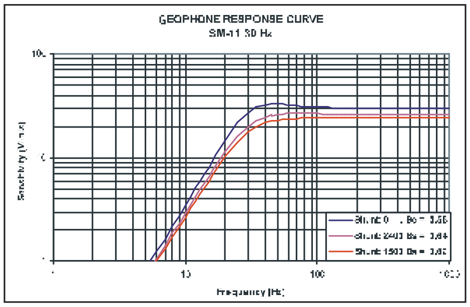

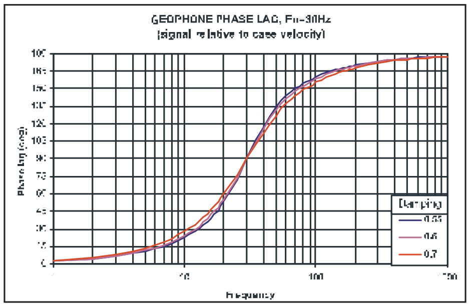

* Warranty excludes damage caused by high-voltage and physical damage to the element case.

All parameters are specified at +20°C in the horizontal position unless otherwise stated.

Ordering Information

SM-11

SM-11/U-FT	30 Hz	360 Ω	(upright)	P/N 1011010
SM-11/H-FT	30 Hz	360 Ω	(horizontal)	P/N 1011030

B.4 Manufacturer's Specifications for Amplifiers

CE 4000

CE SERIES

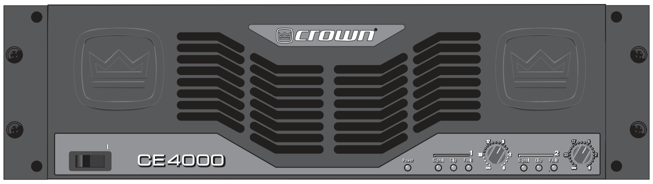

Features

- Patented, award-winning Class I (BCA) technology delivers high efficiency and superb sound
- Extremely reliable; keeps running under the harshest of conditions
- Switch-mode power supply with PFC (power-factor correction) allows world-wide use
- Sub-bass output via integral 4-position high-pass and 3-position low-pass filter sets for each channel
- Compatible with Crown SST (system solution topologies) input modules
- Choice of dual output connectors: 5-way binding post plus Neutrik® Speakon®, 5-way binding post plus barrier strip, or dual Neutrik Speakon
- 3-speed Fan On Demand
- Weighs just 34 pounds
- Three-Year, No-Fault Fully Transferable warranty completely protects your investment and guarantees its specifications

Engineered from the bottom up for top-notch performance and unmatched reliability, the Crown® CE 4000 amplifier represents the wave of the future for power amplifiers. Designed using Crown's patented, award-winning Class I (BCA® Balanced Current Amplifier) engineering, the CE 4000 provides superior power output, increased efficiency, legendary Crown sound and extraordinary reliability.

The CE 4000 not only handles but excels at 2-ohm loads. In repeated stress tests, the CE 4000 continued to perform at levels 12 dB into clip, long after the competition had shut down.

Designed for the utmost in flexibility, the CE 4000 features selectable on-board high-and low-pass filter sets, so you can easily add a sub-bass system. Additional signal control is available via Crown's optional SST (System Solution Topologies) modules, which offer a wide variety of active crossover configurations. Your choice of dual output connectors is also available: Neutrik® Speakon® plus 5-way barrier block, 5-way barrier block plus binding strip, or dual Neutrik Speakon.

Weighing in at a mere 34 pounds, the CE 4000 is easy to transport and set up. What's more, Crown's enhanced, switch-mode power supply (featuring power factor correction) results in a universal power supply, so you can plug it in anywhere. And with the lowest cost per watt of any amp in its class, the CE 4000 is the obvious choice for serious musicians everywhere.

For more details about the Crown CE 4000 amplifier, contact the Crown Technical Support Group at 800-342-6939 or 574-294-8200. Also, visit the Crown Audio website at www.crownaudio.com.

Specifications

Note: All measurements are in Stereo mode with 8-ohm loads and an input sensitivity of 26-dB gain at 1-kHz rated power unless otherwise specified.

Power

Load Impedance: Safe with all types of loads. Rated for 2, 4 and 8 ohms in Stereo mode, 4 and 8 ohms in Bridge-Mono mode.

Voltage Gain at 1 kHz, 8 ohm rated output:

39.0 dB gain at 0.775V sensitivity.
33.8 dB gain at 1.4V sensitivity.
26 dB gain at 3.46V sensitivity.

Required AC Mains: 50/60 Hz , 100-240VAC (±10%).

AC Line Current:

100 Volts: 8.5A
120 Volts: 7.1A
230-240 Volts: 3.7A

At Idle: Amp draws no more than 140 watts.

AC Line Connector: 15A IEC Connector with Country-Specific Cord and Plug.

Output Power:

CE 4000	*1 kHz Power
2 ohm Dual	**1400W****
4 ohm Dual	**1200W**
8 ohm Dual	**600W**
4 ohm Bridge-Mono	**2800W****
8 ohm Bridge-Mono	**2400W**

*1 kHz Power: refers to maximum average power in watts at 1 kHz with 0.5% THD.

**≥ 200V line voltage provides 1800W (2 ohm dual) and 3600W (4 ohm bridge-mono)

Performance

Frequency Response: ±0.25 dB from 20 Hz to 20 kHz at 1 watt.

Phase Response: ±15 degrees deviation from linear phase from 20 Hz to 20 kHz at 1 watt.

Signal to Noise Ratio, A-Weighted: Better than 100 dB below rated 1 kHz power.

Total Harmonic Distortion (THD): ≤ 0.5% at 1 kHz rated power, band-limited 20 Hz to 20 kHz.

Intermodulation Distortion (IMD): (60 Hz and 7 kHz at 4:1) Less than 0.5% at rated power to 30 dB below rated power at 8 ohms.

Damping Factor: Greater than 700 from 10 Hz to 400 Hz (measured using binding-post output connectors).

Crosstalk: Better than 50 dB below rated power, 20 Hz to 10 kHz.

Common Mode Rejection (CMR): Better than 70 dB from 20 Hz to 1 kHz.

DC Output Offset (Shorted Input): ±10 mV.

Controls & Connectors

Level: A 31-step detented rotary level control for each channel located on the front panel.

Power: An on/off rocker switch located on the front panel.

Mode: Turn power off before switching. A two-position switch located on the back panel below the input connectors which, when turned to stereo, operates the amplifier as two independent channels. When "Bridge-Mono" mode is selected, the amplifier bridges the two output channels for twice the output voltage.

Sensitivity: A three-position switch located on the back panel next to the Mode switch. Switchable among 0.775 volts or 1.4 volts for full output into an 8-ohm load (default setting), or 3.46 volts for a fixed voltage gain of 26 dB.

Fault Jack: A back-panel RJ-11 jack that may be remotely monitored to signal amplifier Fault condition. An LED or other signalling device (not supplied) may be used.*

Filter Switches:

Low Pass: A three-position switch for each channel located on the back panel below the input and output modules. Switchable among settings for Flat, 80 Hz and 100 Hz. Filter rolloff is 24 dB per octave.

High Pass: A four-position switch for each channel located on the back panel below the input and output modules. Switchable among settings for Flat, 30 Hz, 40 Hz and 50 Hz. Filter rolloff is 18 dB per octave.

*For more information, please consult the operation manual found at www.crownaudio.com.

INSTALLED

CE 4000

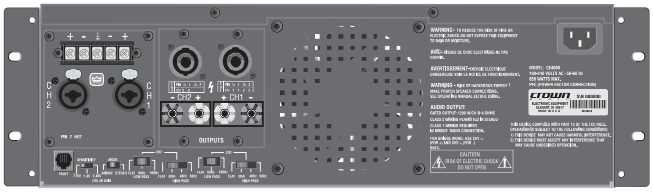

Indicators

Signal: A green LED for each channel which flashes when a very low-level signal (> –40 dBm) is present at input. May be used for troubleshooting cable runs.

Clip: A red LED for each channel which turns on when distortion becomes audible in the amplifier output.

Fault: Normally off, this red indicator will blink under five different conditions:

1. When the amplifier is first powered up, until the unit is ready for operation.
2. If the heatsinks reach a temperature above normal working limits.
3. If the transformer thermal protection circuit is activated.
4. If amplifier output wires develop a short-circuit.
5. Should the amplifier output stage become non-operational.

This circuit may be monitored remotely by plugging a simple switching circuit using an LED or other signaling device into the back-panel RJ-11 (Fault) jack. Under some conditions, the output of the amplifier will be muted.

Power: A green LED that turns on when the amplifier has been turned on and has power.

Input/Output

Input Connector (standard module): One Neutrik Combo connector for each channel which features a balanced ¼-inch (6.35-mm) phone jack and a 3-pin female XLR connector, in parallel with a barrier strip termination.

Input Stage: Input is electronically balanced and employs precision 1% resistors.

Input Impedance: Nominally 20 k ohms, balanced. Nominally 10 k ohms, unbalanced.

Input Sensitivity: 0.775 volts or 1.4 volts for standard 1 kHz power, or fixed 26-dB gain.

Output Connectors (three options available):

CE4D Module: Two 5-way binding posts in parallel with two Speakon® connectors (standard domestic configuration).

CE4E Module: Four Neutrik Speakon® NL4MP (mates with NL4FC) output connectors (standard export configuration).

CE4C Module: Barrier strip outputs in parallel with two 5-way binding posts.

Speakon® Wiring Configuration:

OUTUT PIN ASSIGNMENT

PIN	CH	PIN	CH
1+	2	1+	1
1–	2	1–	1
2+		2+	2
2–		2–	2
CH-2		CH-1	

Output Signal:

Stereo: Unbalanced, two-channel.

Bridge-Mono: Balanced, single-channel. Channel 1 controls are active; Channel 2 should be turned down.

Protection

CE 4000 amplifiers are protected against shorted, open or mismatched loads; overloaded power supplies; excessive temperature, chain destruction phenomena, input overload damage and high-frequency blowups. They also protect loudspeakers from input/output DC, large or dangerous DC offsets and turn-on/turn-off transients.

Construction

Rugged steel chassis is formed into a durable package. Coated with environmentally friendly powder for long life and ease of maintenance.

Cooling: Three-speed Fan On Demand.

Dimensions: EIA Standard 19-inch rack mount width (EIA RS-310-B), 5.25 inches (13.34 cm) high and 16.25 inches (36.56 cm) deep with additional 1-inch rear rack ears.

Weight:

Net weight: 33.3 lb (15.1 kg).
Shipping weight: 39.3 lb (17.8 kg).

Options

SST Modules

Crown's optional SST (System Solution Topologies) modules can improve the fidelity and versatility of your audio system. They feature a variety of professional signal routing and filtering capabilities. Your amplifier may have come with an SST module already factory-installed, or your choice of SST modules can be easily added to the amplifier by any authorized Crown Service Center. For more information, visit the Crown website at www.crownaudio.com.

Output Connector Options

See these options under Output Connectors.

Crown's Three-Year, No-Fault, Fully Transferable Warranty

Crown offers a Three-Year, No-Fault, Fully Transferable Warranty for every new Crown amplifier—an unsurpassed industry standard. With this unprecedented No-Fault protection, your new Crown amplifier is warranted to meet or exceed original specifications for the first three years of ownership. During this time, if your amplifier fails, or does not perform to original specifications, it will be repaired or replaced at our expense. About the only things not covered by this warranty are those losses normally covered by insurance and those caused by intentional abuse. And the coverage is transferable, should you sell your amplifier.

See your authorized Crown dealer for full warranty disclosure and details. For customers outside of the USA, please contact your authorized Crown distributor for warranty information or call 574-294-8200.

crown

H A Harman International Company

Crown Audio, Inc.
1718 W. Mishawaka Rd.
Elkhart, IN 46517-9439
TEL: 574-294-8200
FAX: 574-294-8FAX
www.crownaudio.com

Specifications subject to change without prior notice. Latest information available at www.crownaudio.com.

3/06 131791-4C

B.5 Manufacturer's Specifications for Speakers in Standoff Array

Renaissance Audio Group.

MSW-1166

6″ Bass Midrange

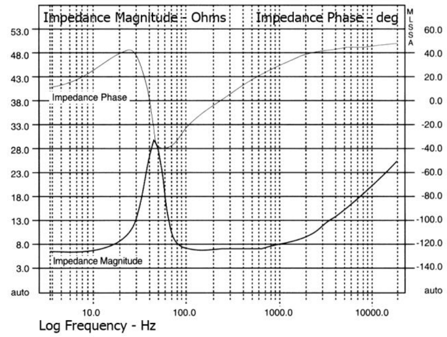

SPECIFICATIONS			
Nominal Power Handling (RMS)		P	150 W
Transient Power - 10 ms			1,000 W
Nominal Impedance		Z	8 Ω
Sensitivity 1W/1M			86 dB
Frequency Response			45 – 5,000 Hz
Resonant Frequency		FS	46 Hz
VOICE COIL			
Voice Coil Diameter		ϕ	75mm (3″)
Voice Coil Height			14.5 mm (0.57″)
Voice Coil Former			Aluminum
Voice Coil Wire			hexagonal shaped aluminum
Number of Layers			2
DC Resistance		RE	6.3 Ω
Voice Coil Inductance @ 1 kHz		LBM	0.61 mH
MAGNET SYSTEM			
Magnet System Type			double ferrite, vented
Magnetic Gap Height		HE	6 mm (0.24″)
Flux Density		B	0.68 T
BL Product		BXL	6.84 NA
Max. Linear Excursion		X	±4.25 mm (0.17″)
OPERATIONAL PARAMETERS			
Suspension Compliance		CMS	721 μM / Newton
Mechanical Q Factor		QMS	2.49
Electrical Q Factor		QES	0.64
Total Q Factor		Q/T	0.61
Mechanical Resistance		RMS	1.871 Kg S^{-1}
Moving Mass		MMS	16.3 g
Equivalent Cas Air Load		VAS	14.34 L
Cone / Dome Material			damped polymer composite
Effective Piston Area		S	119 cm^2
Dimensions	Diameter Cutout Height Mounting Depth		160mm (6.30″) 134mm (5.28″) 68.5mm (2.70″) 62mm (2.44″)
Net Weight			1.1 kg (2.4 lbs)

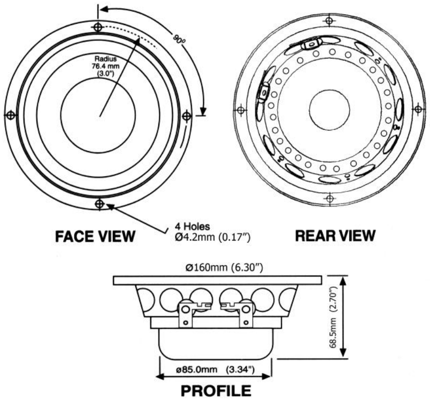

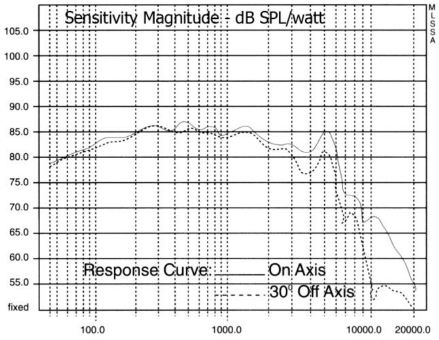

B.6 Manufacturer's Specifications for Subwooofers

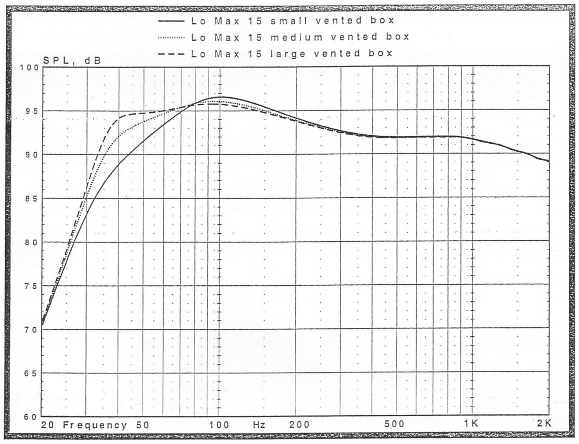

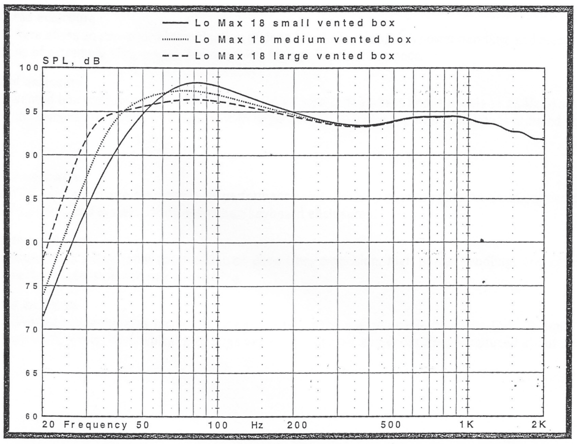

Kapton® is a registered trademark of DuPont.
Kevlar® is a registered trademark of DuPont.
Nomex® is a registered trademark of DuPont.
Rubatex® is a registered trademark of Rubatex Corporation.

PARAMETER DEFINITIONS

Znom: The nominal impedance of the driver in Ohms.

Revc: DC resistance of the driver in ohms, also known as Re.

Sd: The functional radiating surface area of the cone assembly in meters 2.

BL: Efficiency of the voice coil and magnet system in Tesla meters.

Fo: Free air resonance. Also known as Fs.

Vas: Volume of air having the same compliance (springiness) as the driver's suspension.

Cms: Restorative force of the driver's suspension in micrometers/Newton.

Mms: The total mass of the moving parts of the loudspeaker, including the air load, in grams.

Qms: Resonance characteristics of the mechanical factors of the loudspeaker.

Qes: Resonance characteristics of electrical factors of the loudspeaker.

Qts: Resonance characteristics of the electrical and mechanical factors combined together.

Xmax: Distance the cone can move in one direction before the coil begins to leave the magnetic gap.

Le: Inductance of the voice coil in millihenries.

SPL: Typical sound pressure level at 1 watt, 1 meter.

no: Electrical to acoustical conversion efficiency in percent.

Vd: Air displacement of the driver from negative Xmax to positive Xmax.

Pmax: Maximum continuous program power in watts.

Disp: Volume displaced by the driver inside the cabinet when mounted on its rear flange

SPECIFICATIONS	Lo Max® 18”	Lo Max® 15”
Part #	00560400	00560290
Size: inches / mm	18 / 460 nominal	15/ 380 nominal
Frame OD: inches / mm	18-1/8 / 460	15-1/4 / 387
Bolt circle: inches / mm	17-3/8 / 441	14-9/16 / 370
Cutout diameter: inches / mm	16-3/4 / 425	14-1/8 / 359
Depth: inches / mm	8-1/8 / 200	7-1/2 / 190.5
Impedance:	8 Ohms	8 Ohms
Power Capacity:	4800 Watts peak	4800 Watts peak
	2400 Watts program	2400 Watts program
	1200 Watts continuous	1200 Watts continuous
	40 Hz - 400 Hz	40 Hz - 400 Hz
Sensitivity:	97.1 dB / 1 W 1m	95.1 dB / 1 W 1 m
Usable frequency range:	30 Hz -500 Hz	30 Hz -500 Hz
Cone:	Kevlar® impregnated cellulose	Kevlar impregnated cellulose
Voice coil diameter:	4.0”/100 mm	4.0”/100 mm
Voice coil material:	Polyimide coated copper ribbon wire Polyimide – impregnated fiberglass former Nomex® stiffener Solderless diffusion welded OFHC Copper Leads	Polyimide coated copper ribbon wire Polyimide – impregnated fiberglass former Nomex stiffener Solderless diffusion welded OFHC Copper Leads
Net weight: lb./kg	33.5 / 15.2 kg	32.5 / 14.8 kg
Znom (ohms)	8	8
Revc (ohms)	5.40	5.40
Sd (Square Meters)	0.118	0.089
BL (T/M)	23.40	23.40
Fo (Hz)	31.5	38.5
Vas (liters)	294.4	124.0
Cms (uM/N)	140.0	110.8
Mms (gm)	194.68	146.00
Qms	11.15	11.00
Qes	0.330	0.364
Qts	0.386	0.385
Xmax (mm)	10.2	10.2
Le (mH)	0.75	0.75
SPL (1 W 1m)	95.5	95.5
no (%)	2.20	2.20
Vd (cubic inches/milliliters)	73.06 / 1197	55.15 / 904
Pmax (Watts pgm.)	2400	2400
Disp (inches3 / milliliters)	310 / 5080	242 / 3960

Appendix C

Collected Experimental Data

This appendix contains plots of relevant spectra for tests performed with the sixteen-speaker array and the subwoofers as discussed in Sec. 4.3, and for the amplitude response tests described in Sec. 4.4.

C.1 Sixteen-speaker Array Test Spectra

This section shows plots for the acoustic pressure and lid velocity spectra for tests performed with the sixteen-speaker array. The target site was located 2 m in front of the array, on axis. Each of these were continuous-wave tests, and had a Hann window applied across the $\sim$1.25 s duration of the signal before taking the FFT. The resulting bandwidth in the spectra was $\sim$1 Hz.

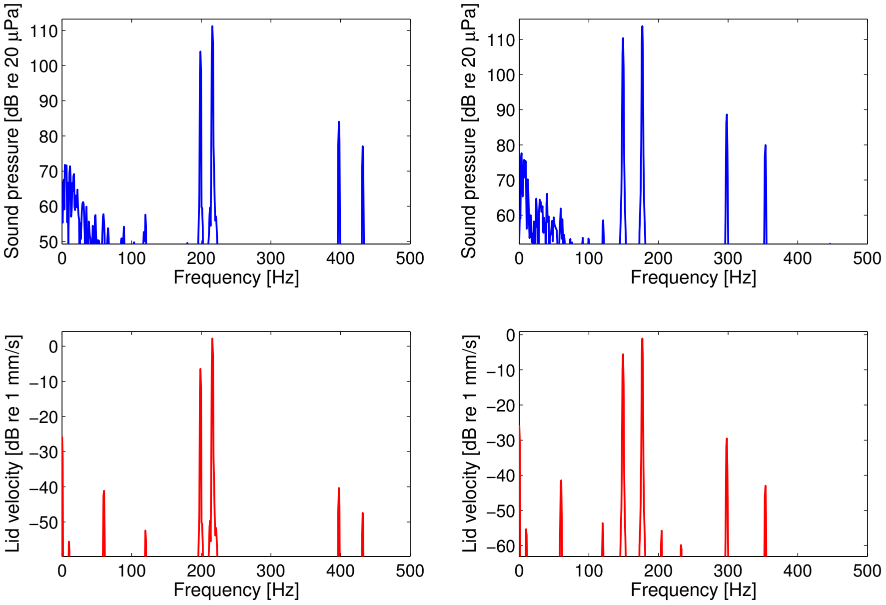

(a) **(b)**

Figure C.1: Unburied mine, standoff array insonification.
(a) $f_1 = 200$ Hz, $f_2 = 220$ Hz; (b) $f_1 = 150$ Hz, $f_2 = 175$ Hz.

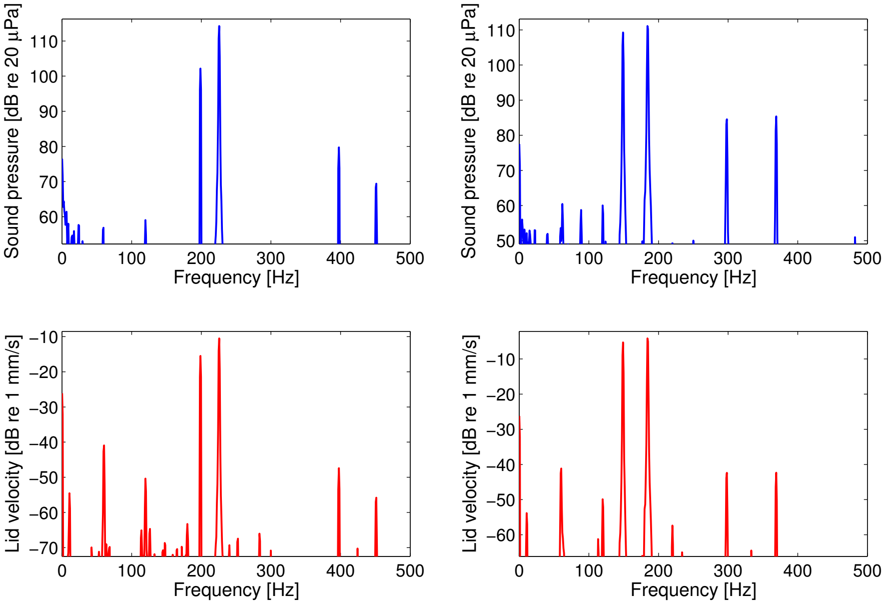

(a) **(b)**

Figure C.2: Disturbed (fresh) soil, 2 cm depth, standoff array insonification. (a) $f_1 = 200$ Hz, $f_2 = 225$ Hz; (b) $f_1 = 150$ Hz, $f_2 = 185$ Hz.

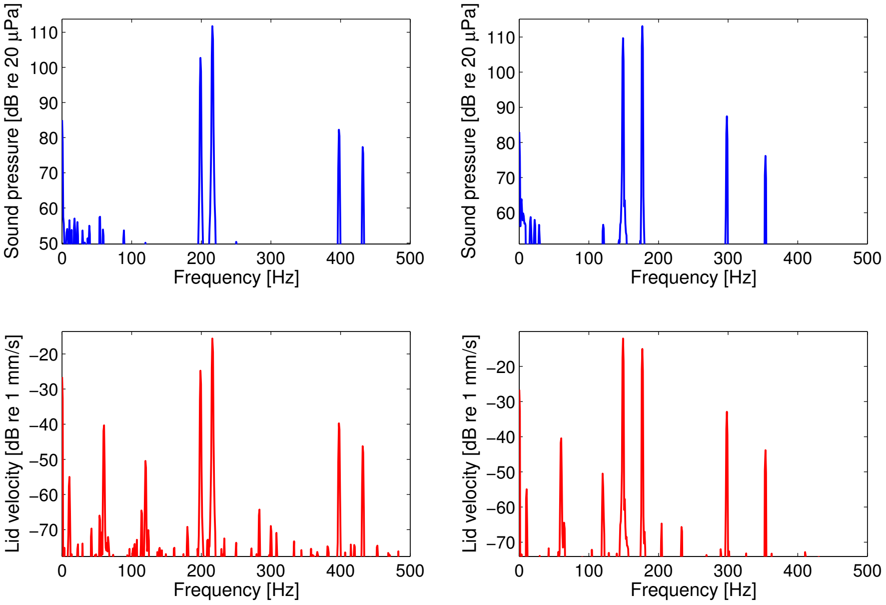

(a) **(b)**

Figure C.3: Disturbed (fresh) soil, 8 cm depth, standoff array insonification. (a) $f_1 = 200$ Hz, $f_2 = 225$ Hz; (b) $f_1 = 150$ Hz, $f_2 = 175$ Hz.

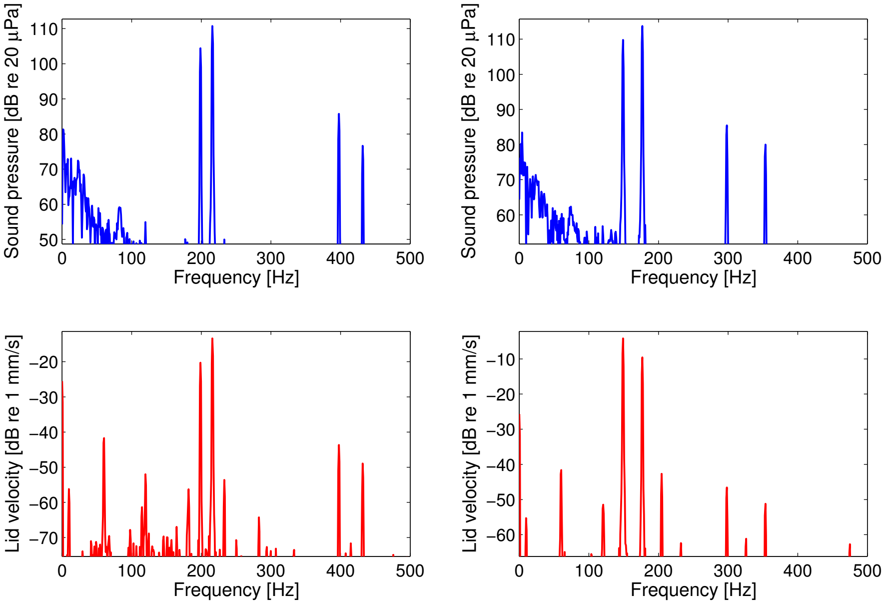

(a) **(b)**

Figure C.4: Dehydrated soil, 2 cm depth, standoff array insonification. (a) $f_1 = 200$ Hz, $f_2 = 220$ Hz; (b) $f_1 = 150$ Hz, $f_2 = 175$ Hz.

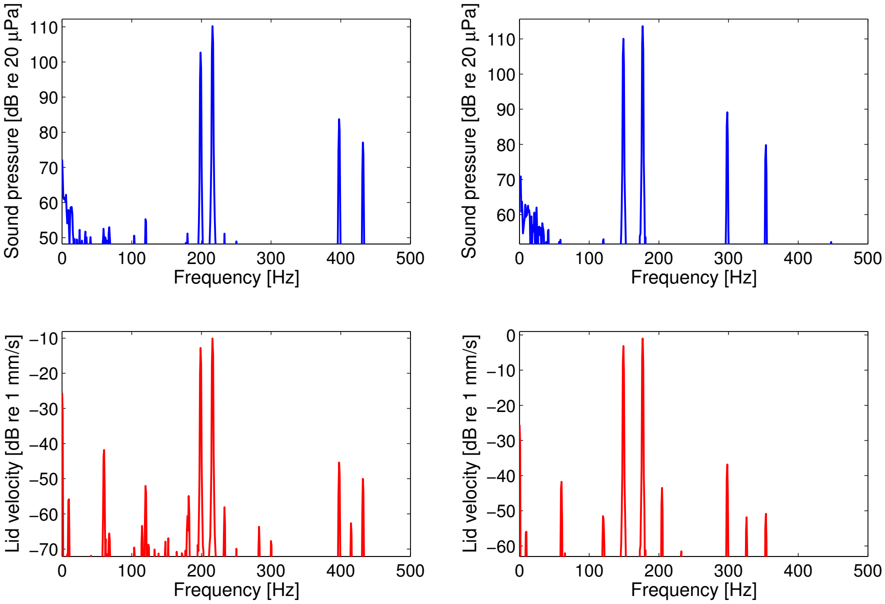

(a) **(b)**

Figure C.5: Settled soil, 2 cm depth, standoff array insonification. (a) $f_1 = 200$ Hz, $f_2 = 220$ Hz; (b) $f_1 = 150$ Hz, $f_2 = 175$ Hz.

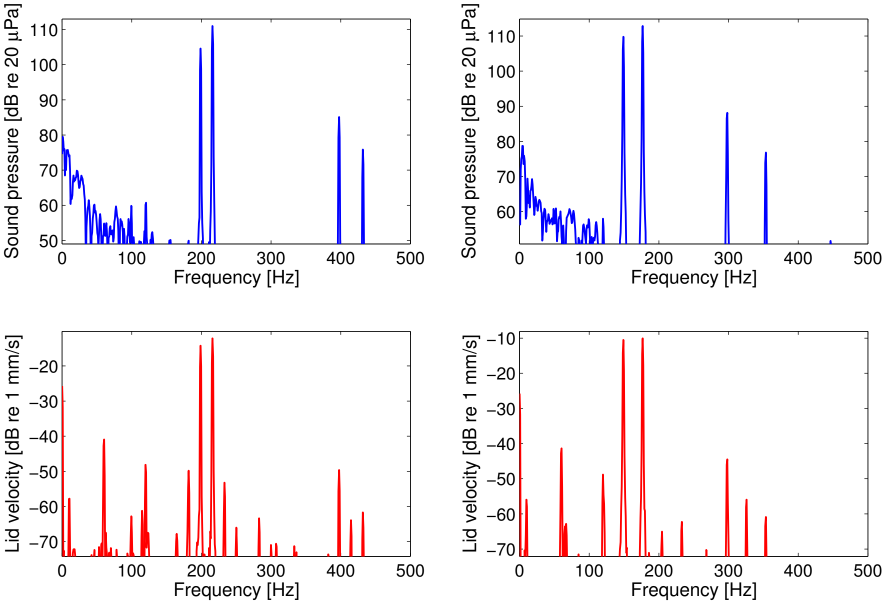

(a) **(b)**

Figure C.6: Disturbed (fresh) sand, 2 cm depth, standoff array insonification. (a) $f_1 = 200$ Hz, $f_2 = 220$ Hz; (b) $f_1 = 150$ Hz, $f_2 = 175$ Hz.

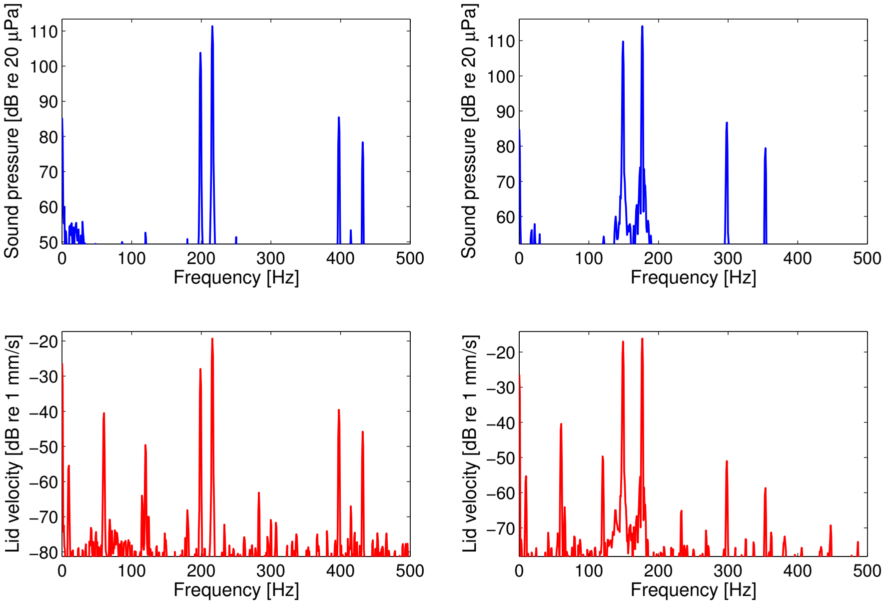

(a) **(b)**

Figure C.7: Disturbed (fresh) sand, 8 cm depth, standoff array insonification. (a) $f_1 = 200$ Hz, $f_2 = 220$ Hz; (b) $f_1 = 150$ Hz, $f_2 = 175$ Hz.

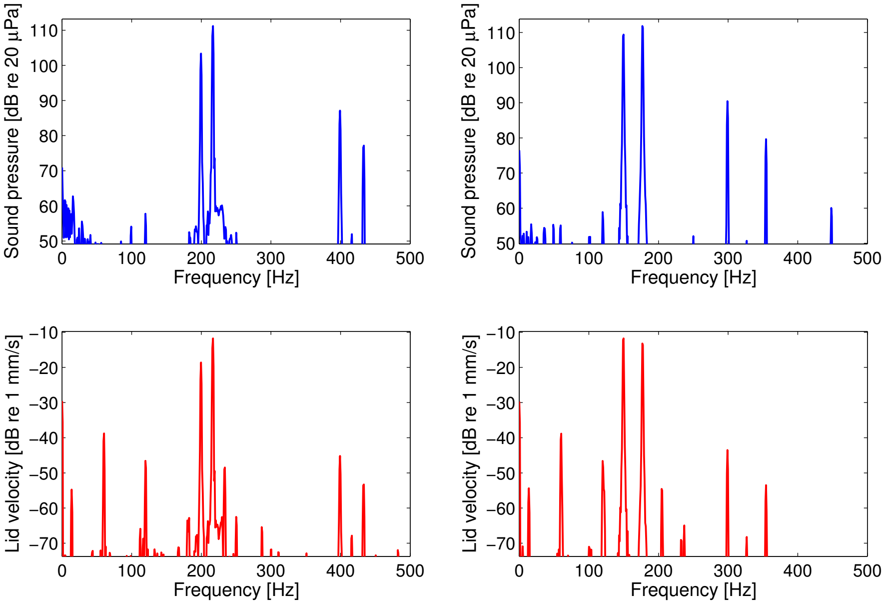

(a) **(b)**

Figure C.8: Settled sand, 2 cm depth, standoff array insonification. (a) $f_1 = 200$ Hz, $f_2 = 220$ Hz; (b) $f_1 = 150$ Hz, $f_2 = 175$ Hz.

C.2 Subwoofer Test Spectra

This section shows plots for the acoustic pressure and lid velocity spectra for tests performed with the sixteen-speaker array. Each of these were continuous-wave tests, and had a Hann window applied across the ~ 1.25 s duration of the signal before taking the FFT. The resulting bandwidth in the spectra was $\sim$1 Hz.

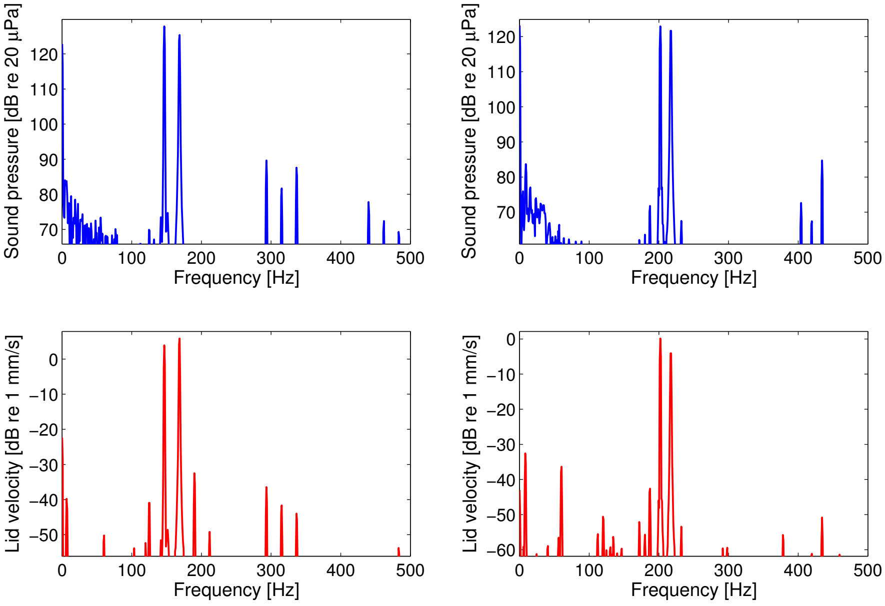

(a) **(b)**

Figure C.9: Unburied mine, subwoofer insonification.
(a) $f_1 = 150$ Hz, $f_2 = 170$ Hz; (b) $f_1 = 200$ Hz, $f_2 = 220$ Hz.

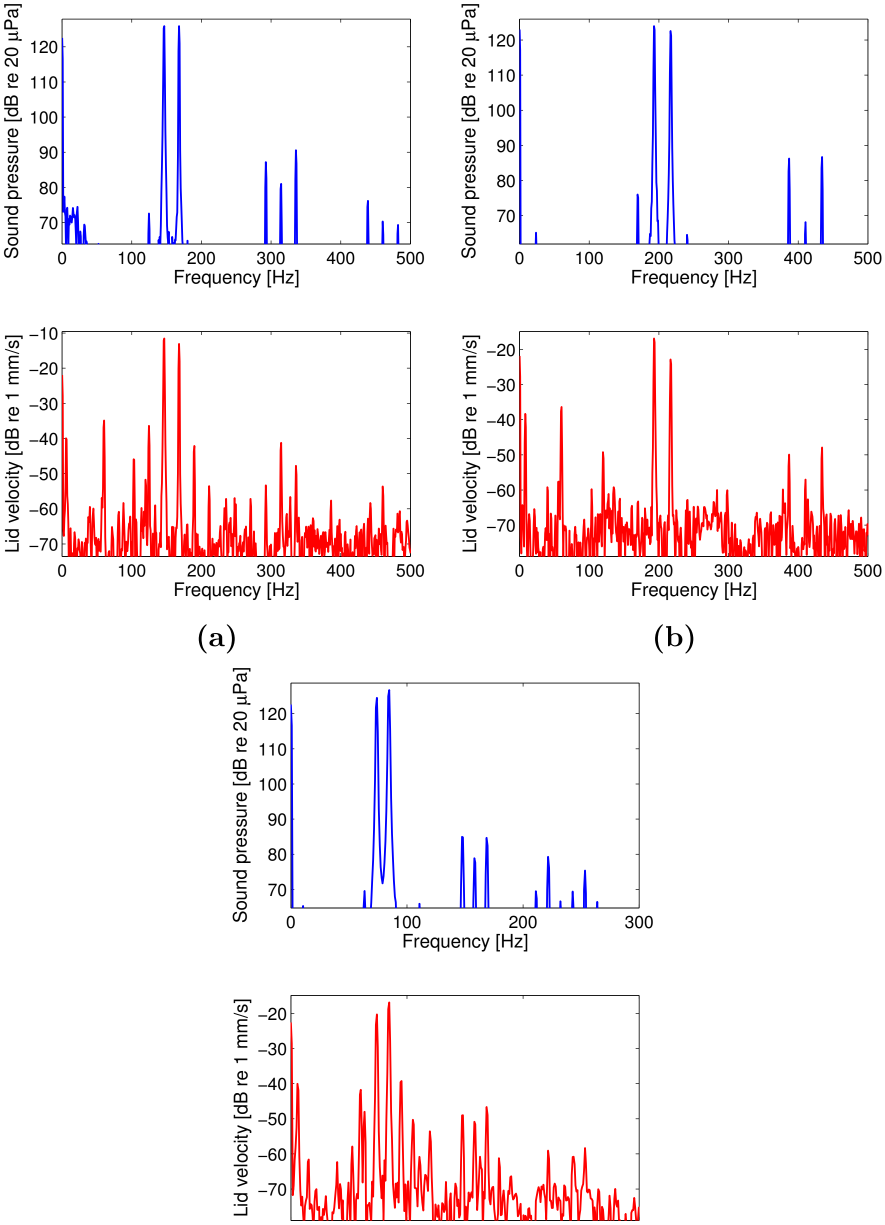

(a) **(b)**

(c)

Figure C.10: Disturbed (fresh) soil, 5 cm depth, subwoofer insonification. (a) $f_1 = 150$ Hz, $f_2 = 170$ Hz; (b) $f_1 = 200$ Hz, $f_2 = 220$ Hz; (c) $f_1 = 75$ Hz, $f_2 = 85$ Hz.

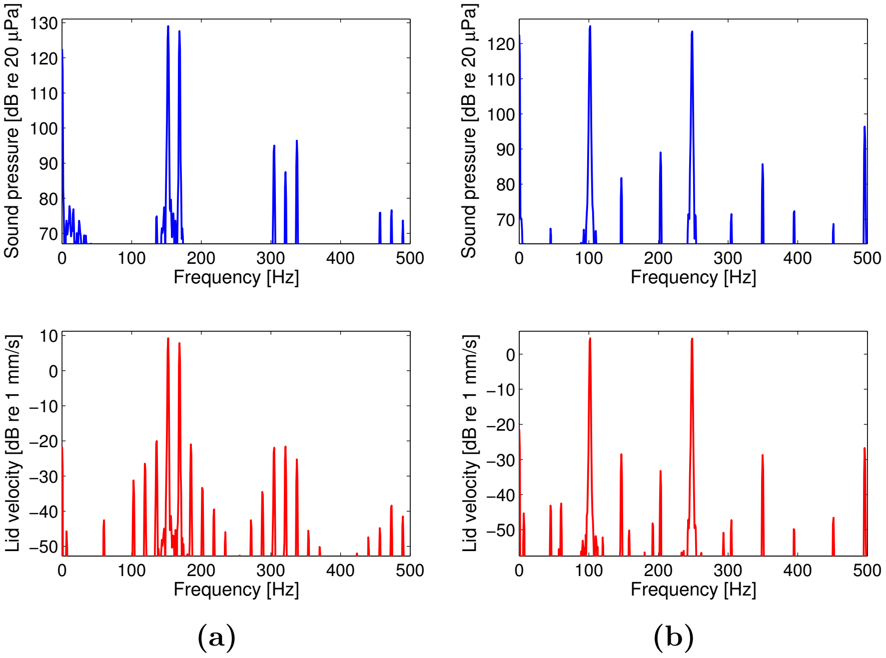

Figure C.11: Settled soil, 5 cm depth, subwoofer insonification. (a) $f_1 = 150$ Hz, $f_2 = 170$ Hz; (b) $f_1 = 100$ Hz, $f_2 = 250$ Hz.

C.3 Amplitude Response Spectra Using Subwoofers

This section shows frequency spectra for the acoustic pressure, lid velocity, and ground velocity corresponding to the amplitude response tests described in Sec. 4.4. Each of these used the subwoofers for pulsed bifrequency excitation with primary frequencies $f_1 = 90$ Hz and $f_2 = 110$ Hz and duration of 5 full beats. The time series for three trials were averaged, and a Hann window was applied to the averaged time series before taking the FFT. The resulting bandwidth in the spectra was $\sim$3 Hz.

Each figure represents results for one burial condition, and is organized in order of increasing amplitude, with spectra from the microphone, lid geophone, and ground geophone for each level of amplitude. For the buried cases in soil and sand (Figs. C.12 and C.14, respectively), the spectra are for the acoustic pressure at the soil surface, the lid velocity of the buried mine, and the ground velocity above the buried mine. For the unburied cases in sand and sand (Figs. C.13 and C.15, respectively), the spectra are for the acoustic pressure at the soil surface, the lid velocity of the unburied mine, and the ground velocity with no mine present. The levels in the spectra for the unburied lid velocity are somewhat suspect due to irregular placement of the unburied mine.

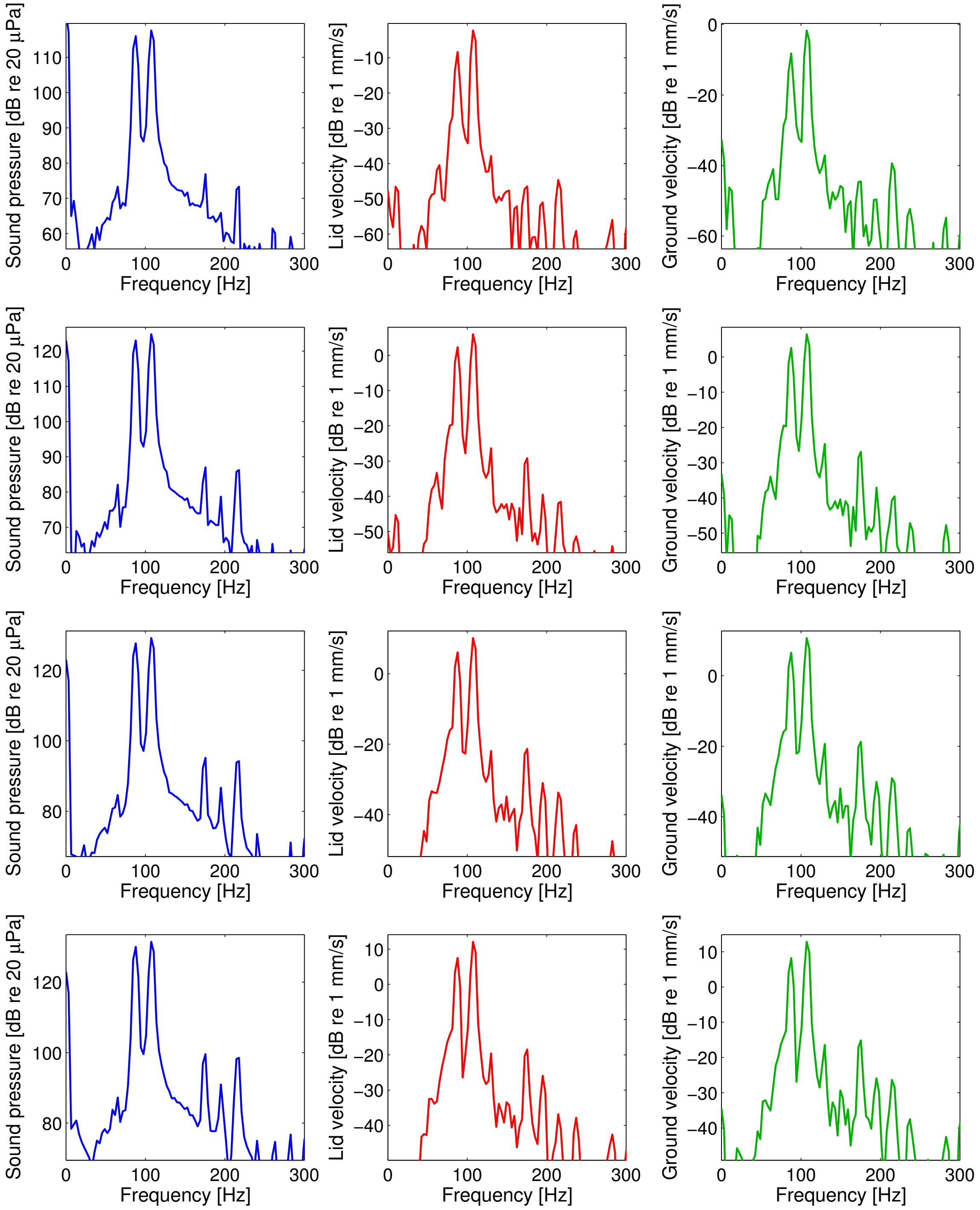

Figure C.12: Amplitude response measurements with subwoofers. Acoustic pressure, lid velocity and ground velocity spectra for mine buried under 5 cm soil. Continued on following page.

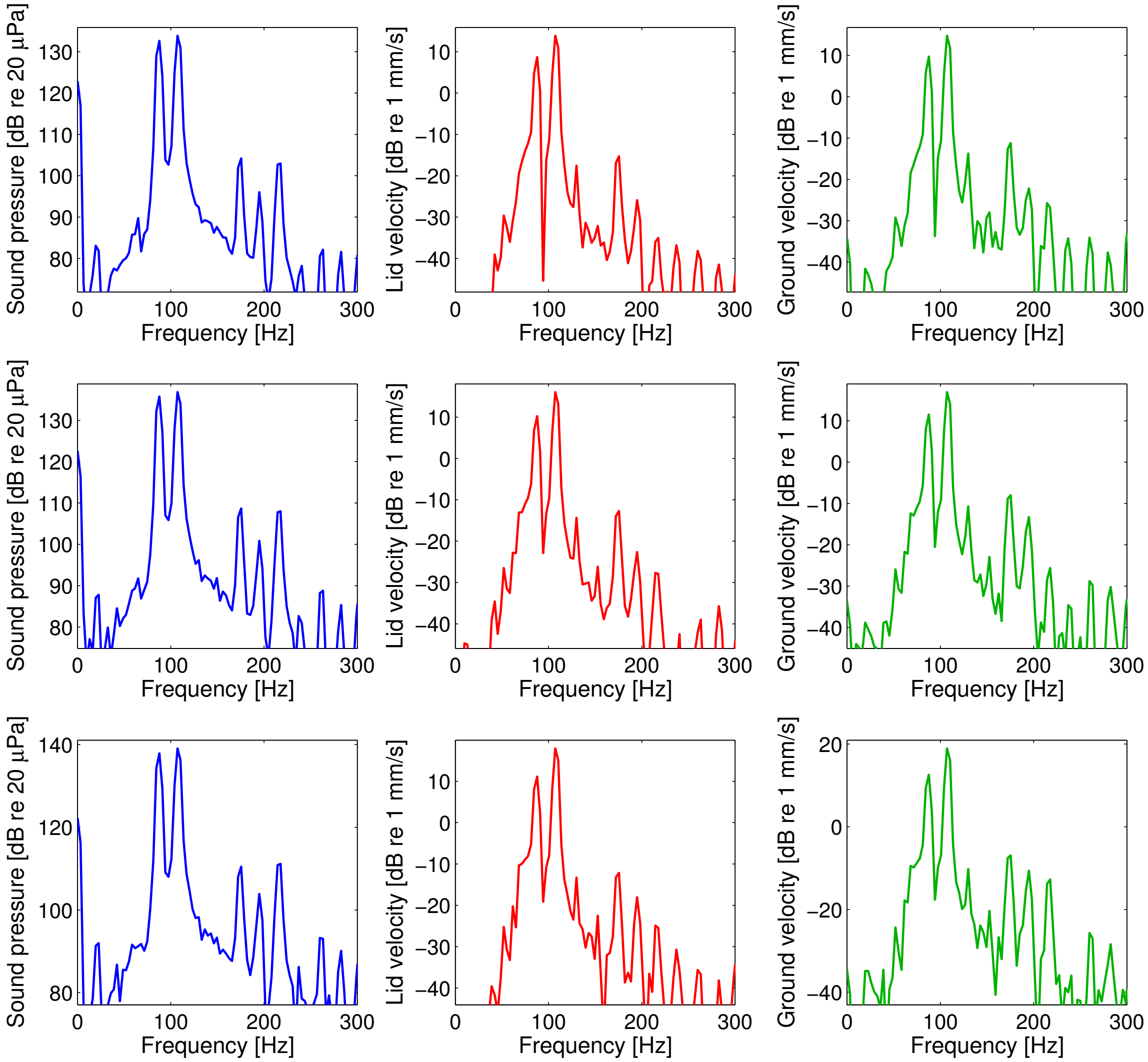

Figure C.12: Continued.

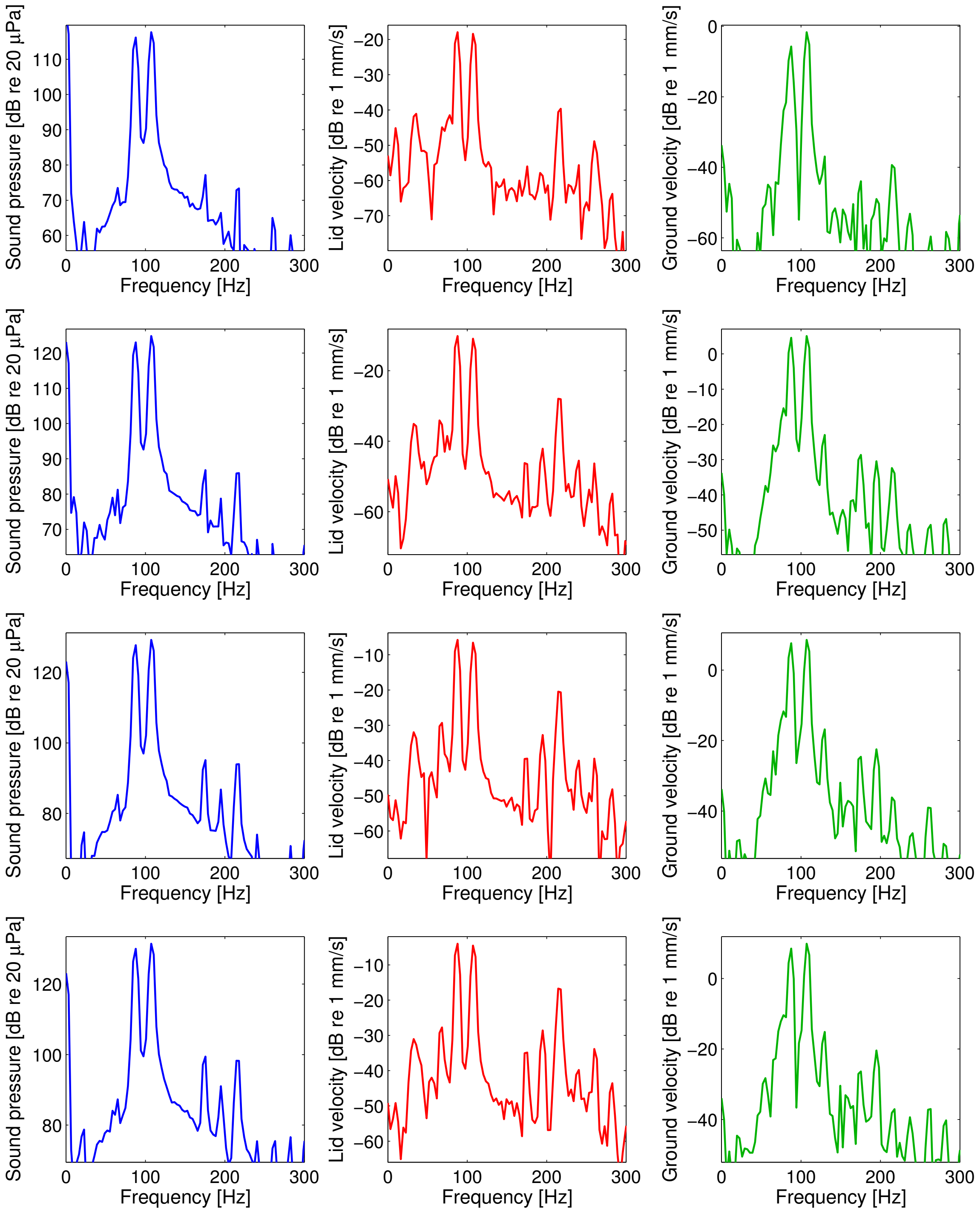

Figure C.13: Amplitude response measurements with subwoofers. Acoustic pressure, unburied lid velocity unburied lid velocity and velocity of geophone buried in sand with no mine present. Continued on following page.

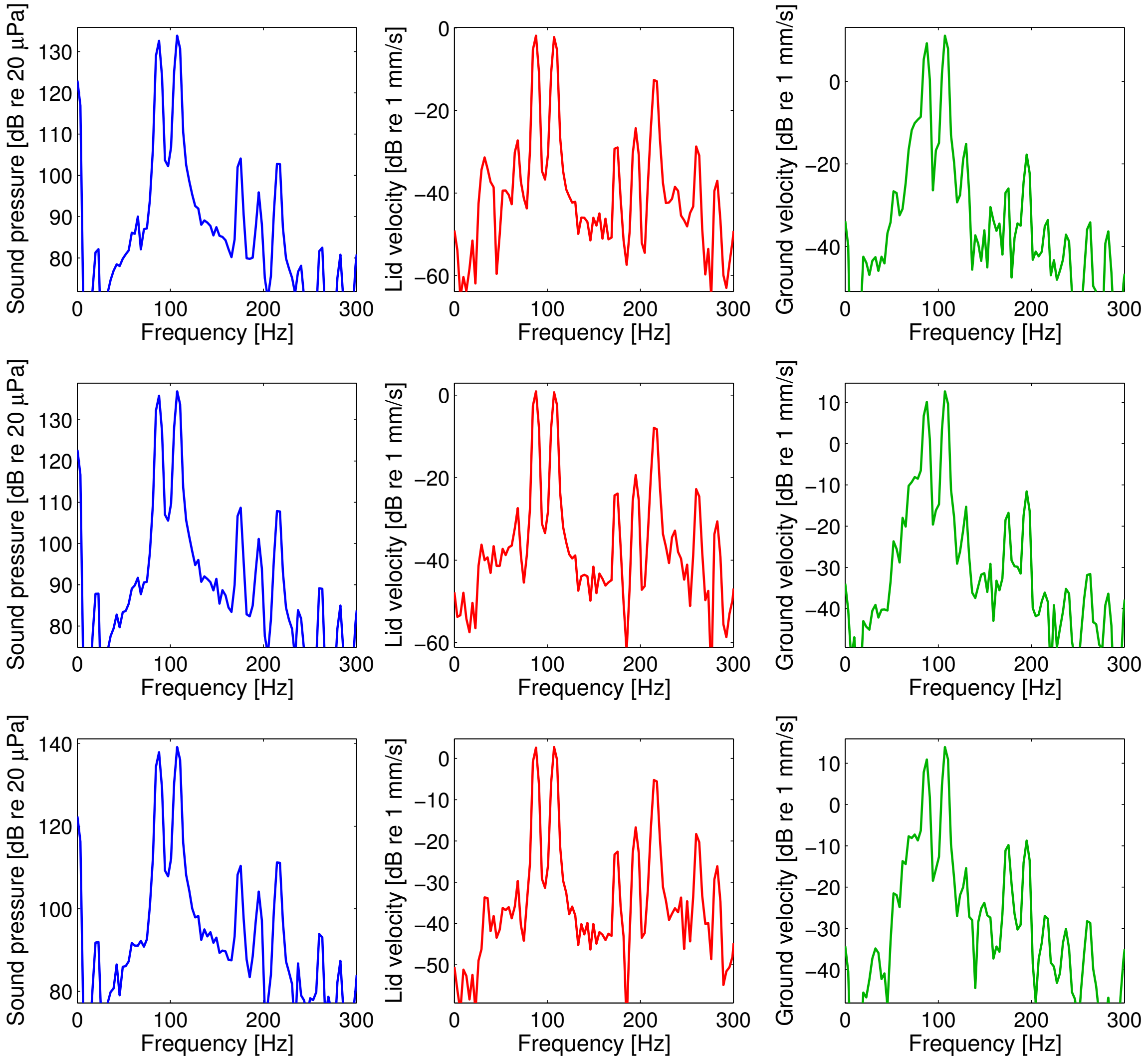

Figure C.13: Continued.

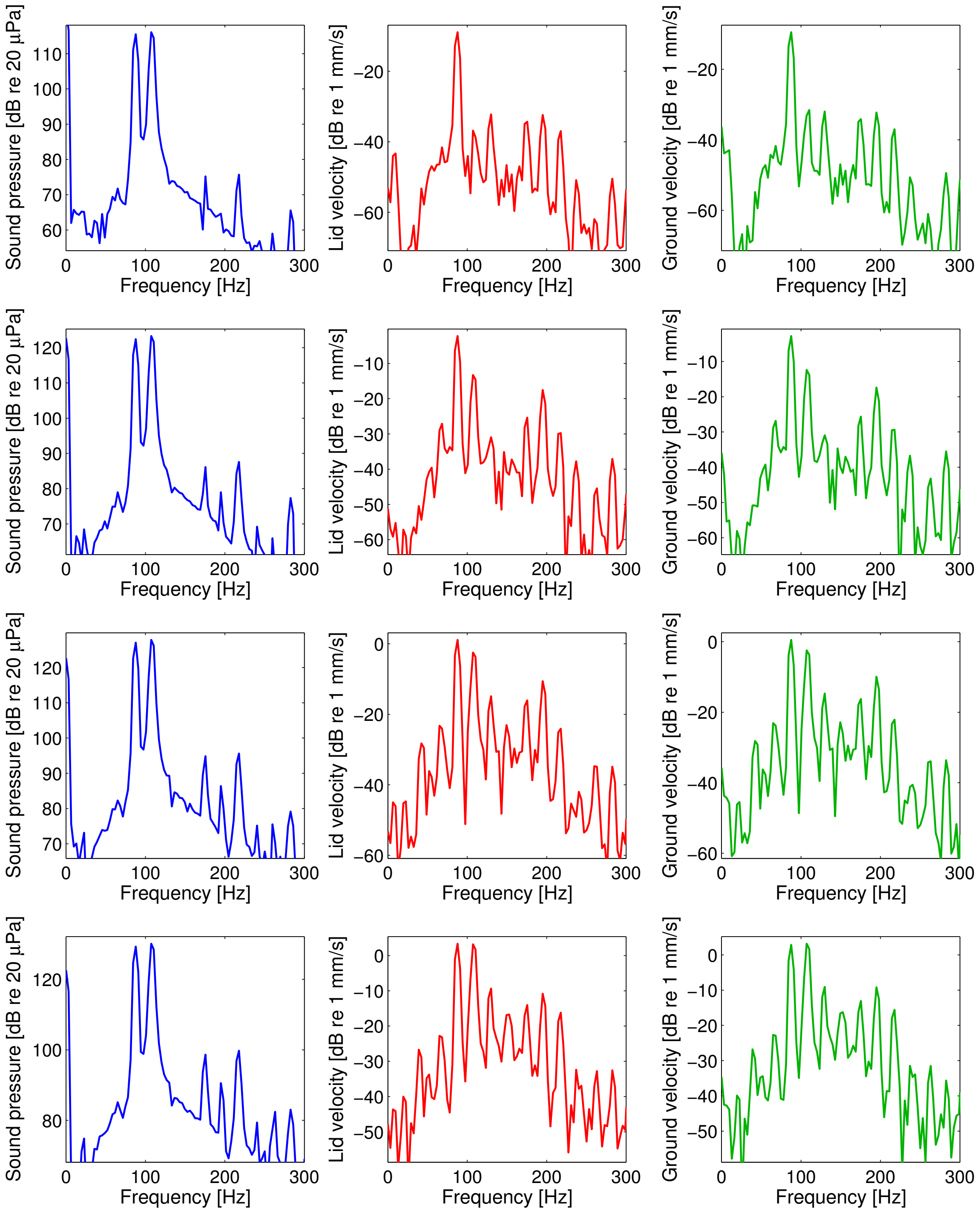

Figure C.14: Amplitude response measurements with subwoofers. Acoustic pressure, lid velocity and ground velocity spectra for mine buried under 5 cm sand. Continued on following page.

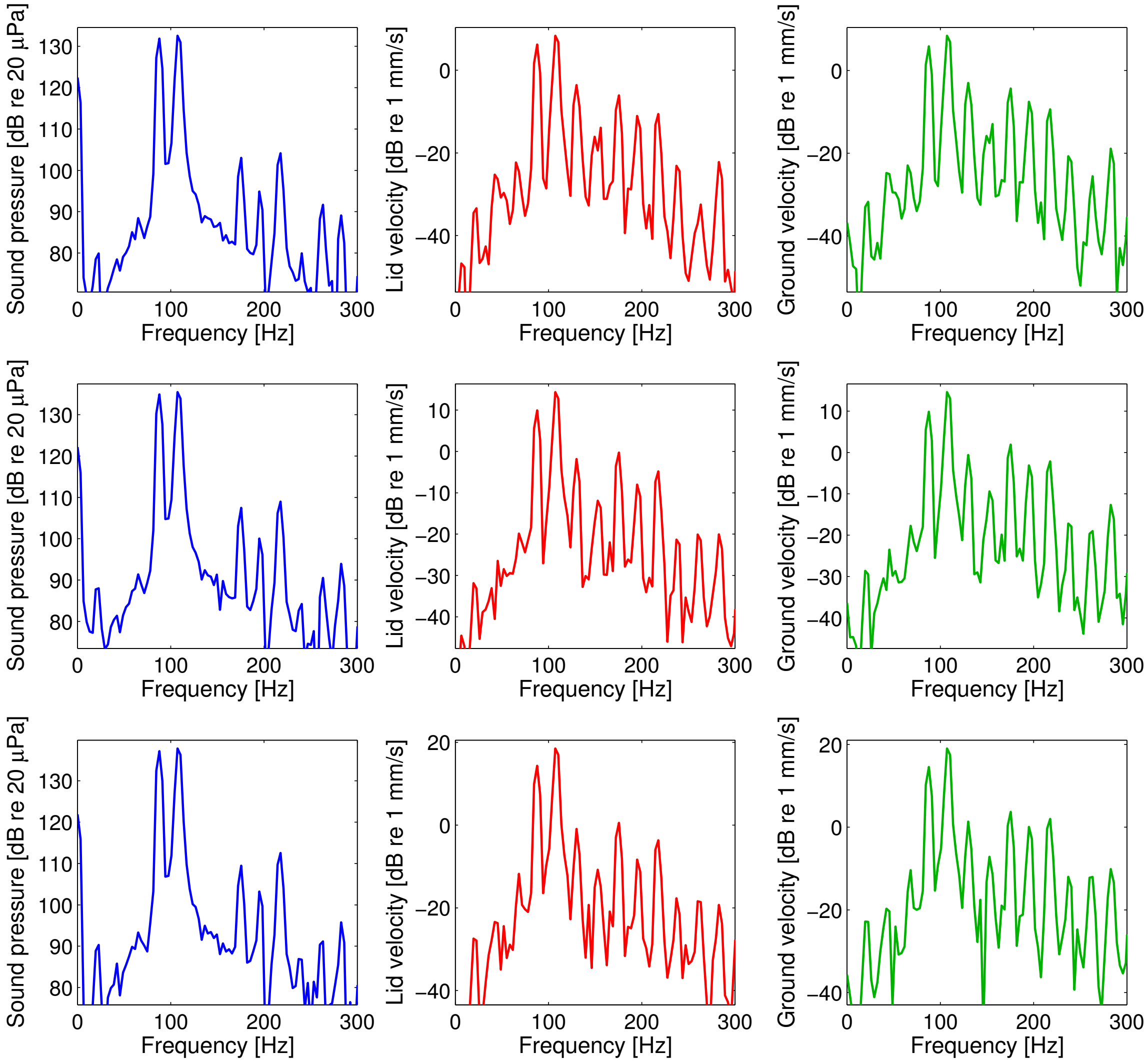

Figure C.14: Continued.

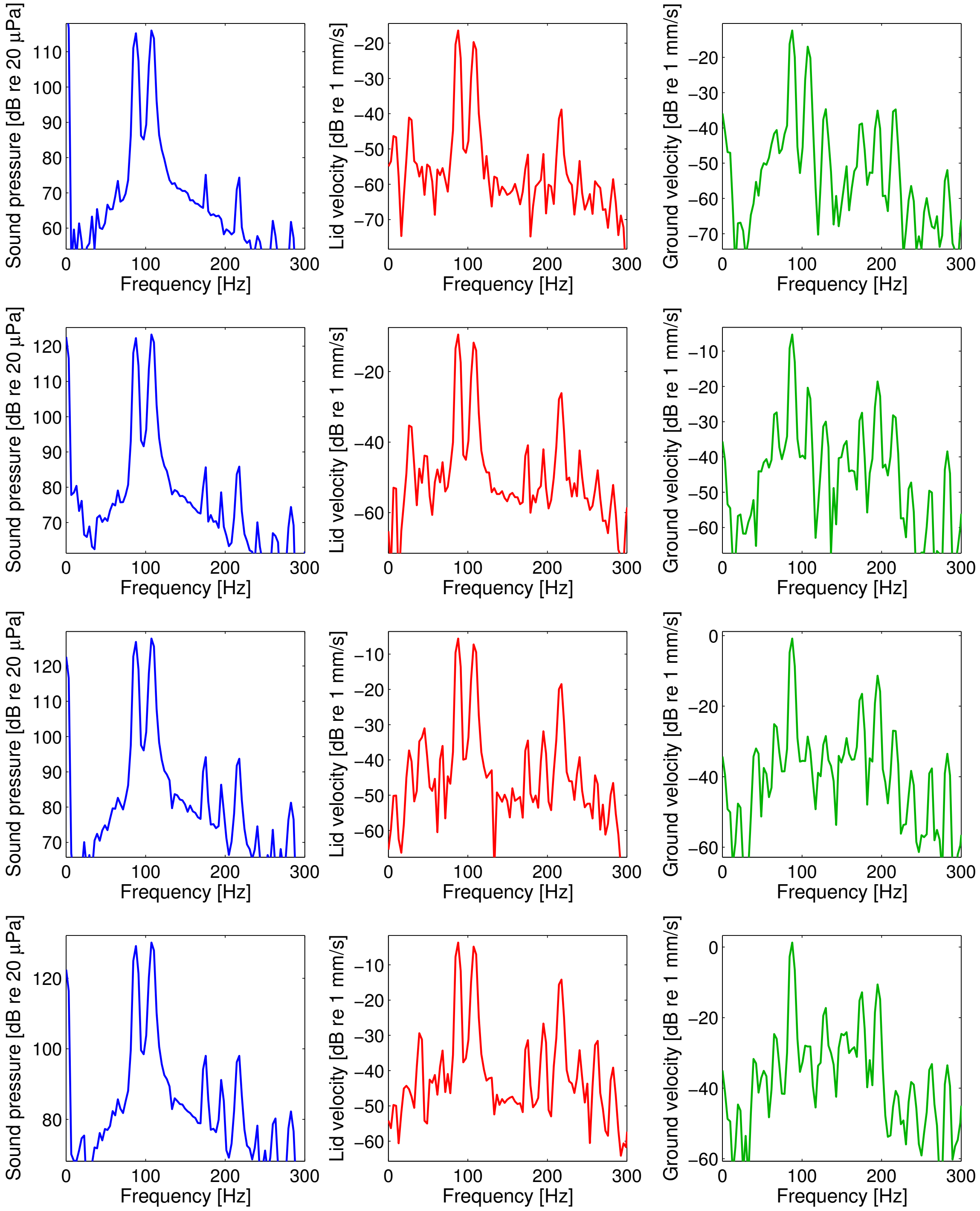

Figure C.15: Amplitude response measurements with subwoofers. Acoustic pressure, unburied lid velocity and velocity of geophone buried in sand with no mine present. Continued on following page.

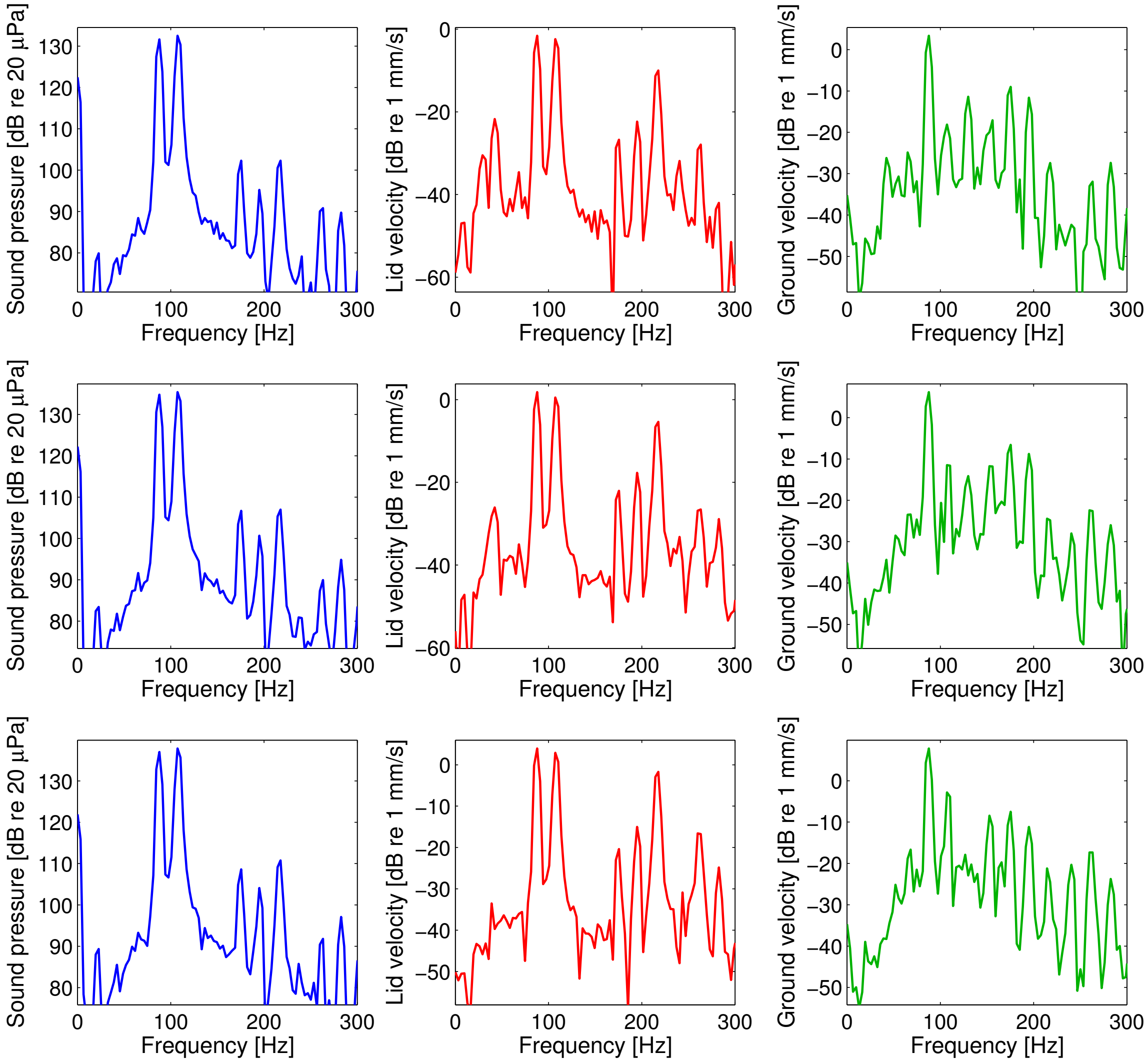

Figure C.15: Continued.

References

[1] J. M. Sabatier, “Advances in acoustic landmine detection”, Battlefield Acoustic Sensing for ISR Applications, Meeting Proceedings RTO-MP-SET-107 **120**, 5–1–5–10 (2006).

[2] T. G. Muir, R. D. Costley, and J. M. Sabatier, “Comparison of acoustic and seismic excitation, propagation, and scattering at an air-ground interface containing a mine-like inclusion”, Journal of the Acoustical Society of America **135**, 49–57 (2014).

[3] K. Gilbert and J. Sabatier, “Method for detecting buried objects by measuring seismic vibrations induced by acoustical coupling with a remote source of sound”, (2000), US Patent 6,081,481.

[4] D. Donskoy and A. Sutin, “Method and apparatus for acoustic detection of mines and other buried man-made objects”, (2002), US Patent 6,415,666.

[5] A. Zagrai, D. Donskoy, and A. Ekimov, “Structural vibrations of buried landmines”, Journal of the Acoustical Society of America **118**, 3619–3628 (2005).

[6] W. C. Kirkpatrick Alberts II, R. Waxler, and J. M. Sabatier, “Studying the mechanical behavior of a plastic, shock-resisting, antitank landmine”, Journal of the Acoustical Society of America **120**, 3655–3663 (2006).

[7] J. M. Sabatier and N. Xiang, “Laser-doppler based acoustic-to-seismic detection of buried mines”, in *SPIE Conference on Detection and Remediation Technologies for Mines and Minelike Targets IV*, edited by A. Dubey, J. F. Harvey, J. T. Broach, and R. E. Dugan, volume 3710, 215–222 (1999).

[8] J. S. Martin, D. J. Fenneman, F. Codron, P. H. Rogers, W. R. Scott Jr., G. D. Larson, and G. S. McCall, “Ultrasonic displacement sensor for the seismic detection of buried land mines”, Proceedings of SPIE **4742**, 617–628 (2002).

[9] D. Donskoy, A. Ekimov, N. Sedunov, and M. Tsionskiy, “Nonlinear seismo-acoustic land mine detection and discrimination”, Journal of the Acoustical Society of America **111**, 2705–2714 (2002).

[10] M. S. Korman and J. M. Sabatier, “Nonlinear acoustic techniques for landmine detection”, Journal of the Acoustical Society of America **116**, 3354–3369 (2004).

[11] W. C. Kirkpatrick Alberts II, J. M. Sabatier, and R. Waxler, “Resonance frequency shift saturation in land mine burial experiments”, Journal of the Acoustical Society of America **120**, 1881–1886 (2006).

[12] D. M. Donskoy, “Nonlinear vibro-acoustic technique for land mine detection”, Proceedings of SPIE **3392**, 211–217 (1998).

[13] D. Donskoy, A. Reznik, A. Zagrai, and A. Ekimov, “Nonlinear vibrations of buried landmines”, Journal of the Acoustical Society of America **117**, 690–700 (2005).

[14] K. Attenborough, Q. Qin, J. Jefferis, and G. Heald, “Accelerometer measurements of acoustic-to-seismic coupling above buried objects”, Journal of the Acoustical Society of America **122**, 3230–3241 (2007).

[15] B. J. Copenhaver, J. D. Gorhum, C. M. Slack, M. L. Barlett, T. G. Muir, and M. F. Hamilton, “Acoustic response of a buried landmine with a low grazing-angle source array, focused on the ground”, Proceedings of Meetings on Acoustics **19**, 045067 (2013).

[16] B. J. Copenhaver, J. D. Gorhum, C. M. Slack, M. L. Barlett, T. G. Muir, and M. F. Hamilton, “Acoustic response of a buried landmine with a low grazing-angle source array, focused on the ground”, Journal of the Acoustical Society of America **133**, 3457(A) (2013).

[17] B. J. Copenhaver, J. D. Gorhum, C. M. Slack, M. L. Barlett, T. G. Muir, and M. F. Hamilton, “Measurement and modeling of pulsed bi-frequency, nonlinear acoustic excitation of buried landmines”, Journal of the Acoustical Society of America **134**, 4129(A) (2013).

[18] L. A. Ostrovsky and P. A. Johnson, “Dynamic nonlinear elasticity in geomaterials”, Rivista del Nuovo Cimento **24**, 1–46 (2001).

[19] V. Nazarov, L. Ostrovsky, I. Soustova, and A. Sutin, “Nonlinear acoustics of micro-inhomogeneous media”, Physics of the Earth and Planetary Interiors **50**, 65–73 (1988).

[20] K. E.-A. Van Den Abeele, J. Carmeliet, P. A. Johnson, and B. Zinszner, “Influence of water saturation on the nonlinear elastic mesoscopic response in earth materials and the implications to the mechanism of nonlinearity”, Journal of Geophysical Research: Solid Earth **107**, ECV 4–1 – ECV 4–11 (2002).

[21] J. A. TenCate, E. Smith, and R. A. Guyer, “Universal slow dynamics in granular solids”, Physical Review Letters **85**, 1020–1023 (2000).

[22] P. A. Johnson, B. Zinszner, and P. N. J. Rasolofosaon, “Resonance and elastic nonlinear phenomena in rock”, Journal of Geophysical Research **101(B5)**, 11553–11564 (1996).

[23] K. Naugolnykh and L. Ostrovsky, *Nonlinear Wave Processes in Acoustics* (Cambridge University Press, New York) (1998).

[24] D. C. Karnopp, D. L. Margolis, and R. C. Rosenberg, *System Dynamics*, fifth edition (Wiley, New Jersey) (2012).

[25] A. Radostin, V. Nazarov, and S. Kiyashko, “Propagation of nonlinear acoustic waves in bimodular media with linear dissipation”, Wave Motion **50**, 191–196 (2013).

[26] M. L. Barlett, J. D. Gorhum, W. M. Wright, M. F. Hamilton, and T. G. Muir, “Vector wave measurements on landmine detection with an array of loudspeakers focused on the ground”, Journal of the Acoustical Society of America **130**, 2541(A) (2011).

[27] D. T. Blackstock, *Fundamentals of Physical Acoustics* (Wiley Interscience, New York) (2000).

[28] A. V. Oppenheim, A. S. Willsky, and S. Hamid, *Signals and Systems*, second edition (Prentice Hall, New Jersey) (1996).

[29] R. McGrath, *Landmines and Unexploded Ordnance: A Resource Book* (Pluto Press, Sterling, VA) (2000).

[30] F. J. Harris, “On the use of windows for harmonic analysis with the discrete fourier transform”, Proceedings of IEEE **86**, 51–83 (1978).

Vita

Benjamin Joseph Copenhaver was born in Lexington, Kentucky. In May of 2011 he received a Bachelor of Science degree from the University of Minnesota–Twin Cities, majoring in physics with minors in music and German. He entered the acoustics program in the Department of Mechanical Engineering at The University of Texas at Austin in August of 2011. Benjamin may be contacted at bcopenhaver@utexas.edu.

This thesis was typeset with LaTeX by the author.